A Search for Leptoquark and WZ Production with the DØ Detector in 1.8 TeV $\sqrt{s}$ $p\bar{p}$ Collisions with the 2 Jets + $\not\!\!E_T$ Final State

Christopher Paul Hays

Professor Philip Michael Tuts

Submitted in partial fulfillment of the

requirements for the degree

of Doctor of Philosophy

in the Graduate School of Arts and Sciences

COLUMBIA UNIVERSITY

2001

ABSTRACT

A Search for Leptoquark and WZ Production

with the DØ Detector

in 1.8 TeV $\sqrt{s}$ $p\bar{p}$ Collisions

with the 2 Jets + $\not\!\!E_T$ Final State

Christopher Paul Hays

We analyze 85.2 pb^{-1} of data for evidence of new particles and physical processes. The data were taken with the DØ detector at the Tevatron between 1994 and 1996 and correspond to an initial state of 1.8 TeV $\sqrt{s}$ $p\bar{p}$ collisions. We select events with 2 high p_T jets and large missing transverse energy and optimize for the observation of scalar and vector leptoquark production, and for WZ production. After comparing the data to the expected background, we set mass limits for scalar and vector leptoquarks, and a cross section limit for WZ production.

Contents

List of Figures

List of Tables

Acknowledgements

The data collected at the DØ detector are the product of the efforts of hundreds of people, and I would like to thank all those whose contributions made the experiment a success, and hence, this analysis possible.

There are several individuals who made direct contributions to this analysis, either by performing some of the actual work or by providing suggestions for the techniques of the analysis. I would like to thank Dan Claes, Eric Flattum, Carl Lundstedt, and Evgeny Popkov, for their efforts to collect the data and Monte Carlo, and for their studies of the trigger used in this analysis. I would like to thank Mike Tuts, Dave Toback, Greg Landsberg and the New Phenomena group, and Harrison Prosper and the Editorial Board, for their suggestions on the techniques and presentation of this analysis. The results presented here are the product of countless hours of discussion and collaboration with those mentioned above.

I would like to end with a special thanks to my advisor, Mike Tuts. He provided advice on the key decisions made in the analysis and he had a keen eye for inconsistencies in the plots and the text. His careful attention to the details contributed immensely to the integrity of this analysis.

To those who came before

so that I could understand;

for those who will follow,

so that they can understand better.

Preface

To many, physics is a foreign discipline requiring knowledge of obtuse equations and baffling concepts. While the physicist possesses a large body of knowledge attained through years of study, there is little else that separates the physicist from anyone else. Physics is the attempt to understand the world, and universe, we live in; in that sense, every child practices physics daily to gain the knowledge and understanding of her environment necessary for survival. The only difference between such a child and a physicist is that the physicist's knowledge allows her to ask questions that have not been previously answered and are significant to understanding our universe.

In practice, physical knowledge is gained by studying a particular phenomenon and devising a model to describe it. The model is tested in as many situations as possible, and if it fails a new model is developed to encompass a wider range of situations. As more and more tests are performed under more and more ex-

treme conditions, eventually the generality of the model extends to all cases of the phenomenon under study.

High energy physicists study the phenomenon of the structure of the universe itself. An obvious, but prescient, metaphor for the pursuit of the high energy physicist is that of putting together a jigsaw puzzle. The puzzle has been passed down from generation to generation and consists of some completed sections, several stray pieces, and many blank spaces. The experimental physicist finds and describes a piece, and the theoretical physicist determines the correct fit (and sometimes the order is reserved). It is the ultimate puzzle, as it provides the blueprint for the construction of the entire universe.

This thesis describes a search for the next piece of the puzzle. It tests the current model (the 'Standard Model') under conditions only recently achievable for study. These conditions allow for the production of particles and interactions that *could never before be observed.* Discovering such particles and interactions could lead to a wave of understanding, filling in whole new sections of the mysterious puzzle we call the universe.

Chapter 1

Introduction

1.1 Before the Standard Model

There have been many civilizations throughout history that developed a detailed understanding of certain aspects of our universe, particularly the motion of the stars and planets relative to the Earth. However, it was not until Isaac Newton published his fundamental laws of motion in 1686 [1] that we had a set of axioms upon which to build a detailed model of the universe. Newton's model described a fixed universe, with all objects in constant motion relative to it unless acted on by some external 'force.' Newton provided an equation relating forces to motion ($F = ma$), and developed a branch of mathematics (calculus) [2] that aided in the solution of the equation for a variety of situations.

Newton's laws withstood more than two hundred years of tests, but developments in the twentieth century forced a modification of his laws for extreme situations, where extreme corresponds to the very fast (close to the speed of light) or the very small (roughly the size of a molecule). In 1905, Albert Einstein showed that for objects moving very fast relative to one another, the absence of a fixed universe manifests itself in differences between the times and distances measured by the two objects [3]. Tests of Einstein's theory confirmed his predictions [4] and Newton's idea of a fixed universe was replaced by that of a malleable universe defined by the mass and energy it contained. Einstein went on to show that mass (and, equivalently, energy) curved the universe in just the right way to cause the force that Newton called 'gravity' [5].

Einstein's model of motion and curved spacetime (gravity) augmented the theory of electromagnetism developed by James Clerk Maxwell in the late nineteenth century [6]. Maxwell gathered a set of equations ('Maxwell's equations'), which described all of the known electromagnetic interactions and provided a deeper understanding of light as nothing more than electromagnetic waves. However, in what led to the modification of Newton's laws for the very small, Einstein showed that the elecromagnetic waves comprising light exist only in quantized energy 'packets' [7]; this immediately led to the understanding that as one probes smaller and smaller distances, one creates larger and larger disruptions to the object

being probed. Consequently, there is a limit to the knowledge one can obtain about an object's position and motion (this became known as the 'Heisenberg uncertainty principle' [8]).

In 1928, Paul Dirac combined the theories of the very fast (relativity) and the very small (quantum mechanics) into a single equation of motion for matter particles (specifically, particles known as 'fermions') [9]. The equation predicted the peculiar observed property of 'spin,' as well as the existence of 'antimatter' particles, each of which has the same mass but opposite force charges as its corresponding matter particle [10]. The discovery of the antielectron (or 'positron') in 1933 [11] was a triumph for Dirac's 'quantum field theory.'

Using quantum field theory, physicists in the 1930's developed descriptions for three of the forces: The electromagnetic force, as the exchange of a particle of light ('photon') between two electrically charged particles [12]; the 'weak' force, which is responsible for radioactive decay, as the direct interaction between weakly charged particles [13]; and the 'strong' force, which is responsible for binding neutrons and protons in the atom, as the exchange of a 'pion' particle between the proton and the neutron [14]. With some calculational finesse [15], physicists tested the electromagnetic quantum field theory ('quantum electrodynamics,' or QED) with striking precision and success [16]. However, similar successes for the strong and weak field theories were not forthcoming, and comprehensive theories

came only with the development of the Standard Model.

1.2 The Standard Model

In the early 1960's, there were four forces and many particles, with no underlying unifying principle (see Table 1.1). However, by the end of the decade, the particles had been organized and the electromagnetic, strong, and weak forces were described by *gauge field theories* [18].

1.2.1 The Strong Interactions

Murray Gell-Mann achieved an early success in classifying many of the known particles in terms of a few fundamental particles. He postulated that all of the hadrons are in fact bound states of constituent particles, which he dubbed *quarks* [19]. Based on overwhelming evidence in favor of this hypothesis [20], the Standard Model contains six quarks: Up (u), down (d), charm (c), strange (s), top (t), and bottom (b) (Table 1.2). These quarks combine in particle-antiparticle pairs (mesons), or in particle or antiparticle triplets (baryons), to form all of the known hadrons. For example, the familiar protons and neutrons, which comprise the atomic nucleus, are uud and udd bound states, respectively.

The understanding of hadron bound states was furthered by the description of

Hadrons

Particle	Symbol	Mass (MeV/c^2)
pi zero	π^0	135.0
pi plus/pi minus	$\pi^{\pm}$	139.6
K plus/K minus	$K^{\pm}$	493.9
K zero	K^0	497.8
proton	p	938.2
neutron	n	939.5
lambda	Λ	1115.4
sigma plus	Σ^+	1189.4
sigma zero	Σ^0	1191.5
sigma minus	Σ^-	1196.0
xi zero	Ξ^0	1311
xi minus	Ξ^-	1318

Leptons

Particle	Symbol	Mass (MeV/c^2)
electron neutrino	ν_e	< 2
muon neutrino	ν_μ	< 2
electron/positron	$e^{\pm}$	0.511
muon/antimuon	$\mu^{\pm}$	105.7

Table 1.1: *The known matter particles in 1962 [17], organized by those that participate in the strong interactions (hadrons) and those that do not (leptons); we do not include the massless photon. We express the masses as energies divided by the speed of light (c) squared; the energy unit is a million times the energy an electron gains from a one volt energy potential (MeV).*

the strong force as a gauge field theory [21]. In a gauge field theory, interactions between particles are mediated by force-carrying particles called *gauge bosons.* The strong force has eight gauge bosons ('gluons'), which exchange the strong charge, color, between quarks. There are three types of color charge, red (r), blue (b), and green (g). This model, Quantum Chromodynamics (QCD), vastly simplifies the description of the strong interactions. For example, we can write all of the up-antiup annihilations into a gluon using the following matrices:

$$\left(\begin{array}{ccc} \bar{u}_{\bar{r}} & \bar{u}_{\bar{b}} & \bar{u}_{\bar{g}} \end{array} \right) \left(\begin{array}{ccc} g_{\bar{r}r} & g_{\bar{b}r} & g_{\bar{g}r} \\ g_{\bar{r}b} & g_{\bar{b}b} & g_{\bar{g}b} \\ g_{\bar{r}g} & g_{\bar{b}g} & g_{\bar{g}g} \end{array} \right) \left(\begin{array}{c} u_r \\ u_b \\ u_g \end{array} \right) .$$

The bars over the quarks and colors denote 'antiquarks' and 'anticolors,' respectively; every gluon carries one color and one anticolor.[1] The colors of the inital up and antiup quarks become the gluon's color and anticolor, respectively; thus, color is conserved in this interaction. We can use a diagrammatic form designed by Richard Feynman [22] to express a given interaction; as an example, Fig. 1.1 shows a red up and an antiblue antiup annihilating, resulting in a red and antiblue gluon.

In addition to interactions between quarks and gluons, it is possible to have

[1] This description does not use the canonical basis for the gluon fields. The matrix shows nine gluons, but one of the gluons on the diagonal is a combination of the other two on the diagonal.

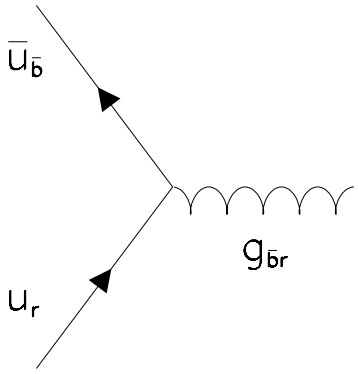

Figure 1.1: *Feynman diagram for the annihilation of up and antiup quarks into a gluon. The arrow into the vertex represents the incoming up quark; the arrow away from the vertex represents the incoming antiup quark.*

interactions between gluons and gluons, since the gluons possess color charge. Two incoming gluons can annihilate into one or two gluons, resulting in Feynman diagrams with three or four gluons meeting at a vertex (Fig. 1.2).

1.2.2 The Electroweak Interactions

In 1967, in the midst of the advances in QCD, Steven Weinberg, Sheldon Glashow, and Abdus Salam independently developed a unified description of the electromagnetic and weak interactions [23].

Quantum Electrodynamics describes the electromagnetic interactions as arising from the exchanges of photons between particles with electric charge. As an example, we can represent the annihilation of an electron and a positron into a

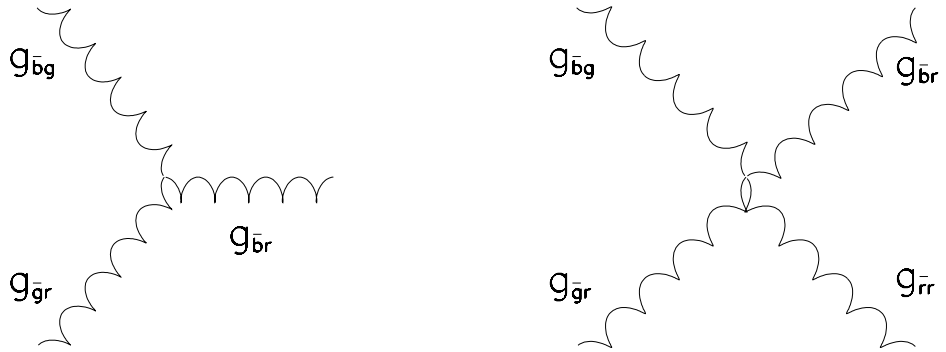

Figure 1.2: *Feynman diagrams for the annihilation of two gluons into one (left) or two (right) gluons. The color combinations shown here represent just two examples of the color exchanges that can occur.*

photon (γ) by a simple set of matrices,

$$(\,e^{+}\,)\,(\,\gamma\,)\,(\,e^{-}\,)\,,$$

or a Feynman diagram (Fig. 1.3). Since photons have no charge and interact only with electrically charged particles, photons do not interact directly with themselves (unlike gluons).

Using the gauge field theory formalism, Glashow, Weinberg, and Salam incorporated electromagnetism into the weak interactions. They postulated a set of three gauge bosons, W^{+}, W^{-} and Z^{0}, which mediate the weak interactions. These bosons exchange 'flavor' charge between quarks or leptons; unlike gluons, the $W^{\pm}$ and Z^{0} have non-zero masses. The Higgs particle (Section 1.2.3) possesses weak

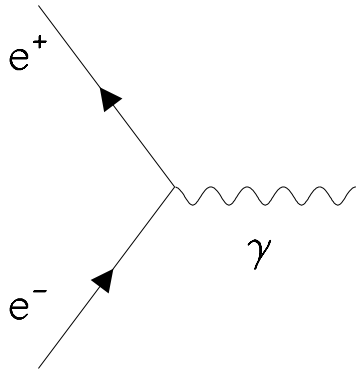

Figure 1.3: *Feynman diagram for the annihilation of an electron and a positron into a photon.*

charge, giving the weak bosons non-zero masses and allowing particles with weak charge to have mass. Thus, the differences in mass between the up and down quarks can be attributed to their weak charges. We separate weak charge into 'up' and 'down' charge, corresponding to the respective weak charges of the up and down quarks.

We can represent the annihilation of up and down quarks into weak gauge bosons by:[2]

$$(\,\bar{u}_{\bar{u}} \quad \bar{d}_{\bar{d}}\,) \begin{pmatrix} Z^0_{\bar{u}u} & W^+_{\bar{d}u} \\ W^-_{\bar{u}d} & Z^0_{\bar{d}d} \end{pmatrix} \begin{pmatrix} u_u \\ d_d \end{pmatrix}.$$

Figure 1.4 shows the formation of a $W^{\pm}$ by an up quark interacting with

[2]There are four particles in the gauge boson matrix, but the two Z^0 particles shown are actually the same particle.

an antidown quark. As with gluons, the $W^{\pm}$ and Z^0 carry the charge of the force they mediate; thus, they can interact with themselves, resulting in Feynman diagrams with three or four gauge bosons meeting at a vertex. And because of the unification of the electromagnetic and weak interactions, photons can interact directly with $W^{\pm}$ particles (but not with Z^0 particles, since they do not carry any electric charge).

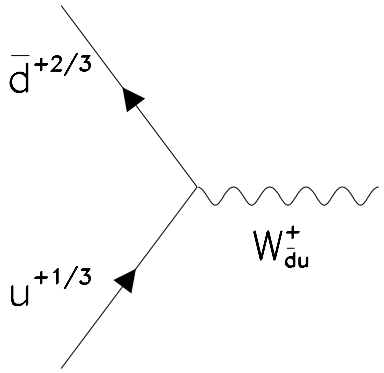

Figure 1.4: *Feynman diagram for the annihilation of an up quark and an antidown quark into a* W^+.

All of the quarks and leptons can be organized into weak doublets (Table 1.2), furthering our understanding of the fundamental particle spectrum.

Quarks			Leptons		
$\begin{pmatrix} u^{+2/3} \\ d^{-1/3} \end{pmatrix}$	$\begin{pmatrix} c^{+2/3} \\ s^{-1/3} \end{pmatrix}$	$\begin{pmatrix} t^{+2/3} \\ b^{-1/3} \end{pmatrix}$	$\begin{pmatrix} \nu_e^0 \\ e^- \end{pmatrix}$	$\begin{pmatrix} \nu_\mu^0 \\ \mu^- \end{pmatrix}$	$\begin{pmatrix} \nu_\tau^0 \\ \tau^- \end{pmatrix}$

Table 1.2: *The fundamental particles of matter, organized by participation in strong interactions and by weak particle doublets; the superscripts indicate each particle's electric charge. There are three sets each of lepton and quark doublets, resulting in three particle 'generations.' We do not show the antiparticles, which have the same masses and opposite charges of the corresponding particles.*

1.2.3 The Higgs Particle

The 1980's brought confirmation of the electroweak theory through the observations of the W and Z particles and the measurements of their masses [24]. The 1995 discovery of the top quark [25] and the 2000 observation of the tau neutrino [26] completed the set of fundamental particles shown in Table 1.2. At this point, all of the Standard Model fundamental particles, including the gauge bosons, have been found. Except one.[3]

While the gauge field theory description of the strong and electroweak forces has been overwhelmingly successful, it contains a key feature that requires the existence of a new particle. In a gauge field theory, fundamental particles can only acquire mass through interactions with a 'scalar' particle [28], which is a particle without spin and without a preferred direction in space (to be compared

[3]Experiments completed in early 2001 at the Large Electron Positron collider in Switzerland (LEP) strongly suggest the existence of the last particle, a 'Higgs' with a mass of approximately 115 GeV/c^2 [27].

with a 'vector' particle, which does have a preferred direction in space). The scalar particle can either be fundamental (the 'Higgs' particle), or it can be a composite of two or more fundamental particles bound together by a new force called 'technicolor' [29]. There have been no observed scalar fundamental particles, but scalar composite particles bound by the strong force have been observed (the pion is an example). The known scalar particles can not account for the masses of the fundamental particles, however, since they would give the $W^{\pm}$ and Z^0 masses of only about 30 MeV/c^2 (compared with their observed masses of 80 and 91 GeV/c^2; see Table 1.3). If composite scalar particles provide mass to the fundamental particles, they must be bound by a force considerably stronger than the strong force, and must have masses of at least a few hundred GeV/c^2.

Quarks		Leptons		Vector Bosons	
Particle	Mass	Particle	Mass	Particle	Mass
u	1 to 5 $\times 10^{-3}$	ν_e	$< 3 \times 10^{-9}$	gluon	0
d	3 to 9 $\times 10^{-3}$	e	5.11×10^{-4}	γ	0
c	1.15 to 1.35	ν_μ	$< 1.9 \times 10^{-4}$	$W^{\pm}$	80.419
s	0.075 to 0.175	μ	0.106	Z^0	91.188
t	174.3	ν_τ	$< 1.82 \times 10^{-2}$		
b	4.0 to 4.4	τ	1.78		

Table 1.3: *The masses of the fundamental particles, in units of GeV/c^2 [30].*

1.3 Beyond the Standard Model

The Standard Model vastly improves our understanding of the fundamental particles and the forces of nature. The particles are neatly divided into matter and force-carrying particles, with the matter particles organized by their participation in the strong and weak interactions. The Standard Model offers a powerful organizational structure, which in fact suggests the existence of further connections between the particles and the forces.

1.3.1 Grand Unification

The successful merging of the electromagnetic and weak theories leads naturally to the idea of a similar merging of the electroweak and strong theories. In 1974, Sheldon Glashow and Howard Georgi made one of the first attempts at a 'Grand Unified Theory' [31], which describes the electroweak and strong forces as different manifestations of a single 'elec-stro-weak' force.

In a unified theory, there is only one type of charge, which we can take to be an expanded color charge. Thus, we can call the up and down flavor charges of the weak force 'orange' and 'yellow' charges in our elecstroweak force. Then we can write interactions in terms of a larger set of gluons, which carry the new color

charges as well as the standard QCD charges:[4]

$$(\,\bar{d}_{\bar{r}} \quad \bar{d}_{\bar{b}} \quad \bar{d}_{\bar{g}} \quad (\bar{\nu}_e)_{\bar{o}} \quad \bar{e}_{\bar{y}}\,) \begin{pmatrix} \begin{pmatrix} g_{\bar{r}r} & g_{\bar{b}r} & g_{\bar{g}r} \\ g_{\bar{r}b} & g_{\bar{b}b} & g_{\bar{g}b} \\ g_{\bar{r}g} & g_{\bar{b}g} & g_{\bar{g}g} \end{pmatrix} & \begin{pmatrix} g_{\bar{o}r} & g_{\bar{y}r} \\ g_{\bar{o}b} & g_{\bar{y}b} \\ g_{\bar{o}g} & g_{\bar{y}g} \end{pmatrix} \\ \begin{pmatrix} g_{\bar{r}o} & g_{\bar{b}o} & g_{\bar{g}o} \\ g_{\bar{r}y} & g_{\bar{b}y} & g_{\bar{g}y} \end{pmatrix} & \begin{pmatrix} g_{\bar{o}o} & g_{\bar{y}o} \\ g_{\bar{o}y} & g_{\bar{y}y} \end{pmatrix} \end{pmatrix} \begin{pmatrix} d_r \\ d_b \\ d_g \\ (\nu_e)_o \\ e_y \end{pmatrix}.$$

The 'gluons' containing only orange and yellow colors (lower right-hand corner) correspond to the $W^{\pm}$, Z^0 and γ; the gluons containing only red, blue, and green colors (upper left-hand corner) correspond to the standard gluons of QCD. There are a new set of gluons, which contain one weak color and one strong color (lower left and upper right). These gluons allow for direct interactions between leptons and quarks, and they are thus known as 'leptoquarks' (LQ). Figure 1.5 shows an example of this type of interaction, specifically an antired antidown quark combining with an orange electron neutrino to form an orange and antired leptoquark.

1.3.2 Horizontal Gauge Bosons

The unified model proposed by Georgi and Glashow has been ruled out by experiment [32], likely because there exist additional connections between the

[4] While there are twenty-five entries in the vector boson matrix, only 24 of them are independent and correspond to unique particles.

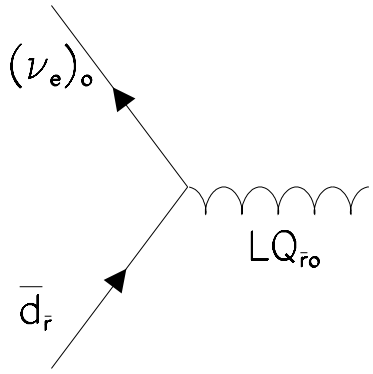

Figure 1.5: *Feynman diagram for the combination of an antired antidown quark with an orange electron neutrino, resulting in an orange and antired leptoquark.*

particles that are not included in the model. One such connection could be a force linking the three generations of particles [33].

We have seen how the particles in the sets of six quarks and six leptons can be paired into weak doublets, and how the quarks and leptons can be linked by a unifying force. However, the unified model of Georgi and Glashow does not connect the particles in different generations. Such a connection would require a new force, similar to the weak force but with heavier vector bosons (H). If we call the force charges 'horizontal' charges, and label them left (l), middle (m), and right (r), we can write the possible interactions between generations in matrix

form:

$$\left(\bar{u}_{\bar{l}} \quad \bar{c}_{\bar{m}} \quad \bar{t}_{\bar{r}} \right) \begin{pmatrix} H_{\bar{l}l} & H_{\bar{m}l} & H_{\bar{r}l} \\ H_{\bar{l}m} & H_{\bar{m}m} & H_{\bar{r}m} \\ H_{\bar{l}r} & H_{\bar{m}r} & H_{\bar{r}r} \end{pmatrix} \begin{pmatrix} u_l \\ c_m \\ t_r \end{pmatrix} .$$

The horizontal force has the appeal of explaining the generational structure of the fundamental particles, and it has the potential to explain the mass differences of particles in different generations.

1.3.3 Compositeness

Murray Gell-Mann was led to his description of hadrons as quark bound states by the structure the bound states displayed. Similarly, the structure of the current set of 'fundamental' particles might simply be due to a substructure of constituent particles [34]. In this case, there would be a new, very strong, force binding the constituent particles together. All of the known particles would be composites of a small number of fundamental particles, and the particle generations would arise from the different energy states of the bound particle systems.

1.3.4 Left-Right Symmetry

The W and Z particles contain a peculiar feature in that they only interact with 'left-handed' quarks and leptons. A quark or lepton can be either left-handed or right-handed, depending on the direction of its spin: If the particle is moving

in the direction of a hand's thumb, the particle is left-handed if its spin is in the direction of the curled fingers of the left hand, and it is right-handed if its spin is in the direction of the curled fingers of the right hand. The interactions of gluons and the photon do not contain any handedness bias, suggesting that a right-handed version of the weak interactions might exist [35]. This would introduce a new force, with new (heavier) vector bosons. Then, but for the non-zero masses of the vector bosons, the weak force would look much like the strong and electromagnetic forces.

1.3.5 Supersymmetry

If a fundamental scalar Higgs particle exists, it would be natural to expect other fundamental scalar particles to exist. The theory of supersymmetry [36] predicts such particles. In supersymmetry, a symmetry exists between the fermion particles (quarks and leptons) and the scalar particles: For every fermion particle there is a corresponding scalar particle.[5] The symmetry extends to the gauge bosons, so that there is a fermion particle for every vector boson. Supersymmetry has the dual appeal of extending the symmetries of nature and forming the basis of string theory, a fundamental theory which incorporates all of the forces of nature.

[5]More precisely, supersymmetry postulates a scalar particle for each fermion degree of freedom.

1.3.6 String Theory

The gauge field theory description of the electroweak and strong forces has been an incredible success, leading to the development of the Standard Model, a model tested and verified by a wide variety of phenomena. However, the Standard Model (and, fundamentally, the gauge field theory description) has one glaring weakness: It fails to incorporate gravity. This failure has not affected previous tests of the Standard Model because gravity is so much weaker than the other forces that it can be neglected. Eventually, however, as the energies of our tests increase, the effects of gravity will become apparent.

The only current theory that can incorporate gravity is string theory [37]. String theory describes all matter particles as one dimensional loops, rather than the zero dimensional points of field theory. It predicts the graviton, the mediator of the gravitational force. It also predicts an additional six or seven dimensions beyond the four observed space-time dimensions. Such extra dimensions could exist if they are curled in on themselves, rather than extending linearly in the manner of the familiar dimensions.

1.4 Discovering New Physics

The Standard Model's structure suggests the existence of additional unobserved structure that would result in new particles and forces. The discovery of such 'new physics' could trigger another avalanche of particle discoveries and categorization (akin to the events of the 1960's), ultimately resulting in a broader, more comprehensive model. In fact, the development of the next-generation Standard Model *requires* such an avalanche of discoveries, making the search for new physics one of the most vigorous pursuits of particle physicists today.

The key to discovery lies in observing high energy interactions, which can produce the new heavy particles not prevalent on Earth (such as the top quark). To produce and observe these high energy interactions, we use accelerator and detector technology developed through the course of the twentieth century.

1.4.1 Accelerators

The early study of high energy interactions relied solely on the occurance of these interactions in nature. While these studies resulted in significant scientific breakthroughs (such as the discovery of the atomic nucleus by Ernest Rutherford [38]), they suffered the significant drawback that scientists could not control when and where they would occur. The development of high energy accelerators in the twentieth century gave us the power to initiate high energy interactions, allowing

for control of such factors as their energy and frequency of occurence.

The first accelerator, designed by Cockcroft and Walton in 1932 [39], consisted of a multi-stage circuit with a large energy difference between two endpoints. Because of the intermediate stages, more than a million volts could be generated using capacitors and diodes. Subsequent accelerator designs utilized the idea of increasing energy in stages, with one twist: Rather than using *internal* stages to produce a single energy difference between two points, contemporary accelerators use *external* stages to provide multiple smaller energy increases to particles. This advance was crucial to increasing the energy threshold of accelerators, as accelerators with a single energy difference encounter problems of insulation breakdown at high energies (about 50 MeV) [40].

A few months after the Cockcroft-Walton debut, Ernest Lawrence began operation of the *cyclotron* [41], an accelerator providing multiple small energy boosts to protons. In a cyclotron, protons revolve in a magnetic field and pass through an electric field every half revolution. The electric field increases the protons' energy and, consequently, the radius of their circular motion, causing the protons to spiral outward until they reach the cyclotron's outer edge. At that point, the protons are released from the cyclotron and collide with a fixed target. While inside the cyclotron, the protons revolve with constant frequency, and the electric field oscillates with that frequency. This equality holds as long as the proton-

s' velocities are much less than that of light; at high velocities the frequency of revolution changes with each energy boost, destabilizing the proton beam. Thus, cyclotrons cannot accelerate protons to kinetic energies close to the proton's rest mass of a billion electron volts (GeV).

The accelerator energy barrier was broken in 1945, when McMillan and Veksler independently suggested varying the frequency and shifting the phase of the oscillating electric field [42]. Using the proper combination of these adjustments, the next wave of particle accelerators ('synchrotrons') produced stable beams of particles revolving at a fixed radius. By the early 1950's, synchrotrons could produce proton beams with energies in excess of 6 GeV [43].

Another important advance in accelerator technology occured in 1952 with the development of strong focusing [44]. Strong focusing improves the longitudinal stability of the beam by alternately focusing and defocusing the beam in each transverse direction. Accelerators utilizing this technology acclerated protons to energies of 33 GeV in the early 1960's [45] [46].

The final critical accelerator development came in the ability to collide two high energy beams [47]. In a collision of two beams with equal and opposite momentum, the full energy of the beams can be used to create new particles, since the net momentum in the initial collision is zero. Previous collisions of a single beam on a fixed target allowed for the production of new particles with

masses of only a fraction of the beam energy, since the conservation of momentum required a significant portion of the energy to go to the momentum of the produced particles.

Armed with this technological capacity, scientists in the early 1970's completed the Fermilab accelerator in Batavia, Illinois, with 400 GeV proton beams [48]. By the late 1980's, Fermilab could produce proton-antiproton collisions with beams of 900 GeV each (or up to 1.8 TeV of energy available for the production of new particles) [49]. Figure 1.6 shows the historical increase in proton beam energy with time.

1.4.2 Detectors

With the ability to produce interactions of high energy and frequency came the need for improvements in the detection of the products of these interactions. The initial Cockcroft-Walton experiment in 1932 measured outgoing particles with energies of a few MeV up to 50 times per second; the detectors at the Fermilab Tevatron in 2001 measure outgoing particles with energies up to a few hundred GeV more than 2 million times per second [50].

The original Cockcroft-Walton detector system consisted of a zinc sulfide scintillator, a microscope, and the human eye. When a particle bombarded the scintillator, it radiated visible light, which was observed through a microscope. This

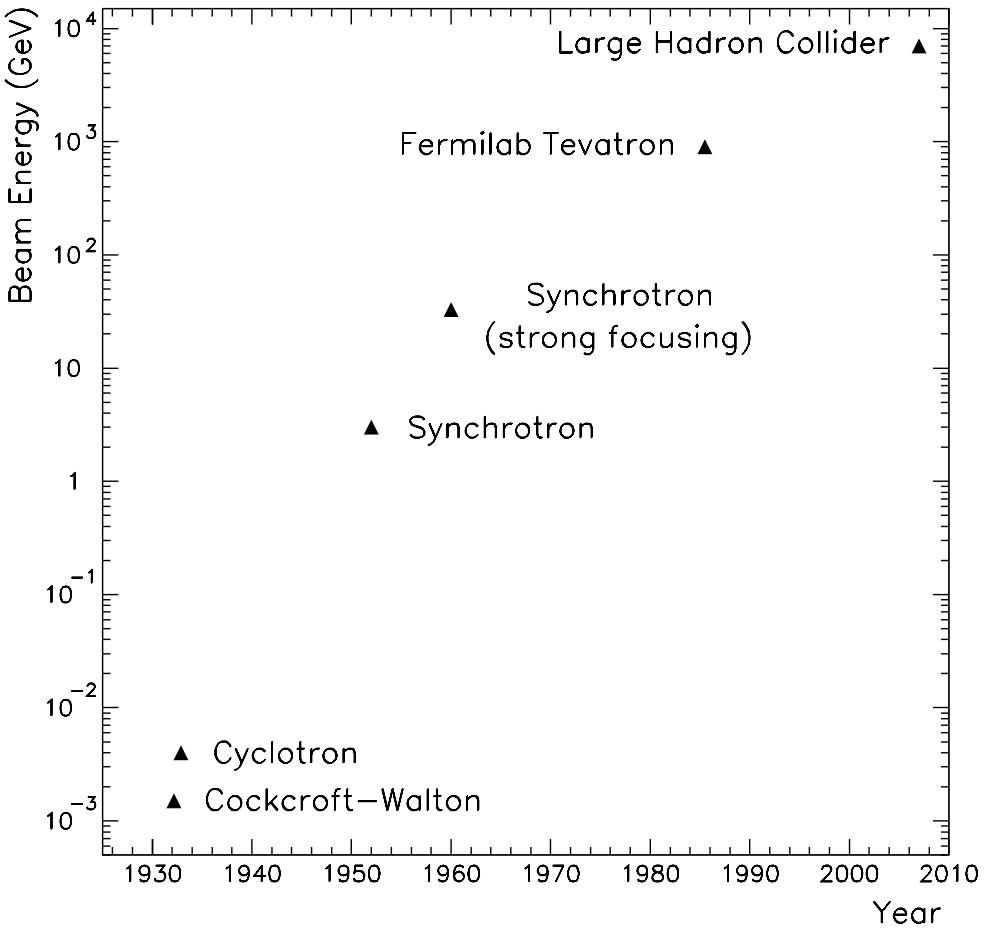

Figure 1.6: *The historical increase in proton beam energy with each accelerator advance [46]. We show the most recent synchrotron, the Fermilab Tevatron, which is the highest energy accelerator to date. Its energy will be surpassed, however, by the Large Hadron Collider at* CERN *in Switzerland.*

method worked for measuring a few particles per minute, but not for a few particles per second. For higher rates, Cockcroft and Walton used an ionization chamber: Particles impinging on the chamber released electrons, resulting in an electronic signal after amplification. This arrangement allowed for the observation of more than thirty particles per second. Cockcroft and Walton could determine the energies of the outgoing particles by measuring the thickness of mica required to completely stop the particles; the knowledge of the rate of energy loss in mica allowed an inference of the initial energy of the particles.

Contemporary detectors use many of the same principles of the Cockcroft-Walton detector, with a few significant improvements. Rather than being confined to a small region a short distance from the interaction, today's detectors surround the interaction point, with only small regions where particles can escape. This increase in geometrical coverage significantly increases the percentage of interactions observed. In addition, contemporary detectors measure the paths of charged particles using ionization chambers with closely spaced wires. To measure a particle's energy, detectors frequently use scintillators, since the energy is proportional to the intensity of light emitted in the scintillator. In order to keep the size of the detectors practical, the scintillators are interspersed with a stopping material to confine the particles within the detector. Additional energy measurements can be made by measuring the curvatures of the charged particles' paths in a magnetic

field.

The advances in detector technology, coupled with those in accelerator technology, allow us to search for new particles using interaction energies high enough to produce particles (like the top quark) several hundred times heavier than the proton. This thesis searches a data set taken with the highest energy accelerator induced interactions to date for evidence of new particles and forces.

Chapter 2

Phenomenology

To discover new physics, we choose initial and final states in which new processes can occur. We study an initial state of proton-antiproton ($p\bar{p}$) collisions with a center of momentum energy of 1.8 TeV (the condition produced by the Fermilab Tevatron). This large energy allows for the production of such heavy objects as W and Z bosons and the top quark; if new particles exist in this mass region, our initial state should result in their production (Fig. 2.1).

We choose a final state of 2 hadronic jets and missing transverse energy based on the potential for the observation of new physical processes and on the low Standard Model backgrounds. The 2 jets + $\not\!\!E_T$ final state arises from the production of 2 quarks or gluons (or a combination of both) in association with at least one unobserved particle. The production of quarks or gluons results in observed 'jets'

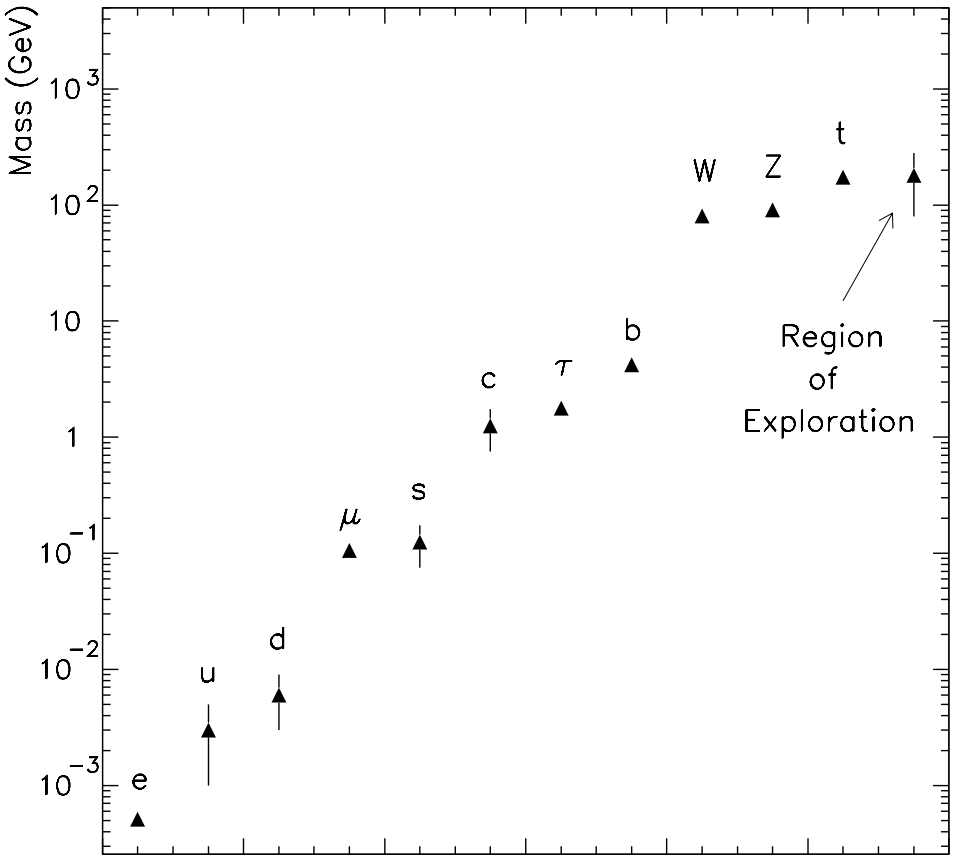

Figure 2.1: *The mass spectrum of the fundamental particles and the region of exploration of the current search. We do not show the massless particles (photon, graviton and gluons) or the neutrinos, whose masses have yet to be measured.*

of hadrons spraying through the detector. The production of a weakly interacting undetected particle (such as a neutrino) results in the measurement of unbalanced energy in the direction transverse to the initial accelerator beam direction (this unmeasured energy is known as the 'missing transverse energy,' or $\not\!\!E_T$).

The source of $\not\!\!E_T$ in new physical processes can be neutrinos or new weakly interacting particles. The observation of new weakly interacting particles would have far-reaching consequences, as they could be responsible for significant quantities of unobserved mass in the universe, thus affecting its underlying geometrical structure (such mass is known as 'dark matter'). The observation of new particles decaying to neutrinos would be equally significant, as they would require the existence of a new force.

The Standard Model backgrounds to the 2 jets + $\not\!\!E_T$ final state arise from W or Z production in association with jets, top quark production, and multijet production with detector measurement errors (Chapter 6). These processes occur at a low enough rate for new processes to be observable.

2.1 New Physics Models

Based on our selection of the 2 jets + $\not\!\!E_T$ final state, we can categorize the types of new physics we might observe. We assume the new physics will be identifiable by the production of new heavy particles or by the excessive production of known

particles. The particle production can occur in pairs or as individual 'resonances.' The particle decay products constitute our final state.

If there are two particles produced in the interaction, there are two classes of decays that can result in the 2 jets + $\not\!\!E_T$ final state: Both particles can decay into a quark (or gluon) and an unobserved particle; or one particle can decay into unobserved particles and the other can decay into quarks or gluons (or a combination of both). Leptoquark, technicolor, and supersymmetric top production models are examples of the former class; WZ, HZ, W', and graviton production models are examples of the latter class. We describe these models in the following sections.

2.1.1 Leptoquark Production

The leptoquarks of Grand Unified Theories [31] are examples of particles that connect the lepton and quark sectors. In addition, there are other types of leptoquarks that might exist [51]. For example, leptoquarks might be scalar Higgs [52] or composite [53] particles. Or, the coupling between vector leptoquarks and the other matter particles can be different from that of a Unified Theory. We separate leptoquark models into scalar and vector leptoquark models, and we examine several possibilities for the coupling of the vector leptoquarks to other matter particles.

All leptoquarks share the same production mechanism, given the initial state of $p\bar{p}$ collisions. Leptoquarks are produced predominantly in pairs, via the exchange of strong color charge. The dominant Feynman diagrams for leptoquark production are shown in Fig. 2.2; we do not show the color charge, as there are a number of possible combinations of color exchange. The first diagram describes leptoquark and antileptoquark production through the annihilation of a quark and an antiquark; the other 4 diagrams describe leptoquark and antileptoquark production through the fusion of 2 gluons.

Given these production diagrams, we can calculate the production rate of leptoquarks. The rate per collision, multiplied by the number of collisions, gives us the prediction for the number of leptoquarks produced at the collider. We express the rate in terms of the effective cross sectional area per collision, or 'cross section.' We multiply the cross setion by the number of collisions per cross sectional area (the 'luminosity') to determine the total number of leptoquarks produced. We show the cross sections for different scalar leptoquark masses in Table 2.1 (the high and low cross sections shown in the Table are due to theoretical uncertainties). These cross sections include 'next-to-leading order' (NLO) diagrams (Fig. 2.3), which have one more vertex than those shown in Fig. 2.2 (each additional vertex reduces the contribution of the diagram, so that NLO diagrams contribute only a small percentage to the overall cross section). The cross section units of picobarns

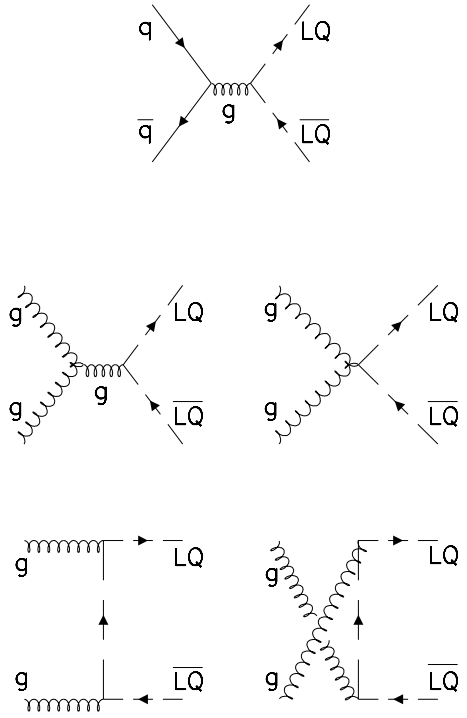

Figure 2.2: *Leading order Feynman diagrams for leptoquark production. The diagrams include all possible color exchanges, which we do not show explicitly.*

(pb) are equivalent to 10^{-36} cm^2. For reference, we have 85.2 pb^{-1} of luminosity in our data set (Section 5.2.2); thus, our data corresponds to the production of about 400 scalar leptoquarks, if they exist and have a mass of 120 GeV.

The production cross sections of vector leptoquarks are complicated by a freedom in the type of interaction (or 'coupling') between leptoquarks and gluons. The leptoquarks of Grand Unified Theories are gauge bosons, and their couplings are known as Yang-Mills (YM) couplings [18]. In principle, leptoquarks and glu-

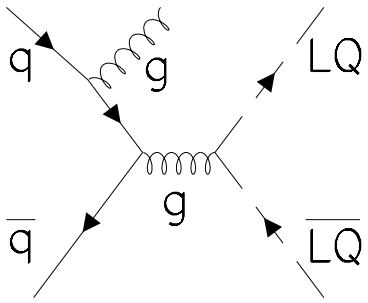

Figure 2.3: *An example of a next-to-leading order Feynman diagram for leptoquark production. The diagram shows a gluon radiated by an incoming quark in a process known as 'gluon bremsstrahlung.'*

M_{SLQ} (GeV)	σ (pb)	σ_{high} (pb)	σ_{low} (pb)
80	43	49	36
100	13	14	11
120	4.5	5.0	3.8
140	1.8	2.0	1.5

Table 2.1: *The cross sections for the pair production of scalar leptoquarks in 1.8 TeV $\sqrt{s}$ $p\bar{p}$ collisions [54]. We assume each leptoquark decays exclusively to a quark and a neutrino.*

ons could have a different type of coupling that depends on the momenta of the outgoing leptoquarks. An example of this is a coupling known as 'Minimal Coupling' [55]. The most general couplings include a combination of Yang-Mills and Minimal Coupling contributions. One can determine the *minimum* number of vector leptoquarks that would be produced at the Tevatron by finding the minimum cross section with respect to these coupling terms. These minimum cross

sections are shown in Table 2.2. In general, vector leptoquarks are produced more copiously than scalar leptoquarks; our data corresponds to the production of at least 2,500 120 GeV vector leptoquarks, if they exist.

M_{VLQ} (GeV)	σ (pb)	σ_{high} (pb)	σ_{low} (pb)
120	29	46	18
140	9.4	16	6.3
160	3.0	4.9	2.0
180	1.3	1.9	0.80

Table 2.2: *The cross sections for the pair production of vector leptoquarks in 1.8 TeV $\sqrt{s}$ $p\bar{p}$ collisions [56]. We assume each leptoquark decays exclusively to a quark and a neutrino.*

If leptoquarks are produced in the initial state $p\bar{p}$ collisions, they will decay before traveling a significant distance as long as their coupling strengths are not significantly weaker than the electroweak coupling strength (a reasonable assumption, particularly if the leptoquarks are gauge bosons in a Unified Theory). In general, a leptoquark can decay to any lepton and quark combination, but for leptoquarks with masses below about 1 TeV, the lepton and quark must be in the same generation [57]. Since we have no observed leptons in our final state, we are most sensitive to the case where both leptoquarks decay into a quark and a neutrino, allowing us to observe leptoquarks of any generation.

The leptoquark model provides an example of a fundamental interaction that produces 2 new heavy particles, each of which decays into a quark and an un-

measured particle. It gives us a specific model that can be generalized to a wider variety of new physics.

2.1.2 Techniparticle Production

Technicolor models possess a wide range of new particles and a variety of production modes resulting in the 2 jets + $\not\!\!E_T$ final state. The mode with the largest cross section is the production of one of eight technirho particles (ρ_{T8}), which are bound states of techniquarks and possess the same color charges as gluons [58]. A technirho decays into 2 technipions, as long as the technirho mass is at least twice that of the technipion. The technipions (π_T) can have various modes of decay, 2 of which correspond to those of scalar leptoquarks: $c\nu_\tau$ and $b\nu_\tau$. The production cross section varies with the masses of the techniparticles; for 550 GeV technirhos and 200 GeV technipions, the cross section is 2 pb, corresponding to the production of over 170 technirhos in our data set.

In addition to the above decay modes, technirho production can result in a 2 jets + $\not\!\!E_T$ final state via 2 other decay modes: $Z^0\pi_T$ and $W^\pm Z^0$. In both of these modes, the Z decays to neutrinos and the other particle decays to quarks or gluons.

Since techniparticles possess a variety of production modes, our direct search for leptoquark and WZ production provides sensitivity to the production of tech-

niparticles. Thus, although we do not directly search for techniparticles, we can observe them if they exist.

2.1.3 Supersymmetric Top Production

The supersymmetric partner to the top quark (the 'stop') is expected to be the lightest superymmetric quark [59]. Stops are produced in pairs in $p\bar{p}$ collisions via $q\bar{q}$ annihilation and gluon fusion. In certain models, each stop particle decays to a charm quark and the lightest supersymmetric particle. If supersymmetric particle number is conserved, the lightest supersymmetric particle can not decay and it passes unmeasured through the detector, resulting in $\not\!\!E_T$. Thus, stop pair production results in a 2 jets + $\not\!\!E_T$ final state in a manner analagous to leptoquarks: Stops are produced in pairs, with each particle decaying to a quark and an unidentified particle. The only difference is that the unidentified particle is massless in the case of the leptoquark, while it can be tens of GeV (or more) in the case of the stop. The cross section of stop production varies by model; many models predict the production of 150 GeV stops with a cross section of about 0.6 pb; this corresponds to about 50 stop pairs in our data set [60].

2.1.4 WZ Production

In the Standard Model, 1.8 TeV $\sqrt{s}$ $p\bar{p}$ collisions result in direct WZ production with a cross section of 2.5 pb (the production diagrams are shown in Fig. 2.4) [61]. WZ production results in a 2 jets + $\not\!\!E_T$ final state when the W decays to a quark and anti-quark and the Z decays to a neutrino and anti-neutrino. These requirements reduce the WZ cross section to 0.33 pb; thus, we expect fewer than 30 WZ events produced in our data set. While this is too few for observation, non-Standard Model couplings [62], techniparticle production (Section 2.1.2), and W' production (Section 2.1.6) can significantly increase WZ production. Thus, a search for WZ events provides a broad test of new physics.

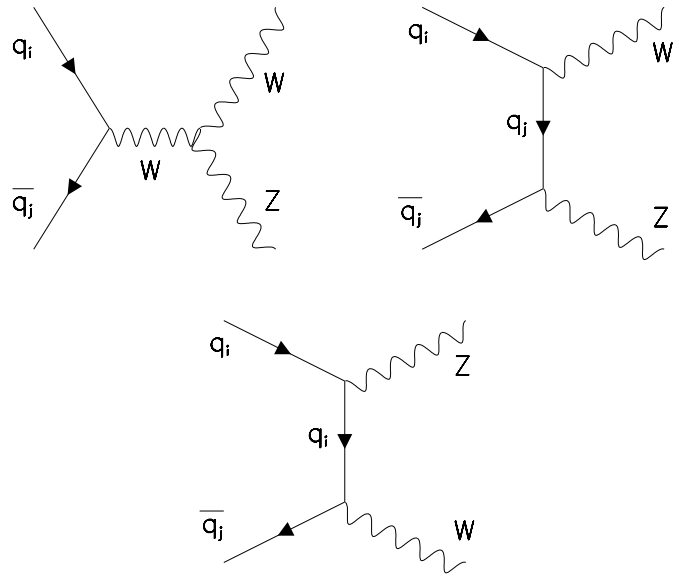

Figure 2.4: *Leading order Feynman Diagrams for WZ Production.*

2.1.5 HZ Production

Higgs particle production results in a 2 jets + $\not\!\!E_T$ final state when the Higgs is accompanied by a Z. The Higgs decays with high frequency (70% for a 120 GeV Higgs) to a $b\bar{b}$ pair, while nearly 20% of the Z decays are to a neutrino and an anti-neutrino. Including these branching ratios, the Standard Model cross section for HZ production is about 0.015 pb [63], corresponding to just 1.3 events in our data set.

2.1.6 W' Production

Heavy charged gauge bosons (W') coupling only to right-handed particles can decay into WZ pairs [64]. We can estimate the number of W' particles in our data set by assuming that their interactions with the W and Z bosons have the same strength as the Standard Model W and Z couplings, with a multiplicative factor determined by the mass of the W'. We can express this factor as a 'mixing angle' between the W' and the W, with the assumption that this angle is equal to $(M_W/M_{W'})^2$. The cross sections for several W' masses are shown in Table 2.3; the branching ratios of W' to WZ, W to jets, and Z to $\not\!\!E_T$, are included in the cross sections. For a 300 GeV/c^2 W', our data set corresponds to the production of nearly 180 W' events.

$M_{W'}$ (GeV)	$\sigma \times$ BR (pb)
200	6.5
300	2.1
400	0.39

Table 2.3: *The cross sections for W' production in 1.8 TeV $\sqrt{s}$ $p\bar{p}$ collisions. We include the branching ratio for W' decays resulting in the 2 jets + $\not\!\!E_T$ final state.*

2.1.7 Graviton Production in Extra Dimensions

The most striking prediction of string theory is the existence of extra dimensions. Such dimensions can escape our perception, and all existing tests of gravity, if their sizes are less than about 200 μm [65]. If there are at least three extra dimensions, the Tevatron's energy of 1.8 TeV could be sufficient to probe these dimensions [66].

In models with extra dimensions, the Tevatron can produce gravitons through their radiation by a gauge boson, or directly through $q\bar{q}$ annihilition. In the case where the graviton is radiated by a gauge boson, the graviton can travel into the extra dimensions and disappear, resulting in $\not\!\!E_T$. For gauge bosons decaying into two jets, the final state is 2 jets + $\not\!\!E_T$; some example diagrams for this process are shown in Fig. 2.5.

The production of gravitons and W or Z particles is similar to WZ production; thus, by searching for WZ production, we are sensitive to the production of

gravitons escaping into extra dimensions.

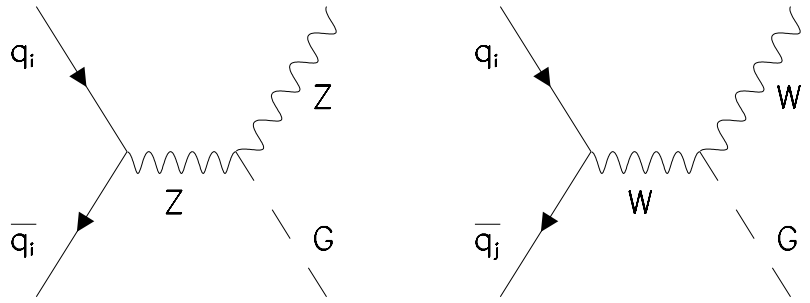

Figure 2.5: *Example Feynman Diagrams for Graviton plus W or Z Production.*

2.2 Distinguishing New Physics

The 2 jets + $\not\!\!E_T$ final state is an excellent probe for new physics, and by searching for leptoquark and WZ production, we are sensitive to a wide variety of new physical processes. If our search results in an observed excess in the data that is inconsistent with the Standard Model, the next step will be to determine the precise nature of the new physics we have discovered. By studying the cross section and characteristics of the excess, and through the analysis of different final states, we will be able to distinguish the precise nature of the new physics.

Chapter 3

Experimental Apparatus

We produce our data set using two major instruments: The Fermilab accelerator system, which creates the 1.8 TeV center of momentum energy $p\bar{p}$ initial state collisions; and the DØ detector, which measures the final state particles.

3.1 The Fermilab Accelerator

The accelerator [67] consists of several stages that progressively increase the energy of the protons and antiprotons. The different stages utilize different apparatuses to accomplish the acceleration: The first stage (preacceleration) occurs via a magnetron source and a Cockcroft-Walton generator; the next stage uses a linear accelerator; and the final three stages (the Booster, Main Ring, and Tevatron) use proton synchrotrons. Only protons are accelerated until the final two

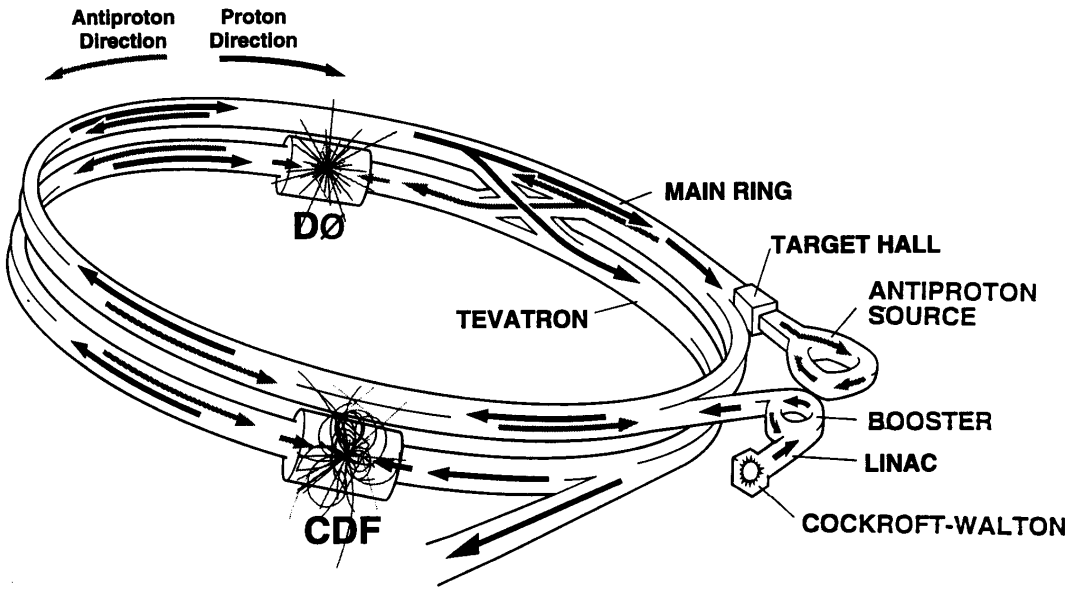

Figure 3.1: *The Fermilab accelerator system.*

stages, at which point antiprotons are produced and subsequently accelerated. Figure 3.1 shows a schematic drawing of the accelerator system.

3.1.1 The Preaccelerator

The acceleration process begins with the release of hydrogen gas into a 'magnetron surface-plasma source' (Fig. 3.2), which adds electrons to the hydrogen atoms. The magnetron source uses an electric field to attract protons to the surface of a cathode. The protons collect electrons from the cathode and are disengaged by the stream of bombarding atoms. If the protons are released with two

electrons, they have a net negative charge and a magnetic field causes them to spiral out the opposite side of the magnetron source. An 'extractor plate' accelerates the ions to a kinetic energy of 18 keV, and a Cockcroft-Walton generator provides an additional acceleration to a kinetic energy of 750 keV.

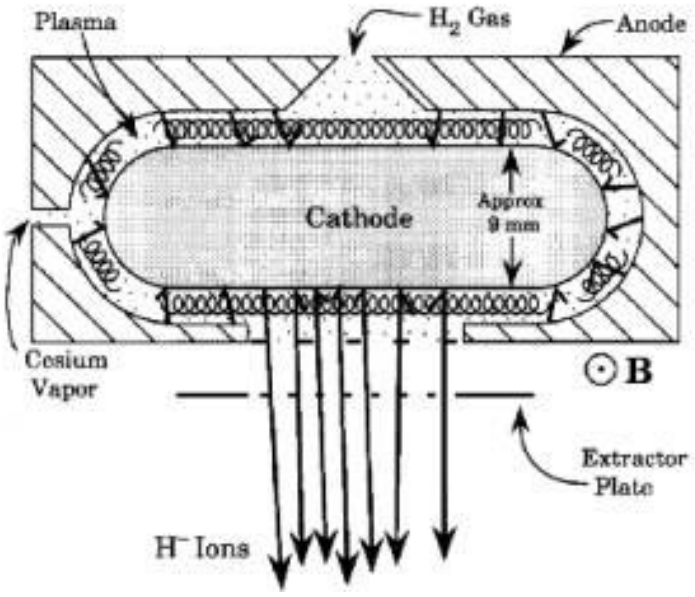

Figure 3.2: *The magnetron source used to create negatively charged hydrogen ions from hydrogen gas.*

3.1.2 The Linac

The linear accelerator (or Linac) consists of two segments: The first segment accelerates incoming negative hydrogen ions from a kinetic energy of 750 keV to a kinetic energy of 116 MeV; the second segment boosts the 116 MeV ions to 400 MeV.

Both segments use the same method of acceleration. An electric field pulls a group of ions through a beam tube. The field then switches polarity, preventing more ions from entering the tube. This use of alternating fields produces a localized 'bunch' of ions, rather than the steady stream coming out of the preaccelerator. After accelerating through the electric field, the ion bunch coasts through a shielded drift tube, continuing through the accelerator during the electric field reversal. When the ions reach the end of the tube, the electric field reverses again, providing another incremental boost to the ions. This step by step increase in acceleration occurs in both segments of the linear accelerator over a distance of 130 meters, until the ions have a kinetic energy of 400 MeV.

3.1.3 The Booster

The 400 MeV ions produced by the Linac enter the Booster, a circular synchrotron nearly half a kilometer around. The ions are 'debunched,' returning the beam to a steady stream of particles. The beam passes through a thin carbon foil, which removes the loosely bound electrons from the proton while negligibly affecting the proton's motion. The steady beam of protons travels around the Booster, collecting more protons with each turn. After six revolutions, the Booster contains about three trillion (3×10^{12}) protons, and the Linac ceases its supply. The Booster then restores the bunch structure to the beam and accelerates the

protons to an energy of 8 GeV.

When the proton energy reaches 4.2 GeV, a precise 'transition' in the alternating electric fields must occur in the Booster to keep the beam stable. Before the transition, a set of magnets along the beam line keeps the protons in orbit, and the alternating electric field forces the protons into bunches. However, at the transition energy, the bunch structure would destabilize without a precise shift in the timing of the alternating electric field cycle. The Booster institutes this shift, but during its application the proton beam undergoes a brief moment of instability.

3.1.4 The Main Ring

When the Booster achieves 8 GeV proton bunches, it injects the protons into the Main Ring, a proton synchroton 6.3 kilometers around. The Main Ring serves two purposes: It provides a 120 GeV proton beam for the production of antiprotons; and it accelerates protons and antiprotons from an energy of 8 GeV to an energy of 150 GeV.

The production of antiprotons occurs via the impingement of 120 GeV protons on a nickel target disk. For every hundred thousand (10^5) protons colliding with the disk, one antiproton results. Two synchrotons debunch and accumulate the produced antiprotons, creating a beam of 8 GeV antiprotons. The accumulator

then bunches the antiprotons and injects them into the Main Ring.

The larger the number of protons and antiprotons in a bunch, the larger the luminosity of collisions, and thus the better the chance of producing new particles. In order to increase the numbers of protons and antiprotons in their respective bunches, the Main Ring coalesces groups of fifteen proton bunches and eleven antiproton bunches; these are the largest groups that can be coalesced while keeping the beams stable. After the coalescing procedure, proton bunches contain 150 billion (1.5×10^{11}) protons, while antiproton bunches contain 50 billion (5.0×10^{10}) antiprotons.

As with the Booster, the Main Ring provides the necessary electric field shift to maintain beam stability through transition; this occurs when the protons and anti-protons have an energy of 17.6 GeV. During the transition, a brief beam instability occurs.

3.1.5 The Tevatron

The Main Ring injects its counter-rotating beams of 150 GeV protons and antiprotons into the Tevatron. The Tevatron, located about two feet below the Main Ring in the same tunnel, accelerates the protons and antiprotons to an energy of 900 GeV.

Increasing the beam energy in the Tevatron, while maintaining the same radius

as the Main Ring, requires a powerful magnetic field to keep the protons and antiprotons in orbit. Superconducting magnets provide this magnetic field: Nearly 1,000 magnets operating at a temperature of 4.6^o Kelvin (-268.4^o C) provide a field of 4.2 Tesla. The conventional magnets in the Main Ring can provide only about 1.8 Tesla (corresponding to a beam energy of 400 GeV).

The Tevatron can hold more than a thousand bunches, but it operates with only six bunches each of protons and antiprotons (more concurrent bunches can lead to instabilities, particularly in the antiproton beam). In two luminous regions (locations 'BØ' and 'DØ' along the ring), special superconducting magnets focus the beam to a height and width of 40 μm each (the height and width in the non-luminous region are 1.3 mm each, or 30 times larger). The proton and antiproton beams cross in the luminous regions and the beam focusing results in a substantial increase in luminosity. In each luminous region, the beams cross at a rate of nearly 300,000 per second, or one every 3.5 μsec.

The data used in this analysis were taken during the 1994-1996 running period of the Tevatron (Runs '1B' and '1C'). Figure 3.3 shows the total integrated luminosity delivered by the Tevatron, as well as that recorded by the DØ detector, during Run 1.

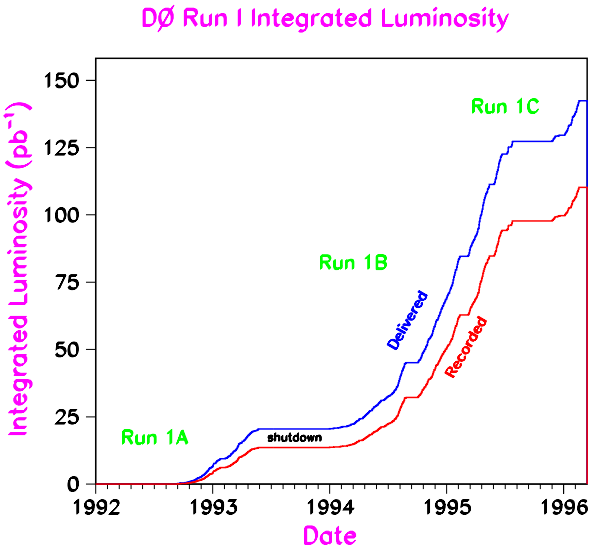

Figure 3.3: *The total luminosity delivered by the Tevatron and recorded by the DØ detector in Run 1 [68].*

3.2 The DØ Detector

The 1.8 TeV $p\bar{p}$ collisions produced by the Tevatron provide the initial state; in general, we search for new physics by studying the different possible final states. We measure the final state particles using one of two detectors: The Collider Detector at Fermilab (CDF) [69]; or the DØ detector [70]. This analysis utilizes the DØ detector to measure the final state particles (Fig. 3.4).

The observation of each final state object consists of two parts: Identification and measurement. Electrons, muons, photons, and hadronic 'jets' comprise the identifiable objects; energy and location constitute the measurable quantities. The DØ detector consists of three subsystems to aid in the identification and measure-

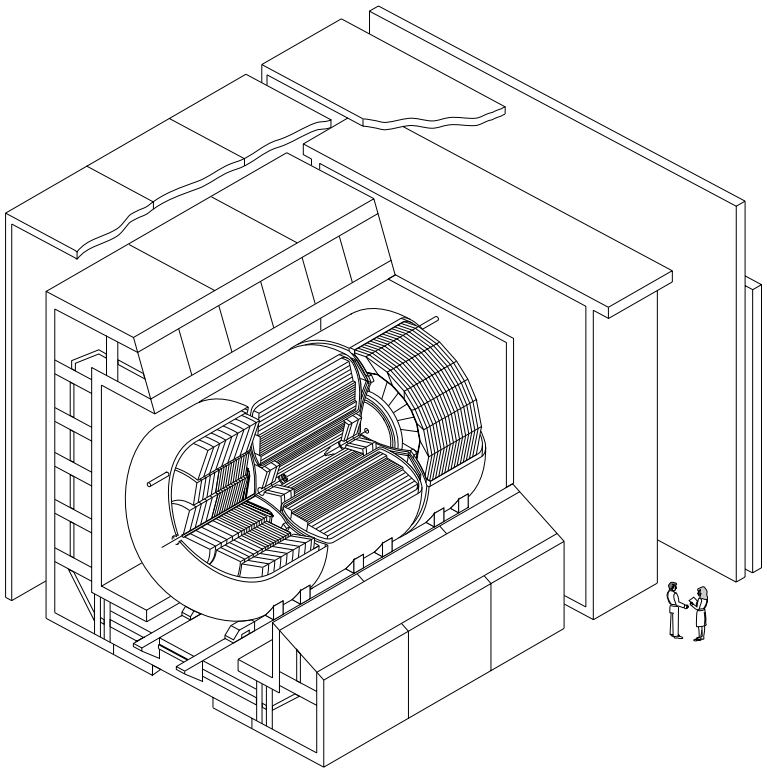

Figure 3.4: *The DØ detector. The Tevatron beam pipe runs through the center of the detector and the Main Ring beam pipe runs through the upper edge of the calorimeter.*

ment of particular objects. The central detector (CD) locates charged particles and distinguishes between electrons, photons and hadrons. The calorimeter provides position and energy measurements, and assists in object identification. The muon system provides muon identification and muon position and energy measurements.

3.2.1 The Central Detector

The final state particles from a given $p\bar{p}$ collision at DØ cross through the beam pipe and enter the central detector system [71], which consists of the vertex drift chamber, the transition radiation detector, and the central and forward drift chambers (Fig. 3.5).

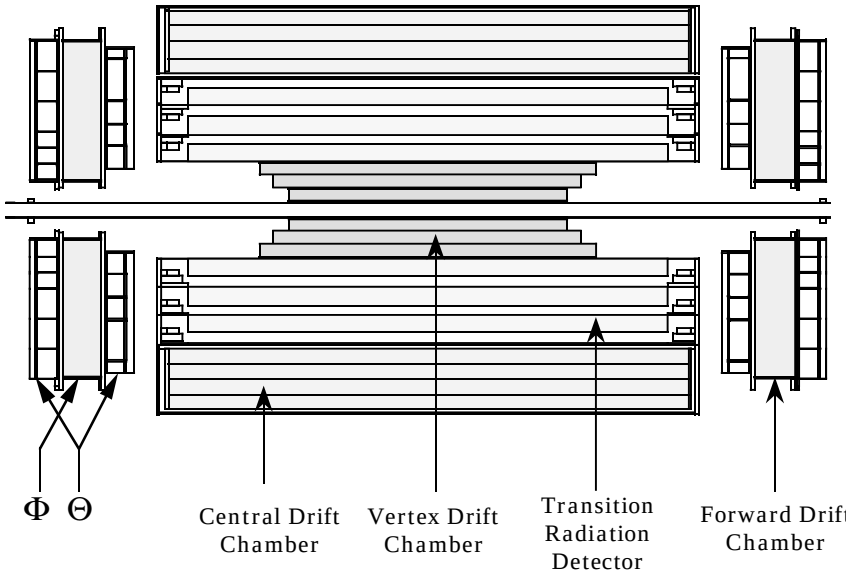

Figure 3.5: *The central detector system. The length of the central drift chamber is 2 meters; its radius is 74.5 centimeters.*

The Vertex Drift Chamber

The vertex drift chamber (VTX) consists of three layers of sense wires, separated by carbon fiber support tubes. Electrically charged particles travelling through the drift chamber strip electrons from the carbon dioxide gas in the chamber. The

negatively charged electrons drift toward a positively charged wire at a nearly constant speed; as they approach the wire, they accelerate, stripping electrons from other carbon dioxide atoms and creating an avalanche of electrons. By the time the electrons reach the wire, they have multiplied by a factor of 40,000, providing a clear electronic signal in the wire.

The first VTX layer encompasses the beryllium beam tube, 3.7 cm from the center of the tube. It contains 16 sets of sense wires, equally spaced around the tube (every 22.5 degrees). Each set contains 8 wires moving out radially from the tube; each successive wire is staggered by 100 μm relative to the previous wire to assist in position measurement. The outer 2 layers have the same configuration as the first layer, with 32 sets of sense wires instead of 16. Table 3.1 lists some of the parameters and performance characteristics of the VTX system.

Active radius	3.7 cm to 16.2 cm
Number of layers	3
Active lengths of each layer	96.6 cm, 106.6 cm, 116.8 cm
Number of cells	16, inner layer; 32, outer 2 layers
Numbre of sense wires	8 per cell; 640 total
Sense wire separation	4.6 mm radially with 100 μm stagger
Drift velocity	$\sim 7.3\mu$m/ns
Maximum drift distance	1.6 cm
Gas gain	4×10^4
Position resolution	$r\phi \sim 60$ μm, $z \sim 1.5$ cm

Table 3.1: *Vertex chamber parameters and performance characteristics [70].*

We determine the position of a charged particle in the VTX by measuring the time difference between the $p\bar{p}$ collision and the arrival of electrons at each wire (the 'drift time'). The time difference provides the distance of the particle from each wire (since the drift speed is known); to determine the position, we use the information from two neighboring staggered wires. If the charged particle comes from the right of the wires, the wire to the right measures a shorter drift time; if it comes from the left, the wire to the left measures a shorter time.

While the VTX fully surrounds the beam tube, it has limited coverage along the direction of the beam (the 'z' direction). The first layer extends 48.3 cm in each direction from the center of the detector, and each subsequent layer extends about 5 cm further. If the interaction occurs in the center of the detector, particles with an angle greater than 15.5^o from the beam line pass through the VTX chamber. Or, defining the detector 'pseudo-rapidity' as,[1]

$$\eta = -ln(tan(\theta/2)), \tag{3.1}$$

particles with $|\eta_d|$ less than 2.0 pass through the VTX.

[1] We henceforth use pseudo-rapidity rather than angular degrees because the pseudo-rapidities of two particles add, while their angles do not (as long as the particles are travelling at speeds close to the speed of light, which is the case for all of the particles we study). We use η_d (detector η) to refer to the pseudo-rapidity of particles emanating from the center of the detector ($z = 0$), and η (physics η) to refer to the pseudo-rapidity of particles originating from the actual vertex in an interaction. Because the measured z position of an interaction ranges from -100 cm to 100 cm, the two definitions are not in general equivalent.

The VTX measures positions perpendicular to the beam line with an accuracy of 60 μm; we can use this accuracy to determine the radial displacement of the interaction from the center of the beam pipe (the 'x' and 'y' positions of the interaction).

The Transition Radiation Detector

After passing through the VTX, particles with $|\eta_d|$ less than 1.4 pass through the transition radiation detector (TRD). The TRD consists of three sets of 393 polypropylene foils interspersed with nitrogen gas. When charged particles pass from the foil to the gas (or vice versa), they radiate energy in the form of photons. At the end of each set of foils a drift chamber measures the photons that have converted into an electron and a positron.

The amount of 'transition' radiation emitted in the TRD depends inversely on the particle's mass: The lighter the particle, the more radiation it will emit. Electrons are the lightest charged particles and will emit the most radiation. Thus, measurement of the radiation emitted by particles in the TRD helps distinguish electrons from charged hadrons.

The Central Drift Chamber

The central drift chamber (CDC) extends 92 cm in each direction ($+z$ and $-z$) from the center of the detector. It has a similar radial design to the VTX: Four layers of drift chambers form a cylinder surrounding the TRD. The layers contain 32 sets of 7 sense wires, extending a radial distance 49.5 cm to 74.5 cm from the center of the beam tube. At this radius, particles with $|\eta_d|$ less than 1.0 pass through all four layers of the CDC.

The CDC provides excellent resolution in the radial direction (180 μm), but the resolution in the z direction (2.9 mm) is not as good. The sense wires are parallel to the beam and do not provide information on where along the wire the electron shower hits. In order to determine the z position of the hit, we use delay lines on both sides (radially) of the sets of 7 sense wires. A shower incident on a sense wire induces a pulse in the delay line; by measuring the time difference of the arrival of the pulse on both ends of the delay line, we can determine the z position of the shower.

The CDC serves three purposes: Reconstruction of the vertex z position; matching of tracks to energy deposits in the calorimeter; and measurement of the energy loss (dE/dx) of particles traversing the detector. We determine the z position of the interaction by pointing the tracks back to the beam line and averaging over the tracks (Section 4.2.1). We then match the tracks to the cal-

orimeter energy deposits, assisting in the identification of photons, electrons and hadronic jets. A photon leaves no tracks (since it has no charge); an electron leaves one track; and a hadronic jet generally leaves more than one track. The dE/dx measurement also assists in the identification of electrons and hadronic jets, since electron energy loss in the detector differs from that of hadrons.

Table 3.2 lists some of the parameters and performance characteristics of the CDC.

Active radius	51.8 cm to 71.9 cm
Number of layers	4
Active length	179.4 cm
Number of cells per layer	32
Numbre of sense wires	7 per cell; 896 total
Sense wire separation	6.0 mm radially with 200 μm stag ger
Drift velocity	$\sim 34\mu$m/ns
Maximum drift distance	7 cm
Gas gain	2-6 $\times$ 10^4
Position resolution	$r\phi \sim 180$ μm, $z \sim 2.9$ mm
Number of delay lines	2 per cell; 256 total
Delay line velocity	2.35 mm/ns

Table 3.2: *Central detector chamber parameters and performance characteristics [70].*

The Forward Drift Chamber

In addition to the CDC, the forward drift chamber (FDC) measures charged tracks for use in determining the z vertex position. The FDC measures tracks for

particles with $|\eta_d|$ between 1.2 and 2.8.

The FDC (Fig. 3.6) consists of two sets of drift chambers, one at each end (in z) of the CDC/TRD/VTX system. In each set, one drift chamber contains wires extending radially from the beam pipe; these wires determine the angular direction around the beam pipe ('ϕ') that charged particles travel. Two chambers on either side of the ϕ chamber form a square around the beam pipe and measure charged particles' angular positions relative to the pipe ('θ').

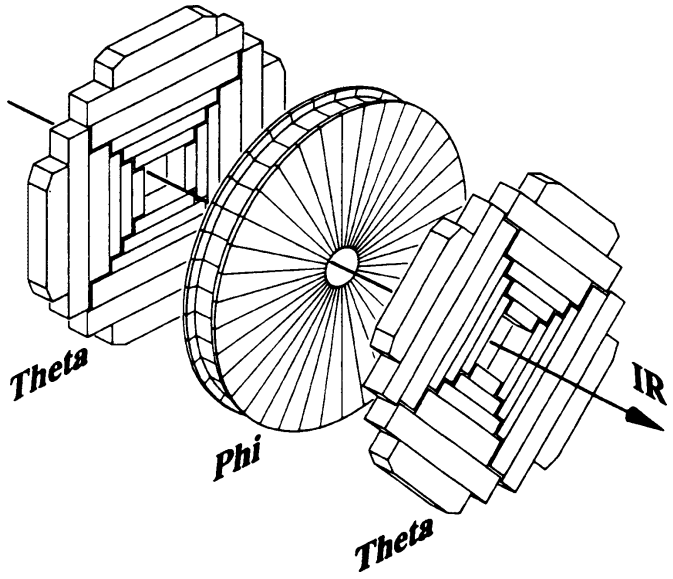

Figure 3.6: *The forward drift chamber θ and ϕ modules.*

3.2.2 The Calorimeter

After travelling through the central detector system, all particles except for muons and neutrinos lose their energy through radiation and collisions in the

calorimeter. The calorimeter measures a fraction of this energy (the 'sampling fraction'), allowing for an inference of each particle's initial energy.

The bulk of the calorimeter uses uranium as the material into which incident particles collide. Electrons colliding with uranium atoms radiate high energy photons, which also interact with the uranium to form electron-positron pairs. The rate of energy loss for electrons and photons is described in terms of the 'radiation length' (X_o), which is the thickness of the collision material required for these particles to lose 63% of their initial energy (i.e., $dE/E = -dx/X_o$). For uranium, the radiation length is 3.1 mm [30], so that the average electron or photon loses 99% of its energy after travelling through 15 mm of uranium. To account for fluctuations in this value, and to ensure containment of all photons and electrons, the DØ calorimeter has (at η_d=0) a uranium thickness of 65.6 mm in the region used for stopping electrons and photons (the 'electromagnetic,' or EM, region).

The process of energy loss for hadrons is more complicated than it is for electrons and photons [72]. Hadrons lose their energy by colliding with uranium nuclei, spraying more hadrons through the uranium. These secondary hadrons can collide with the uranium or (if they are π^0 particles) decay into photon or electron-positron pairs. Since uranium nuclei are considerably smaller than uranium atoms, hadronic collisions with the nuclei occur less frequently than electronic

and photonic collisions with the atoms. Thus, hadrons travel greater distances before losing their energy. The 'interaction length' (λ) for hadrons in uranium is 10.5 cm. At η_d=0, the DØ calorimeter consists of 33.6 cm of uranium in the first hadronic ('Fine Hadronic,' or FH) region, and 46.5 mm of copper (3.2 λ) in the second hadronic ('Coarse Hadronic,' or CH) region. Figure 3.7 shows the DØ calorimeter, with the different regions labelled.

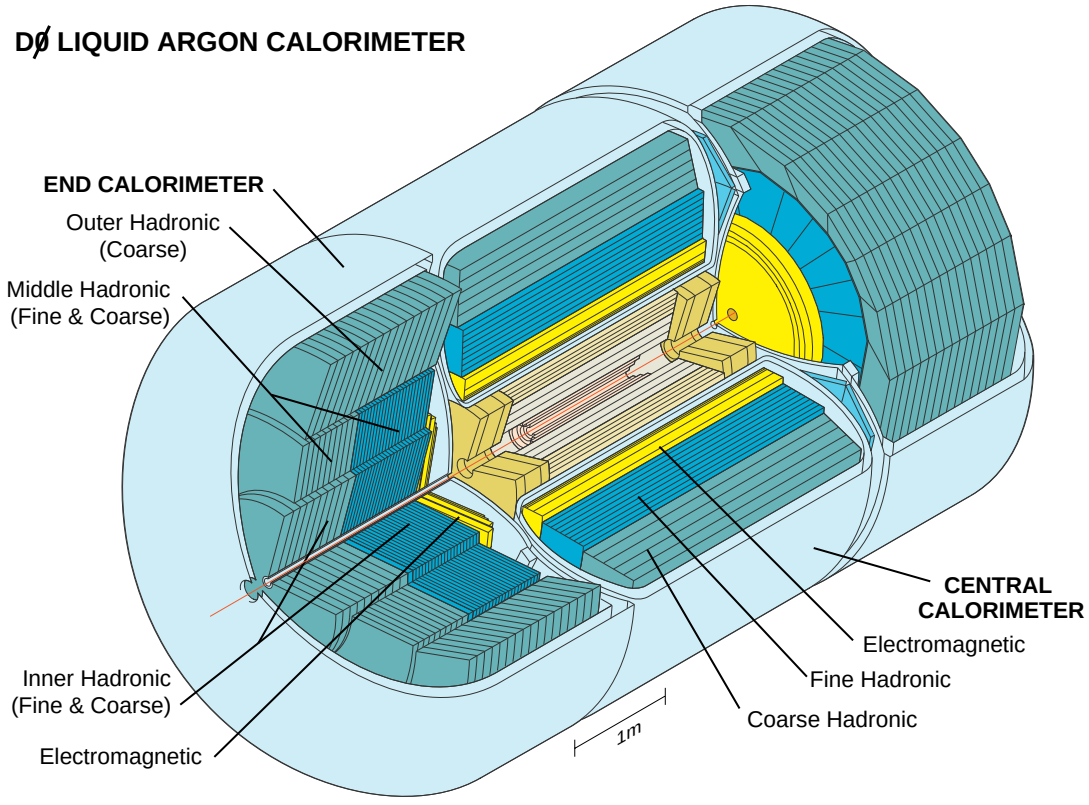

Figure 3.7: *The calorimeter and central detector, with the different region labelled. Not shown is the Main Ring, which runs through the Coarse Hadronic region at the top of the detector.*

Calorimeter Cell

The calorimeter is divided into individual 'cells' to provide information on the development of electromagnetic and hadronic showers through the detector. Each cell has three components (Fig. 3.8): A uranium plate, with which incoming particles collide; a liquid argon gap, which the showering charged particles ionize; and a copper plate surrounded by an insulator (G10), which measures the electric charge produced through ionization. The charge is collected in a duration of 2.2 μsec after the beam crossing. Since the average electron takes 0.45 μsec to traverse the cell, the board collects nearly all of the charge resulting from the initial collision. After the measurement, the charge on the board dissipates, allowing for the measurement of particles from the next beam crossing 1.3 μsec later. Occasionally, a large deposition of charge takes longer than the time between crossings to dissipate, resulting in a larger charge in the cell at the beginning of the next crossing than at the end; in this case, the cell erroneously measures a negative net charge in the subsequent crossing.

Calorimeter Segmentation

The calorimeter cells are stacked into radial 'layers,' which are in turn grouped into detector regions (Tables 3.3 and 3.4). The calorimeter is divided into three liquid argon cryostats, one centered on the interaction point (the 'central calor-

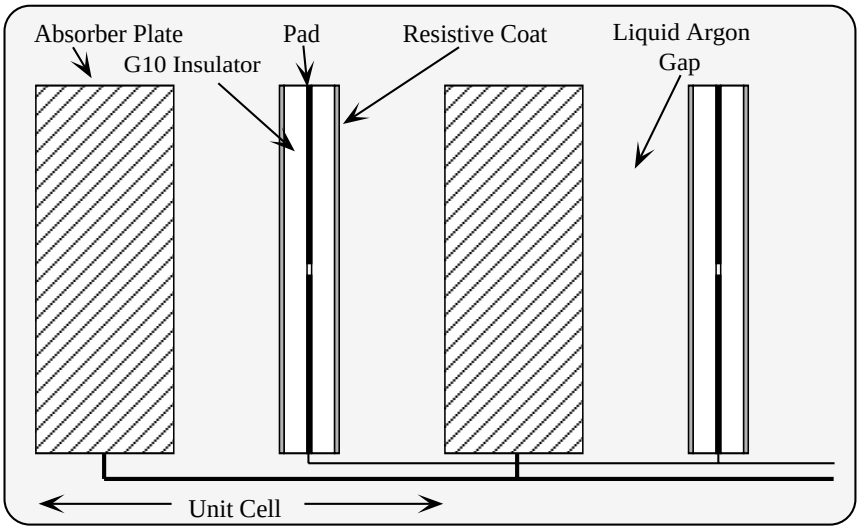

Figure 3.8: *The composition of the unit calorimeter cell. The widths of the absorber plates (3 to 46.5 mm) and liquid Argon gaps (2.1 to 2.3 mm) vary by detector region (Tables 3.3 and 3.4).*

imeter,' or CC [73]), and two on either side of the CC (the 'end calorimeters,' or EC [74]).

The cells are designed to provide 0.1×0.1 η-ϕ 'towers' projecting from the interaction point (Fig. 3.9). The third layer has 0.05×0.05 η-ϕ segmentation to provide better resolution of electromagnetic shower shapes, improving the distinction between electrons or photons and pions. At high $|\eta_d|$ the height and width of 0.1×0.1 regions narrow considerably, so for $|\eta_d|$ >3.2 the segmentation is 0.2×0.2.

The separate cryostats leave small gaps in coverage in the intercryostat region (ICR). In this region, an intercryostat detector (ICD) consisting of scintillator tiles provides energy measurement. In addition, copper pads at the outer edges of the

Characteristic	EM	FH	CH
$\|\eta_d\|$ coverage	≤ 1.2	≤ 1.0	≤ 0.6
Number of layers	4	3	1
Number of cells per layer	2, 2, 7, 10	20, 16, 14	9
Absorbing material	Depleted U (DU)	98.3% DU, 1.7% Nb	Cu
Absorber thickness (mm)	3	6	46.5
Liquid argon gap (mm)	2.3	2.3	2.3
Radiation lengths (X_0)	20.3	96.8	32.9
Interaction lengths (λ)	0.76	3.2	3.2
Sampling fraction (%)	11.79	6.79	1.45

Table 3.3: *The characteristics of the different regions of the central calorimeter (*CC*). The numbers of radiation and interactions lengths decrease with increasing $|\eta_d|$; the values listed are for η_d=0.*

Characteristic	EM	IFH	ICH	MFH	MCH	OH
$\|\eta_d\|$ coverage	1.3-3.7	1.6-4.5	2.0-4.5	1.0-1.7	1.3-1.9	0.7-1.4
# of layers	4	4	1	4	1	3
Cells per layer	2,2,6,8	16	14	15	12	8
Absorber	DU	DU-Nb	SS	DU-Nb	SS	SS
Thickness (mm)	4	6	6	6	46.5	46.5
Argon gap (mm)	2.3	2.1	2.1	2.2	2.2	2.2
# of X_0	23.2	123.9	32.8	116.1	37.9	65.1
# of λ	0.95	4.9	3.6	4.0	4.1	7.0
Sampling (%)	11.9	5.7	1.5	6.7	1.6	1.6

Table 3.4: *The characteristics of the different regions of the end calorimeter (*EC*). In this Table, 'SS' stands for stainless steel, and the numbers of radiation and interaction lengths assume the incident particles are perpendicular to the cells. This approximation is valid in the limit $|\eta_d| \to \infty$; for lower values of $|\eta_d|$, these numbers increase.*

CC and the inner edges of the EC provide additional energy measurement (since these boards have no uranium, they are called 'massless gaps,' or MG).

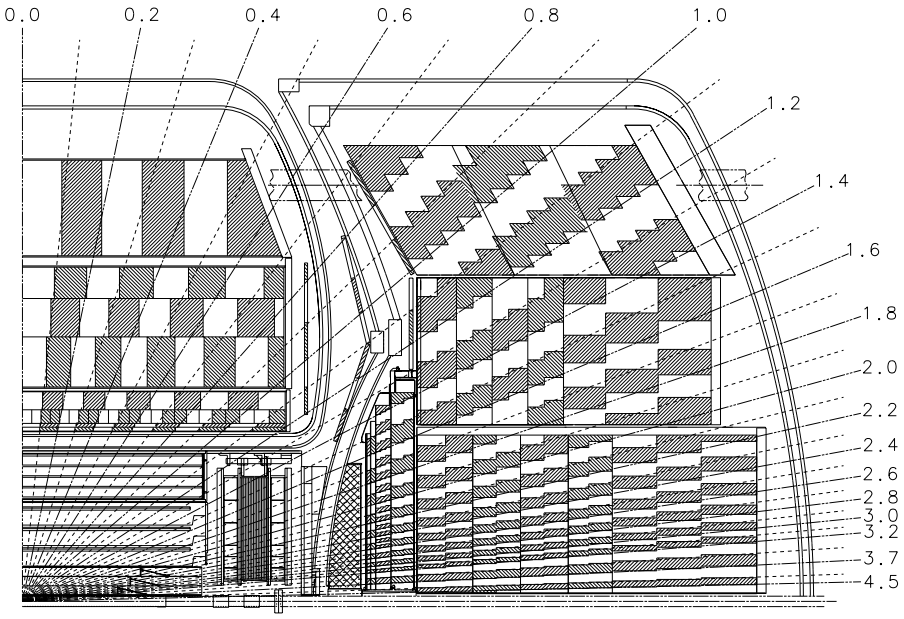

Figure 3.9: *A central detector and calorimeter quadrant. The numbers represent the η_d directions from the center of the detector.*

In the CH region, the detector has a hole for the Main Ring, which runs through one ϕ division for $|\eta_d| < 1.3$. In the CC, there are gaps in the modules every two divisions; these gaps are rotated between the EM, FH, and CH layers, so that they do not significantly affect hadronic showers. However, we lose a small percentage of electrons and photons through these detector cracks.

Calorimeter Performance

The calorimeter energy measurement has errors dominated by: Electronic noise and Uranium decay; statistical fluctuations in the number of measured charged particles; and calorimeter non-uniformities and calibration errors. We combine these errors into the fractional energy resolution of measured particle energies:

$$(\frac{\sigma_E}{E})^2 = \frac{N^2}{E^2} + \frac{S^2}{E} + C^2 \tag{3.2}$$

The calorimeter noise (N) dominates the error for low E_T measurements and calorimeter non-uniformities and calibration errors (C) dominate for high E_T measurements. Table 3.5 shows the different factors contributing to the resolution of individual pions, electrons, and jets. A 50 GeV jet with $|\eta_d| \leq 0.5$ has a resolution of 5.8 GeV.

Measured object	N	S	C
Electron	0.21 GeV	0.16 $\sqrt{GeV}$	1.2%
Pion	1.3 GeV	0.44 $\sqrt{GeV}$	4.7%
Hadronic Jet, $\|\eta_d\| \leq 0.5$	2.7 GeV	0.69 $\sqrt{GeV}$	3.6%

Table 3.5: *The values of noise (N), sampling fluctuations (S), and errors from calorimeter non-uniformities (C) entering into equation 3.2. We show the resolution for* CC *electrons [73] [75],* ECMH *pions [73], and hadronic jets with* $|\eta_d| \leq 0.5$ *[76].*

3.2.3 Level 0

In addition to the calorimeter surrounding the beam, two sets of scintillators ('Level 0' [77]) between each forward detector chamber and end calorimeter measure the forward-scattered particles from the collision. When a proton and antiproton collide, individual quarks or gluons interact and the remaining quarks (the 'beam remnants') continue down the beam pipe. Some of the beam remnants scatter slightly and pass through the Level 0 scintillators, which provide at least partial coverage for $1.9 < |\eta_d| < 4.3$. In over 99% of collisions resulting in proton and antiproton fragmentation ('inelastic collisions'), both sets of Level 0 scintillators observe pieces of the beam remnants.

3.2.4 The Muon System

Unlike hadrons, photons, and electrons, muons do not lose significant energy ($\sim$0.1%) in their collisions with the calorimeter Uranium plates. Thus, muons travel through the calorimeter and enter the muon system [78]. A magnetic field produced by toroids causes the muons to bend as they travel through the system. Neighboring the toroids on the inside and outside are proportional drift tubes (PDTs), which measure the location of a muon before and after it passes through one of the toroids. By reconstructing the muon's path and measuring its curvature in the magnetic field, we determine the energy of the muon.

Figure 3.10 shows a cutaway view of the DØ detector, with the muon components labelled. The muon system consists of 2 pieces: The wide angle muon system (WAMUS), which covers $|\eta_d| \leq 2.5$; and the small angle muon system (SAMUS), which covers $2.5 < |\eta_d| \leq 3.6$. The WAMUS consists of 3 toroids, a central toroid (CF) covering $|\eta_d| \leq 1$, and 2 end toroids (EF) covering $1 < |\eta_d| \leq 2.5$. The 2 SAMUS toroids occupy the center of the EF toroids. The proportional drift tubes come in three layers, A, B, and C, corresponding to immediately inside, immediately outside, and about one meter outside the toroid, respectively. Layer A consists of four PDTs, while layers B and C consist of three PDTs each.

3.2.5 Main Ring Veto Counters

During proton injection or transition in the Main Ring, the beam destabilizes and frequently collides with the beam pipe at DØ, resulting in a spray of particles through the calorimeter. We use a set of Main Ring veto counters [79] to identify this activity, providing important information on whether the calorimeter has been contaminated with energy not induced by the $p\bar{p}$ collision.

The veto counters consist of two sets of scintillators surrounding the Main Ring, one on each end of the calorimeter. Each set contains two hexagonal counters surrounding the beam pipe, with each hexagon divided into six ϕ slices.

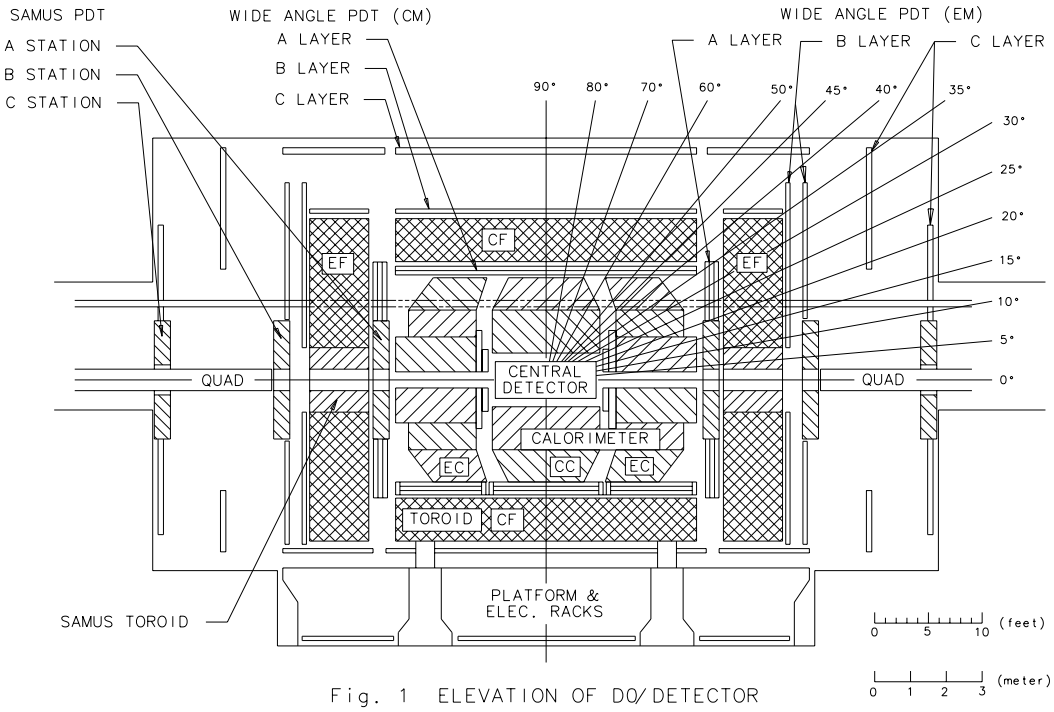

Figure 3.10: *The full DØ detector, with the muon components labelled.*

Chapter 4

Data Collection

We obtain our 2 jets + $\not\!\!E_T$ data set through two steps: Collection and selection. As the $p\bar{p}$ collisions occur, we collect the raw data from each detector subsystem and reconstruct the final state particles, keeping events that loosely satisfy our 2 jets + $\not\!\!E_T$ final state criteria. After the completion of the Run, we remove events in which the measurement has been compromised by cosmic rays, Main Ring activity, detector malfunction or measurement errors.

We collect the data in individual 'runs,' which last up to 4 hours. Run 1B consists of individual runs numbering 72481 to 93115, while the runs in Run 1C number 94478 to 96929. Since the protons and antiprotons collide inelastically in only 63% of the crossings, and since only 0.1% of these collisions produce high E_T jets (> 25 GeV), we do not collect the data from every $p\bar{p}$ crossing. Rather, we

use a 'trigger' system to select events with high E_T particles for data collection. The system consists of 3 stages, or 'Levels,' which separate the data by final state. We use a set of trigger requirements ('JET_2_MISS' [80]) that selects events with a 2 jets + $\not\!\!E_T$ final state.

Following the initial selection of the data by the trigger, we use DØRECO version 12 [81] to consolidate the information from each detector subsystem and reconstruct particle tracks and jets. We use DØFIX version 2.6 [82] for various corrections and CAFIX version 5.1 [83] for jet energy corrections. The resulting data set has full measurements of the final state particles and can be analyzed for the presence of new particles and processes.

4.1 The JET_2_MISS Trigger

We collect the 2 jets + $\not\!\!E_T$ data set by requiring the final state of a given crossing to pass a set of selection criteria known as the JET_2_MISS trigger. We apply these criteria immediately after each crossing, thereby reducing the 10^{13} crossings to a data set of a little over 5×10^5 events.

4.1.1 Level 0

Along with the particles produced by $p\bar{p}$ collisions, the DØ detector measures high energy particles originating from stars and galaxies outside of the Earth's solar system ('cosmic rays'). These cosmic rays can produce an apparent 2 jets + $\not\!\!E_T$ final state through radiation or ionization in the detector. To reduce the number of these events contaminating our data sample, we use the Level 0 trigger [77] to require an inelastic collision consistent with a z vertex within 100 cm of the center of the detector. This requirement removes cosmic ray events and events resulting from interactions between the beam and gas in the beam pipe.

4.1.2 Level 1

The Level 1 trigger system [84] collects the detector information and retains events that satisfy a given set of requirements based on rudimentary jet and missing energy calculations. The Level 1 trigger system also allows for the removal of periods during which the data are likely to be contaminated by large quantities of Main Ring induced energy.

Jets

The Level 1 trigger system utilizes two hadronic jet definitions: Calorimeter tower jets (JT); and large tile jets (LJ). A calorimeter tower jet consists of all EM

and FH layers in a 0.2×0.2 η-ϕ region, while a large tile jet consists of all EM and FH layers in a 0.8×1.6 η-ϕ region. For tower jets, the trigger system sums the EM and FH layers separately, and then adds the two. The trigger selects events based on the nuber of jets whose energies transverse to the beam (E_T) are above a given threshold.

To reduce the effects of noise, the trigger has a 'zero suppression' mechanism: It only adds the EM and FH layers from a given tower if those layers contain energy outside of the range of normal background noise. This range is defined to be $|E_T| < 0.5$ for the sum of FH layers in a tower with $|\eta_d| \leq 0.8$, and $|E_T| < 0.25$ for the sum of FH layers in a tower with $|\eta_d| > 0.8$. For the sum of EM layers in a given tower, the noise range is defined to be $|E_T| < 0.25$.

The JET_2_MISS trigger utilizes the calorimeter tower jet definition, requiring 3 tower jets to have values of E_T greater than 5 GeV. Since hadronic jets have a cone radius of about 0.5, high E_T jets frequently contain more than one Level 1 tower jet with E_T above 5 GeV (Section 5.1.1). Thus, the requirement of 3 tower jets reduces the size of the data set while maintaining events with two high E_T jets.

$\not\!\!E_T$

Since the initial collision has zero energy in the direction transverse to the beam, the net measured energy in this direction results from unmeasured particles or energy measurement errors. We define the magnitude of this energy as the 'missing transverse energy' ($\not\!\!E_T$). We define the direction of $\not\!\!E_T$ to be opposite to the direction of the net measured E_T.

The Level 1 trigger system calculates the missing energy of each event by adding the zero suppressed energy in every EM and FH layer with $|\eta| \leq 2.4$. It then calculates the $\not\!\!E_T$ using the Level 0 vertex measurement. The JET_2_MISS trigger requires the Level 1 $\not\!\!E_T$ measurement to be greater than 20 GeV.

Main Ring Vetoes

The 'Main Ring vetoes' constitute the final pieces of the Level 1 trigger system incorporated into the JET_2_MISS. Figure 4.1 shows an example of an event with Main Ring activity resulting in large energy depositions in the calorimeter. Such activity occurs most frequently from instabilities in the Main Ring beam during injection and transition. Thus, the JET_2_MISS trigger does not take data during the 0.4 second window starting from Main Ring injection and continuing through Main Ring transition. This veto, known as MRBS_LOSS[1], results in a loss of 17%

[1]MRBS stands for Main Ring Beam Sync.

of the 2.4 second Main Ring cycle. In addition to the instabilities during injection and transition, Main Ring activity can result from collisions with gas in the beam pipe. The JET_2_MISS trigger does not take data when Main Ring protons or antiprotons pass through the DØ detector within 800 nanoseconds of a Tevatron $p\bar{p}$ crossing. This veto, known as MICRO_BLANK, results in an additional 9% loss of luminosity.

The Level 1 JET_2_MISS trigger requirements have an effective cross section of about 0.6 μb; thus, only one out of every 10^5 events passing the Level 0 trigger passes the Level 1 requirements.

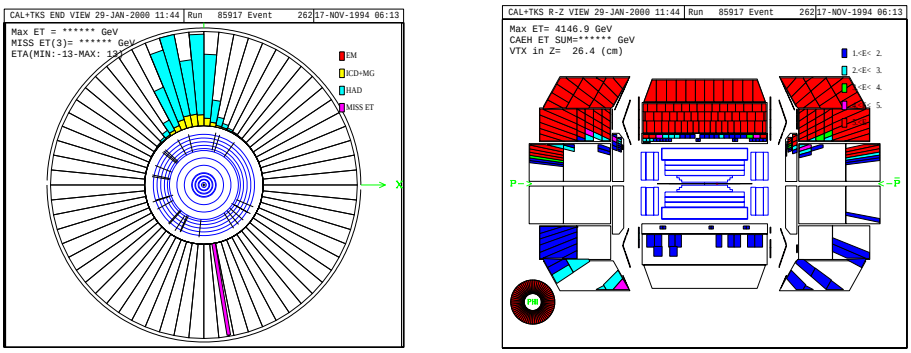

Figure 4.1: *End (left) and side (right) views of the calorimeter in an event with Main Ring activity. There are 55 TeV of E_T in the Main Ring region.*

4.1.3 Level 2

The Level 2 system consists of 50 VAX computer processors that reconstruct the particles in each event in more detail and with greater accuracy than the Level

1 system. The JET_2_MISS trigger utilizes the Level 2 reconstruction of jets, $\not\!\!E_T$, and the angle in ϕ between the direction of the $\not\!\!E_T$ and the direction of the nearest jet.

Jets

The Level 2 processors construct jets using Level 1 jet 'seeds,' defined to be tower jets with E_T greater than 2 GeV and large tile jets with E_T greater than 6 GeV. Starting with the highest energy seed, the Level 2 system sums the E_T of all trigger towers whose centers lie within a 0.7 η-ϕ cone of the seed tower. If the seed jet is a large tile jet, we define the seed tower as the E_T weighted center of the large tile. We weight the towers within the jet by E_T to determine the η and ϕ positions of the jet.

The JET_2_MISS trigger requires 2 Level 2 jets, 1 with an E_T above 25 GeV, and another with an E_T above 10 GeV.[2]

$\not\!\!E_T$

We calculate the $\not\!\!E_T$ at Level 2 using the energy of each individual cell. Each cell possesses its own zero suppression value: We measure the standard deviation (σ) of the noise in each cell during periods of Tevatron quiescence; during a Tevatron

[2]A small fraction (3.8%) of the data taken with the JET_2_MISS trigger requires two Level 2 jets with E_T greater than 30 GeV.

Run we set all cell measurements within 2σ of zero to zero (Fig. 4.2). As an example, a typical hadronic cell is set to zero if it contains energy within about 0.1 GeV of zero.

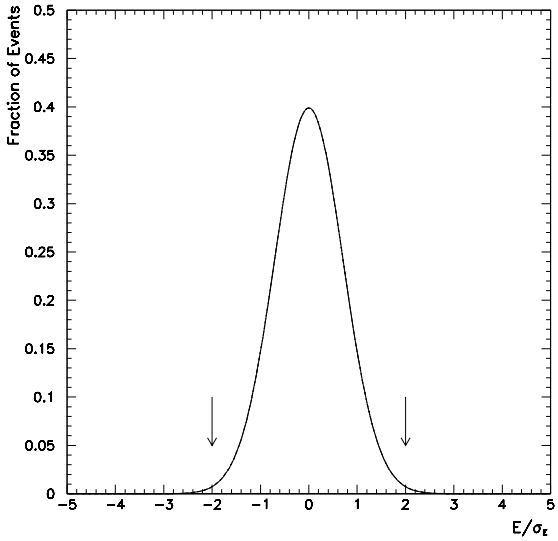

Figure 4.2: *A representation of the noise in each cell when no charged particles pass through the cell. If the measured energy in a cell is within 2σ of 0 (the arrows in the plot), we set the cell's energy to zero.*

The JET_2_MISS trigger requires the Level 2 $\not\!\!E_T$ to be greater than 25 GeV. In addition, the trigger requires that the angle in ϕ between $\not\!\!E_T$ and the nearest jet be greater than 0.25 radians (or $2\frac{1}{2}$ detector ϕ slices). This requirement removes events with a jet with significant energy loss through detector cracks (such as the regions between cryostats).

The accuracy of the $\not\!\!E_T$ measurement is crucially dependent on a functioning detector and the absence of energy deposits from external sources. Any anomalous

energy measurement from an electronics failure or Uranium decay leads to an erroneous $\not\!\!E_T$ measurement. We use the 'Anomalous Isolated Deposit Algorithm' (AIDA) to remove individual cells with anomalous energy measurements ('hot cells') [85]. AIDA removes any cell with an E_T greater than 10 GeV and an energy at least 20 times greater than the average energy of the cells in the neighboring layers. If a neighboring layer is the third EM layer (EM3), which has smaller cells than other layers, AIDA sums the energies of the 4 EM3 cells corresponding to the one candidate cell. If the hot cell is in the FH1 layer, which typically has the largest energy depositions of a jet, AIDA requires the E_T of the cell to be greater than 30 GeV for removal.

We show the full set of JET_2_MISS trigger requirements in Table 4.1. The Level 2 requirements reduce the effective cross section by a factor of about 100, resulting in an overall reduction factor of 10^7 for Levels 1 and 2 combined.

Quantity	Level 1	Level 2
Jet/Tower E_T	3 towers $>$ 5 GeV	25 GeV jet 10 GeV jet
$\not\!\!E_T$	20 GeV	25 GeV
$\Delta\phi$(jet,$\not\!\!E_T$)	-	14.3^o

Table 4.1: *The* JET_2_MISS *Levels 1 and 2 trigger thresholds. The Level 2 requirements listed here are implemented for 96.2% of the data; for the other 3.8%, the trigger has two 30 GeV jet thresholds and no* $\Delta\phi$ *requirement.*

4.2 Event Reconstruction

After collecting the data with the JET_2_MISS trigger, we reconstruct the final state particles and measure their positions and energies. The reconstruction program (DØRECO 12) performs a multitude of tasks for each event, among which are: The definition of the positions of all collisions; the determination of the likelihood of multiple collisions; the construction of jets from clusters of cells containing energy depositions; the calculation of electron identification quantities based on information from the various subdetectors; and the construction of muon tracks and calculation of muon energies.

4.2.1 Vertex Measurement

The calculation of the transverse energies of the final state particles requires the measurement of the z position of the interaction point. While the x and y positions vary by no more than 0.5 cm throughout the Run (Fig. 4.3), the variation in the z position is 200 cm (Fig. 4.4). The x and y positions are calculated periodically during the Run to constrain the reconstruction of particle tracks.

To perform the vertex reconstruction [81], we find all of the tracks in the CDC and extrapolate them to the z axis. We then bunch the tracks into clusters of at least three tracks. If the CDC contains 1 or 2 tracks, we define the event to contain a single cluster. If the CDC contains no tracks, we use the FDC tracks to

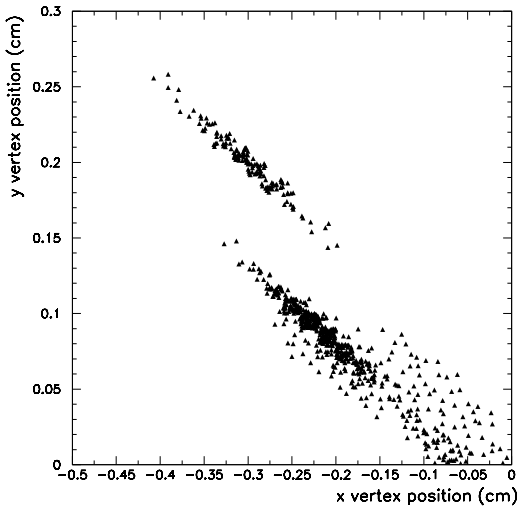

Figure 4.3: *The x and y positions of the events in the* JET_2_MISS *data set.*

determine the vertex. We fit each cluster to a Gaussian distribution and determine the cluster position from the distribution's mean. If the positions of 2 clusters are separated by more than 8 cm, we assign 2 collision vertices to the event and define the primary vertex as the mean of the cluster with the most tracks.

The Tevatron produces an average of one inelastic collision per $p\bar{p}$ crossing at DØ (Section 4.6). The JET_2_MISS trigger selects only one event out of 10^7; on average, this event contains an additional inelastic collision. Most inelastic collisions result in small quantities of energy entering the detector: Only about 0.1% of a sample of inelastic collisions (Section 5.2.1) contains a jet with E_T greater than 25 GeV. We do not remove events with more than 2 jets (Chapter 5), so the energy from additional collisions does not significantly affect our data

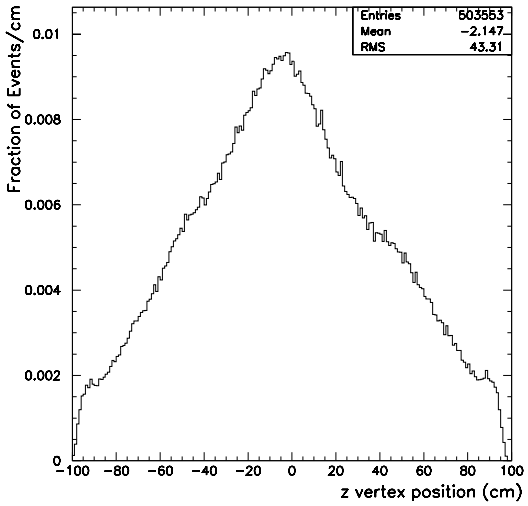

Figure 4.4: *The z positions of the events in the* JET_2_MISS *data set.*

set. However, the 'secondary' vertex from the additional collision adversely affects our $\not\!\!E_T$ measurement in a small fraction of events. When we erroneously define the vertex from the secondary collision to be the vertex for the primary collision, our jet E_T and $\not\!\!E_T$ measurements are incorrect (Section 5.2.3).

4.2.2 Multiple Interactions

We use the Level 0 and CDC information to define a 'multiple interaction' (MI) variable [81]. The variable provides an estimate of the likelihood that an event contains more than one collision. It has the following 5 values:

1. 'most likely' a single interaction

2. 'likely' a single interaction

3. 'likely' a multiple interaction

4. 'most likely' a multiple interaction

5. 'likely three' or more interactions

The quantities we use as inputs to this variable are: The number of reconstructed vertices; the time difference between particles arriving at the two Level 0 scintillators; the distance between the reconstructed vertex and the Level 0 vertex; the fraction of tracks used to construct the primary vertex; the fraction of tracks used to construct the secondary vertex, in the case of 2 vertices; and the total energy in the calorimeter. As an example, for the case of 1 reconstructed vertex and a time difference of less than 0.4 ns between particle arrival at the two Level 0 scintillators, we set the multiple interaction variable to 1.

4.2.3 Jet Reconstruction

Hadrons colliding with Uranium nuclei produce broad showers of particles. We measure these showers using a cone with a 0.5 radius in η-ϕ space ($R = \sqrt{(\eta^2 + \phi^2)}$). On average, 91.2% of the initial quark or gluon energy is enclosed by the 0.5 cone [83].

Electron and photon collisions with Uranium atoms produce radiation in a narrow region. We measure this energy using a 0.3×0.3 η-ϕ neighborhood of

towers.

The Jet Cone Algorithm

The cone algorithm [86] starts with the highest E_T calorimeter tower, which must be at least 1 GeV. It adds adjacent towers if they contain E_T greater than 1 GeV and continues to add adjacent towers until the towers are a distance R=0.3 from the original tower, or until there are no more adjacent towers with E_T greater than 1 GeV. We define this group of towers as a 'precluster,' and we determine its position by averaging over the E_T weighted η and ϕ centers of its towers. We repeat this procedure with the highest E_T tower ($>$ 1 GeV) not contained in the first precluster, and continue until we no longer have any towers with E_T greater than 1 GeV.

After defining the set of preclusters, we form jet clusters by taking the energy in a 0.5 cone around each precluster and recalculating the E_T weighted η and ϕ position of the cluster; given this new axis, we again take the energy in a 0.5 cone and determine a new η and ϕ position. We continue until the jet axis stabilizes or until we have repeated the process fifty times. The stabilized axis provides the jet η and ϕ positions and the E_T in the 0.5 cone provides the jet E_T; if the E_T is below 8 GeV, we do not include the jet for analysis.

If the axes of 2 jets are separated by less than R=1.0, the jets share at least 1

calorimeter tower. If the total E_T of all shared towers is more than half the E_T of the lower E_T jet, the jets are merged into a single jet. Otherwise, the E_T of each shared cell is added to the closest jet and not to the furthest jet.

The Electromagnetic Nearest Neighbor Algorithm

The electromagnetic clustering algorithm utilizes only the EM layers in each tower. The algorithm associates every tower with the highest E_T tower within a 0.3×0.3 $\eta - \phi$ neighborhood, as long as the highest E_T tower contains more than 50 MeV in the EM layers. If a cluster contains more than 1.5 GeV of energy in the EM layers and has at least 90% of its E_T in these layers, we keep the cluster for analysis as a potential electron or photon.

4.2.4 Electron Identification

The reconstruction programs collect the information from the CDC, FDC, TRD, and calorimeter to calculate the likelihood that a given electromagnetic cluster is an electron.

Electrons traversing the CDC or FDC have two identifiable characteristics: A single isolated track; and a distinct rate of energy loss (dE/dx). Hadrons generally produce several tracks and a photon produces none (unless it converts into an electron-positron pair, in which case it produces two). Electrons and

photons differ from hadrons in their TRD radiation, calorimater shower shapes, and fraction of energy deposited in the EM region. We combine this information into a likelihood that a given particle is an electron:

$$L_{5\ variable} = -log(P_{track\ \sigma} \times P_{dE/dx} \times P_{TRD\ energy} \times P_{EM\ fraction} \times P_{\chi^2}) \quad (4.1)$$

In this equation, P_x denotes the probability that a cluster with a given value of x is an electron, and χ^2 parametrizes the cluster's shower shape. Small values of L correspond to a high probability that the cluster is an electron. For clusters with $|\eta_d| \leq 1.1$, we use the CDC for track and dE/dx information. For clusters wtih $|\eta_d| > 1.5$, we use the FDC for this information, and we do not use the TRD. For clusters with $|eta_d| > 2.6$, we lose reolution for the shower shape χ^2 because the cells in the third EM layers increase in size from 0.05×0.05 to 0.1×0.1 in $\eta - \phi$ space.

In addition to the log likelihood, we use the cluster's 'isolation fraction' to identify electrons. Electrons produce small showers in the calorimeter, while hadrons produce broader showers. Most of an electron's energy is contained in a 0.2 cone, while a large fraction of a hadron's energy falls outside this cone. We define

the isolation fraction as:

$$f_{iso} = \frac{E(all\ layers, R < 0.4) - E(EM\ layers, R < 0.2)}{E(EM\ layers, R < 0.2)}, \tag{4.2}$$

or the fraction of energy in a 0.4 cone that is not contained in the core EM 0.2 cone.

4.2.5 Muon Reconstruction

A muon travelling through the muon system produces charged tracks in the proportional drift tubes and bends when passing through the toroid. The bend direction is perpendicular to both the muon's direction of travel and the direction of the magnetic field. As an example, for the special case of a muon travelling in the y direction at η=0, the magnetic field is in the -x direction and the bend is entirely in the -z direction. In general, the muon bends in a combination of the x, y, and z directions determined by the muon's η and ϕ position.

We reconstruct muon tracks using the photodrift tubes in the A, B, and C layers, separately reconstructing tracks in the bend and non-bend directions. To assist in the identification of muons, we define 'flags' to provide information on the quality of the muon track reconstruction. The 'flag word 1' contains information on the number of layers used in the reconstruction. The 'flag word 4' is defined

as the number of failures of the following quality criteria:

- The A, B, and C layers all register hits along the muon's track.
- The distance between the muon vertex and the reconstructed vertex is less than 100 cm in the non-bend direction.
- The distance between the muon vertex and the reconstructed vertex is less than 80 cm in the bend direction.
- The root mean square deviation of the individual hits to the track is no more than 7 cm in the non-bend direction.
- The root mean square deviation of the individual hits to the track is no more than 1 cm in the bend direction.

After reconstructing the tracks in the muon system, we examine the calorimeter cells along the muon's path for energy depositions. We examine a 5x5 $\eta - \phi$ array along the path and find the longest contiguous path with cells above the zero suppression threshold. We measure the fraction of hadronic layers containing such cells ('HFRAC'), as well as the fraction of energy in the last calorimeter layer before the muon system ('EFRAC'; this quantity uses a 3x3 $\eta - \phi$ array).

4.3 Cryostat Correction

After reconstruction, DØFIX 2.6 applies various corrections to each event. Among these are a correction to the reconstructed track positions due to the CDC's finite length, and an energy correction to adjust for differences between the cryostats. The jet energy calibration program (CAFIX, Section 4.5) assumes the cryostat correction has *not* been applied, so we remove this correction after running DØFIX.

DØFIX corrects the energy of each cryostat cell as follows:

- $E^{FIX} = E^{RECO} \times 1.0496$, CC
- $E^{FIX} = E^{RECO} \times 1.0478$, ECS
- $E^{FIX} = E^{RECO} \times 1.0609$, ECN

We remove these corrections by adjusting each jet's energy, as well as its x, y, z, and transverse components. Since jet energy corrections affect the $\not\!\!E_T$, we also adjust the $\not\!\!E_x$ and $\not\!\!E_y$ for the jet adjustments. These adjustments are:

- $E = E^{FIX}/1.0496$, jet $|\eta_d| \leq 1.1$
- $E = E^{FIX}/1.0478$, jet $\eta_d > 1.1$
- $E = E^{FIX}/1.0609$, jet $\eta_d < -1.1$

- $\not\!\!E_i = \not\!\!E_i^{FIX} + E_i^{FIX} - E_i$

In the last equation, i corresponds to the x and y components, E_i^{FIX} corresponds to the sum of the jet energies after DØFIX, and E_i corresponds to the sum of the jet energies after adjustments.

4.4 Jet Energy Calibration

After reconstructing electromagnetic and hadronic jets, we calibrate their energies and measure their energy resolutions. In any detector, we can write a particle's true energy (E_{true}) as a function of the measured jet energy ($E_{measured}$); studies have shown that in the DØ calorimeter, the following function applies over the full range of energies used in this analysis:

$$E_{true} = \alpha E_{measured} + \beta \tag{4.3}$$

Thus, our energy calibration involves only the measurement of α (the 'scale') and β (the 'offset'). The contributions to the offset come from energy within the jet which did not originate from the initial high energy particle. Such contributions include: Energy deposits from uranium decay; additional inelastic collisions; proton or antiproton remnants from the high energy collision; or residual charge in the readout electronics system from previous collisions. The scale corrects for

inaccuracies in the energy calibration prior to the Run (the 'response' correction) and for hadronic jet energy that falls outside of the cone used to define the jet (the 'showering' correction).

We use the $Z \rightarrow ee$, $J/\Psi \rightarrow ee$, and $\pi^0 \rightarrow \gamma\gamma$ data to measure the electromagnetic offset, and the Z sample to determine the scale. These particles have masses measured to a high degree of precision, which we reconstruct using the measurements of the energies of the two electrons or photons in the x, y, and z directions.

To measure the hadronic offset, we use data taken every thousandth beam crossing ('zero bias data') and data taken every hundredth inelastic collision ('minimum bias data'). The minimum bias data provides an estimate of the contribution of proton and antiproton remnants from an inelastic collision, while the zero bias data provides an estimate of the other contributions to the hadronic offset. We measure the hadronic scale using events with a photon and a jet; since the photon energy resolution is much better than that of a jet, we use photons to set the hadronic jet energy scale.

4.4.1 $\not\!\!E_T$ Measurement

To measure the $\not\!\!E_T$ in an event, we sum the x and y components of the energy in all of the calorimeter cells, and define the missing energy to be the amount

of energy required to make the net energy in these directions equal to zero. We adjust the missing energy for the corrections to the jets in the event.

4.5 Luminosity

In order to predict the number of events arising from Standard Model processes in our data, we need to measure the total luminosity of our data set. We do this using the Level 0 scintillators, which measure the rate of inelastic collisions produced by the Tevatron. Using the effective Level 0 cross section (σ_{L0}) of 43.1 $\pm$ 1.9 mb [87], we calculate the luminosity per second ('instantaneous luminosity') from the following equation:

$$\frac{dL}{dt} = \frac{Rate\ of\ collisions}{Level\ 0\ cross\ section \times acceptance} \tag{4.4}$$

The acceptance includes the geometrical coverage of the scintillators as well as their counting efficiency. To obtain the luminosity of a given run, we integrate the instantaneous luminosity over the duration of the run.

Since we directly measure the *counting* rate of the Level 0 scintillators (not the actual collision rate), we need to write the equation in terms of the counting rate, taking into account the possibility of multiple collisions per crossing (and thus per

count). We start with the average number of interactions per beam crossing ($\bar{n}$),

$$\bar{n} = \frac{dL}{dt} \times (time\ between\ crossings) \times (inelastic\ cross\ section), \tag{4.5}$$

and use the probability (P_n) that n interactions occur in one crossing:

$$P_n = \frac{\bar{n}^n}{n!} e^{-\bar{n}}. \tag{4.6}$$

We define the counting rate (R) as the probability that at least one interaction occurs in a crossing divided by the time between crossings (τ):

$$R = \frac{1 - P_0}{\tau} = \frac{1 - e^{-\bar{n}}}{\tau} \tag{4.7}$$

Using the equation for the average number of interactions per crossings, we obtain an expression for the instantaneous luminosity in terms of measurable quantities:

$$\frac{dL}{dt} = \frac{-ln(1 - \tau R)}{\tau \sigma_{L0}} \tag{4.8}$$

The instantaneous luminosity of our data set ranges from 0.1 $\times 10^{-6}$ pb^{-1}/sec to 21.3 $\times 10^{-6}$ pb^{-1}/sec, with an integrated luminosity of 92.9 $\pm$ 4.0 pb^{-1}. We show the events in the Run 1B JET_2_MISS data set as a function of instantaneous

luminosity in Fig. 4.5.

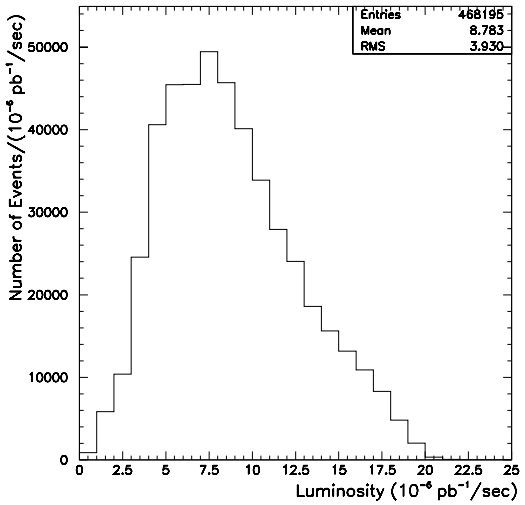

Figure 4.5: *The instantaneous luminosity distribution for the Run 1B* JET_2_MISS *data set. The units of* 10^{-6} pb^{-1}/sec *are equal to* 10^{30} cm^{-2} sec^{-1}.

Chapter 5

Data Selection

Starting with the JET_2_MISS data set, we select events consistent with a high energy collision resulting in 2 hadronic jets and unmeasured particles. To accomplish this, we impose minimum thresholds on the E_T of 2 jets and the $\not\!\!E_T$, and we remove events where $\not\!\!E_T$ results from factors other than unmeasured particles.

Measurement fluctuations are in general larger in the trigger than after full reconstruction of the events. Due to these fluctuations, events with values above the trigger thresholds after reconstruction may not have values above the thresholds in the trigger. This inefficiency decreases as the reconstructed values increase, and it goes to zero when the values become much larger than the trigger thresholds. To reduce the effects of these thresholds on our data set, we set the reconstructed

jet E_T, $\Delta\phi$(jet, $\not\!\!E_T$), and $\not\!\!E_T$ thresholds to values where the trigger is at least 90% efficient.

In addition to imposing trigger induced thresholds, we remove events with significant quantities of $\not\!\!E_T$ arising from the following factors: Detector or beam problems; large energies in the Main Ring region; incorrect definition of the primary vertex; cosmic ray or electron contamination; muon contamination; and jet energy measurement errors.

5.1 Trigger Induced Thresholds

We measure the efficiencies of the trigger thresholds on jet E_T, $\not\!\!E_T$, and the angle between any jet and $\not\!\!E_T$. We use these efficiencies to define a set of thresholds for these quantities. When predicting the background (Chapter 6), we apply the $\not\!\!E_T$ efficiency and the jet E_T efficiency as a function of the separation between the jets.

5.1.1 Jet E_T Thresholds

We measure the Levels 1 and 2 jet trigger efficiencies using jets with a range of reconstructed energies. Our jets sample consists of data taken JET_MIN, JET_30, JET_50, and JET_85 triggers (Table 5.1). Triggers with a large tile Level 1 require-

ment do not necessarily contain Level 1 tower information, so we require events taken with these triggers to also pass the Level 1 trigger JET_2_MED.

Trigger	Level 0	Level 1	Level 2
JET_2_MED	-	2 (5 GeV JT)	-
JET_MIN	-	3 GeV JT	20 GeV JT
JET_30	Single interaction	15 GeV LJ	30 GeV JT
JET_50	Single interaction	15 GeV LJ	50 GeV JT
JET_85	-	35 GeV LJ	85 GeV JT

Table 5.1: *Trigger requirements for jet data samples.*

We require 1 jet to pass the Levels 1 and 2 trigger requirements and study the rest of the jets in the event. We separate the jets into 3 detector regions: Central ($|\eta_d| \leq 1.0$); intercryostat ($1.0 < |\eta_d| \leq 1.5$); and forward ($1.5 < |\eta_d| \leq 4.0$). Figure 5.1 shows the probabilities that central (CC), intercryostat (IC) and forward (EC) jets of given energies contain a given number of Level 1 towers with E_T above 5 GeV.

We use these results to calculate the probability that 2 jets of a given E_T contain at least 3 Level 1 towers with E_T above 5 GeV. Figure 5.2 shows the efficiency for the case of 2 central jets with equal E_T. We require the E_T of both jets to be at least 50 GeV (the arrow in the Figure) to ensure a high trigger efficiency.

The information available for these studies does not include the zero suppression at Level 1 [88], resulting in a potential systematic error in these measurements.

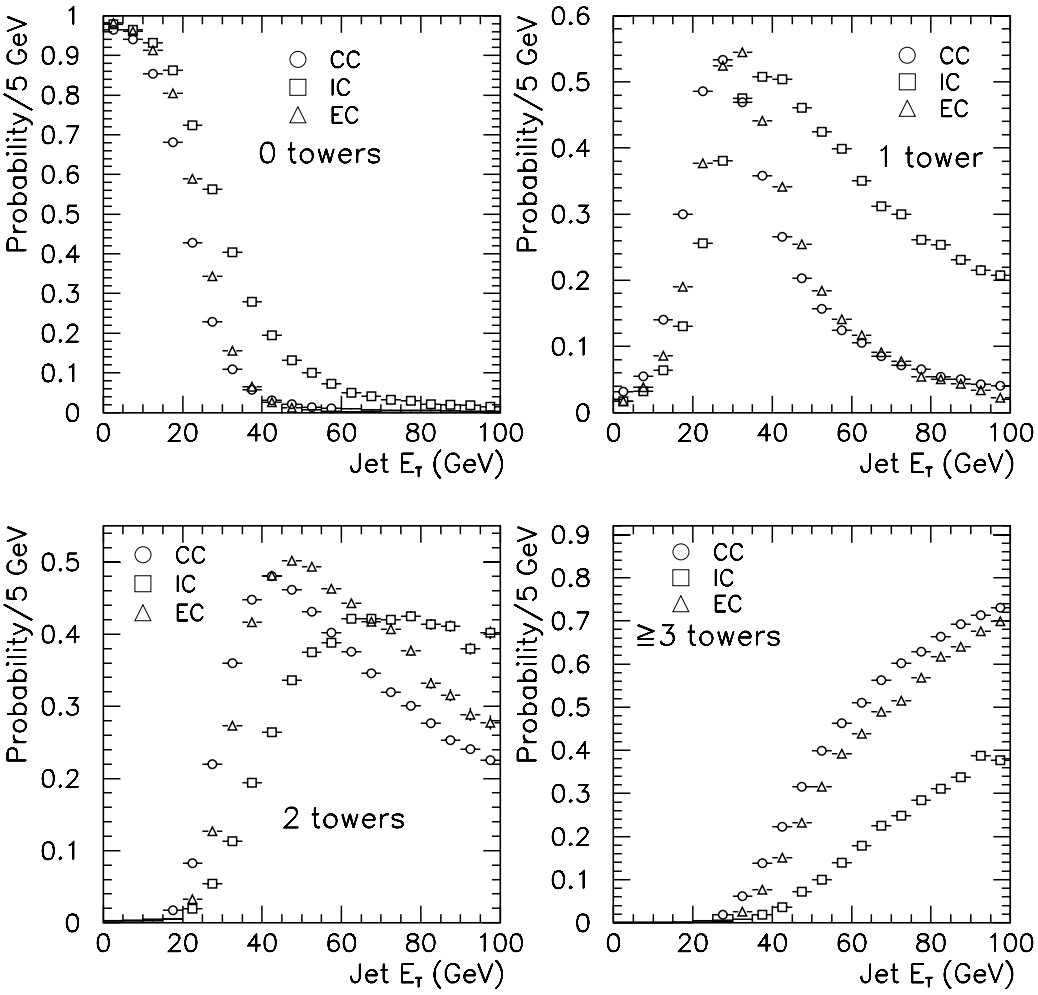

Figure 5.1: *The probability that a jet contains a given number of Level 1 towers above 5 GeV.*

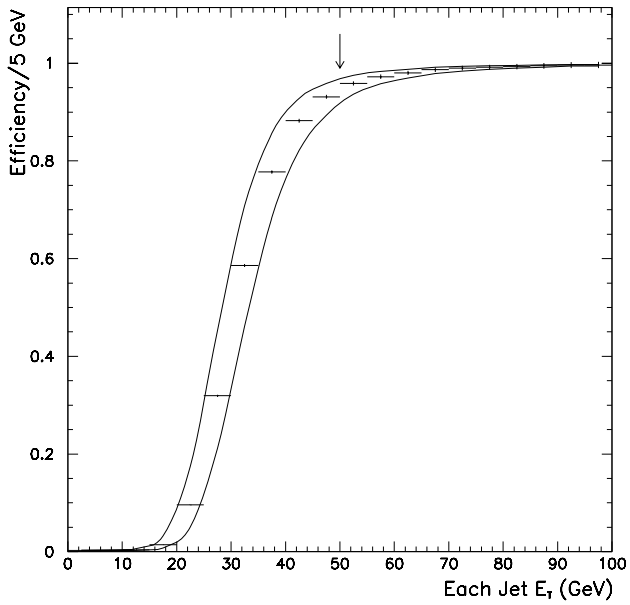

Figure 5.2: *The efficiency for 2 central jets of a given E_T to contain at least 3 Level 1 towers above 5 GeV. The systematic errors are shown as bands.*

We show the maximal effect of this systematic in Fig. 5.2; the error is less than 5% for jets with transverse energies greater than our cut.

For the Level 2 efficiencies, we use events from the JET_MIN data sample that contain at least 3 Level 1 towers above 5 GeV. In each event, we require 1 jet to pass the JET_MIN thresholds and we use the other jets to calculate the efficiency of each Level 2 E_T threshold (10, 25, and 30 GeV) as a function of jet E_T for the 3 detector regions (Fig. 5.3). Requiring both jets to have $E_T \geq 50$ GeV results in a high trigger efficiency at Level 2.

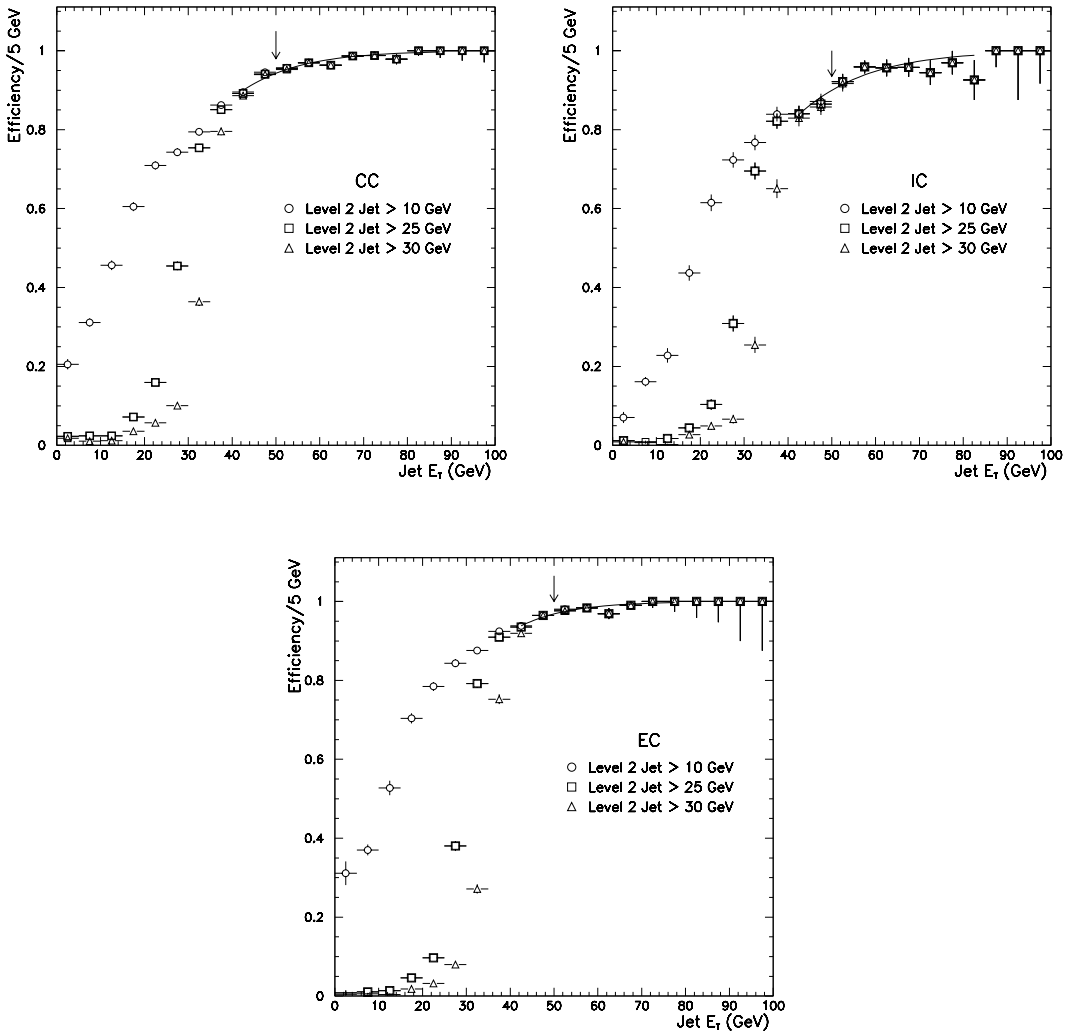

Figure 5.3: *Jet efficiencies for Level 2 trigger requirements for the* CC, IC *and* EC *(clockwise from top left).*

5.1.2 Jet Separation

In measuring the jet E_T trigger efficiencies (Section 5.1.1), we assume that there are no correlations between the jets. This assumption is not valid when there is a small separation in η-ϕ space (ΔR) between the jets. In this case, the energy from one of the jets can spill into the other jet's cone. Also, since the Level 2 trigger builds 0.7 cone jets and we study jets with a 0.5 cone, we expect a loss in efficiency for small jet separation.

We measure the efficiency for 2 jets of given separation to pass the JET_2_MISS trigger using the jets sample of Section 5.1.1. We separate the pairs of jets into 3 distinct topologies: 2 central jets; 1 central jet and 1 intercryostat jet; and 1 central jet and 1 forward jet (we require all events to have at least 1 central jet; see Section 5.2.4). We further separate each sample into events with Jet 2 $E_T >$ 70 GeV and 70 GeV $\geq$ Jet 2 $E_T >$ 50 GeV. The efficiency measurements have a systematic error due to the dependence of the efficiencies on the E_T of the leading jet. We estimate this error by separating each sample into 2 E_T ranges for the highest E_T jet. Figure 5.4 shows the efficiency of each topology and Jet 2 E_T range, including systematic errors.

We reduce the effect of the jet separation trigger efficiency by requiring ΔR > 1.5 when we search for leptoquarks. However, since a high percentage of WZ events have small ΔR (Section 7.2), we do not impose any requirement on ΔR in

our search for WZ production.

5.1.3 $\not\!\!E_T$ Threshold

We use a computer simulation of the $\not\!\!E_T$ trigger thresholds (TRIGSIM [81]) to measure their efficiencies. We provide the simulator with a 2 jets + $\not\!\!E_T$ final state using events with 3 jets and replacing 1 jet with calorimeter noise from a different region of the detector. For our 3 jets event sample, we use data taken with the JET_3_MON trigger, which required JET_2_MED at Level 1 and 3 jets above 10 GeV at Level 2. We require all events to pass the JET_2_MISS jet trigger thresholds. Figure 5.5 shows the efficiency for a given value of $\not\!\!E_T$, with an arrow marking our chosen requirement of $\not\!\!E_T > 40$ GeV.

As a cross-check to the validity of the trigger simulator, we study the trigger efficiency for events with undetected neutrinos. We use events containing an electron and a neutrino from the decay of a W boson. To simulate the effect of 2 final state jets, we require at least 1 hadronic jet in the event, in addition to the electron (see Section 6.1.2 for details of electron and jet quality requirements). Figure 5.6 shows the efficiency of Levels 1 and 2 $\not\!\!E_T$ thresholds of 10 GeV and 15 GeV, respectively. For values of $\not\!\!E_T$ at least 10 GeV greater than the Level 2 threshold, the trigger reaches full efficiency. This result is consistent with the trigger simulator study.

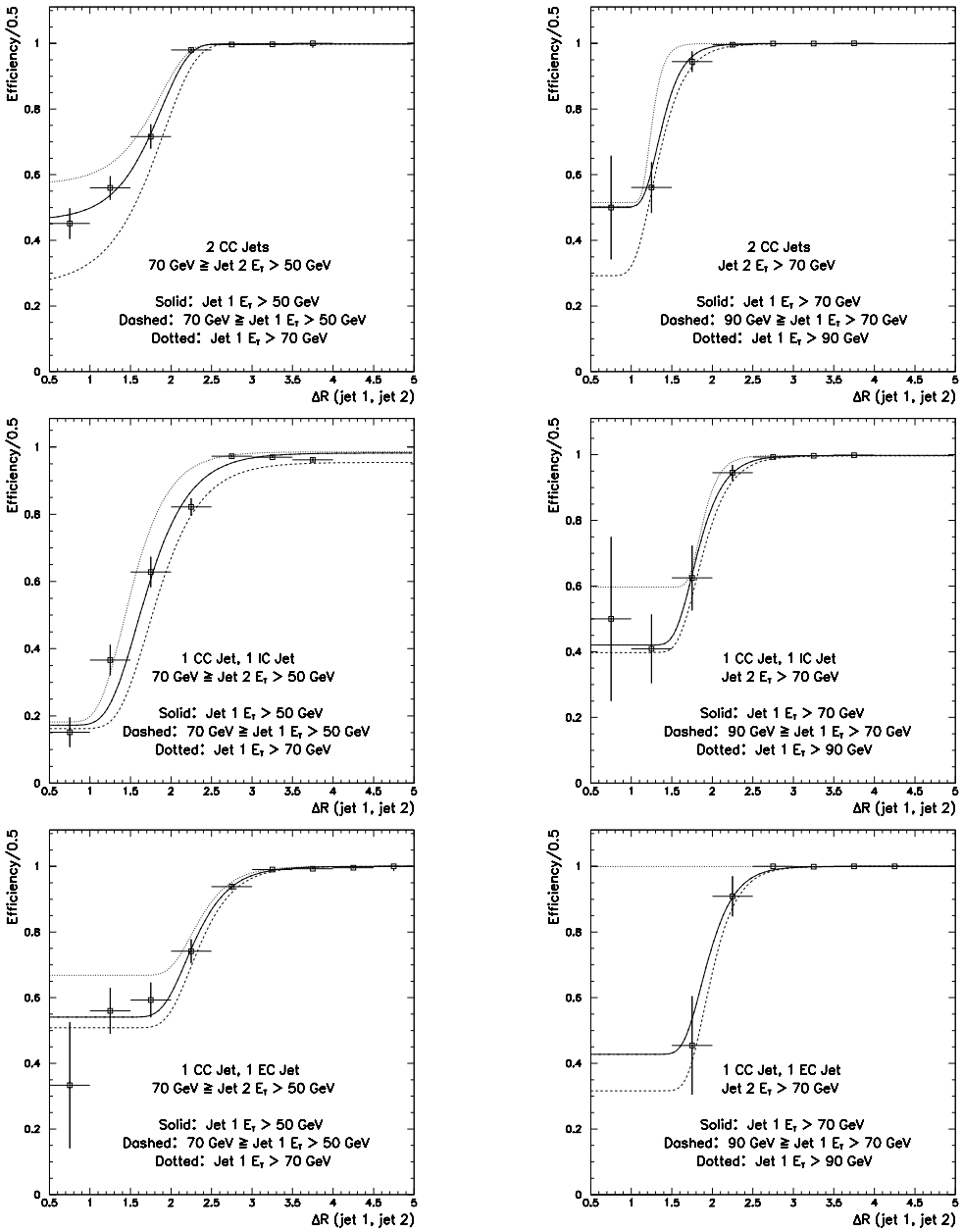

Figure 5.4: *The efficiency for events with 2 jets to pass the* JET_2_MISS *jet requirements, plotted as a function of the ΔR separation between the jets.* Top: *Events with 2 central jets and 70 GeV $\geq$ Jet 2 $E_T > 50$ GeV (left) or Jet 2 $E_T > 70$ GeV (right).* Middle: *Events with 1 central jet and 1 intercryostat jet and 70 GeV $\geq$ Jet 2 $E_T > 50$ GeV (left) or Jet 2 $E_T > 70$ GeV (right).* Bottom: *Events with 1 central jet and 1 forward jet and 70 GeV $\geq$ Jet 2 $E_T > 50$ GeV (left) or Jet 2 $E_T > 70$ GeV (right).*

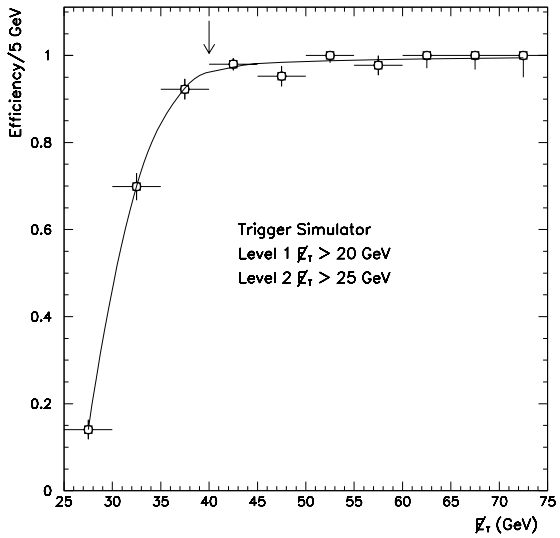

Figure 5.5: *The efficiency of the $\not\!\!E_T$ thresholds in the* JET_2_MISS trigger.

5.1.4 Acolinearity Threshold

The dominant contribution to the 2 jets + $\not\!\!E_T$ data sample comes from inelastic collisions resulting in 2 high E_T jets, with jet energy measurement errors creating artificial $\not\!\!E_T$. Fortunately, in such events the jet directions define the direction of the $\not\!\!E_T$ (Fig. 5.7).

Since events with 2 jets and energy measurement errors have $\not\!\!E_T$ in the same direction as a jet, we implement an acolinearity threshold between any jet and $\not\!\!E_T$ in the JET_2_MISS trigger. To measure the efficiency of this threshold, we use the JET_2_MISS_MON trigger, which has the same jet and $\not\!\!E_T$ thresholds as the JET_2_MISS trigger. We plot the efficiency as a function of the angle (in ϕ) between $\not\!\!E_T$ and the closest jet in Fig. 5.8. We choose a cut of 30^o (marked by an

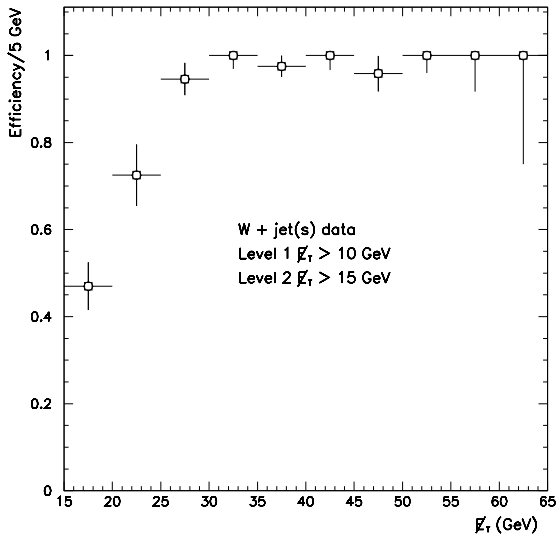

Figure 5.6: *The efficiency of the $\not\!\!E_T$ trigger thresholds in W plus jet(s) data.*

arrow in the Figure), for which the trigger is fully efficient.

5.2 Event Selection

After imposing jet E_T, $\not\!\!E_T$, and $\Delta\phi$(jet, $\not\!\!E_T$) cuts based on the trigger thresholds, we remove events in which measurement error, Main Ring energy, or cosmic rays significantly affect our $\not\!\!E_T$ measurement. In addition, we remove events containing muons or electrons.

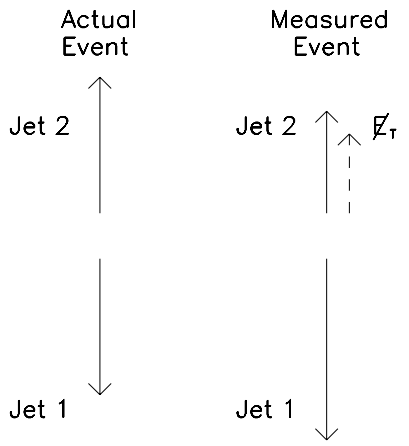

Figure 5.7: *The dominant contribution to the 2 jets + $\not\!\!E_T$ final state at the trigger level arises from 2 jets events (left), where the trigger errs in the E_T measurement of at least 1 jet (right).*

5.2.1 Apparatus Malfunction

We remove all runs with beam, tracking, calorimeter, ICD, or muon system malfunctions. We identify these runs using the Run 1 log book and a standard bad run list. In addition, we infer calorimeter electronics malfunctions through the identification of runs containing a recurrance of jets either in a particular region of the detector, or with their energies dominated by a single cell.

A failure in the calorimeter electronics system can cause a continuous energy measurement in the corresponding set of cells. This results in the continuous reconstruction of a jet in a particular region of the detector. We identify these jets with data that requires only a Level 0 measurement consistent with an inelastic

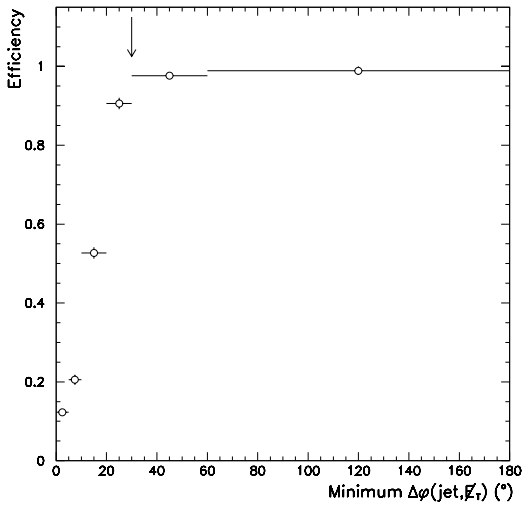

Figure 5.8: *The efficiency of the acolinearity trigger threshold.*

collision ('minimum bias' data). Using the jet η versus ϕ distribution of this data, we examine the run numbers of the clusters of events in a particular detector region. We study the events in the recurring runs and remove the runs that contain identifiable malfunctions. Figure 5.10 shows 2 events from a run removed with this method, one a low energy inelastic event and the other a 2 jets + $\not\!\!E_T$ event.

Another characteristic of a 'jet' resulting from a calorimeter malfunction is the dominance of the jet's energy by a single cell. We identify jets whose highest energy cell contains more than 20 times the energy of any other cell in the jet (we choose this value for consistency with the Anomalous Isolated Deposit Algorithm). If a single run has 5 or more such jets, we remove the run; we use both minimum

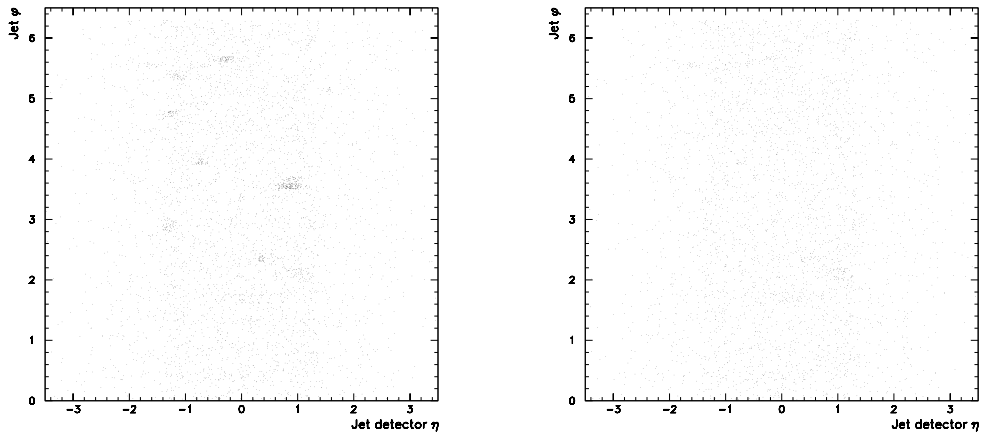

Figure 5.9: *The jet η versus ϕ distribution from inelastic collisions before (left) and after (right) the removal of bad runs.*

bias events and 2 jets + $\not\!\!E_T$ events for this study.

The removal of all bad runs results in a 7.5 pb^{-1} loss in luminosity, leaving 85.4 $\pm$ 3.7 pb^{-1} of data.

5.2.2 AIDA Event Removal

DØRECO applies the Anomalous Isolated Deposit Algorithm (Section 4.1.3) to each event. While the algorithm effectively removes anomalous energy deposits from Uranium decay and electronics failures, it also erroneously removes energy deposits from a small fraction of high E_T jets. This removal results in significant jet measurement error and large erroneously measured $\not\!\!E_T$. We eliminate this effect by removing all events with hot cells removed by AIDA.

The removal of events with hot cells results in an efficiency loss for Standard

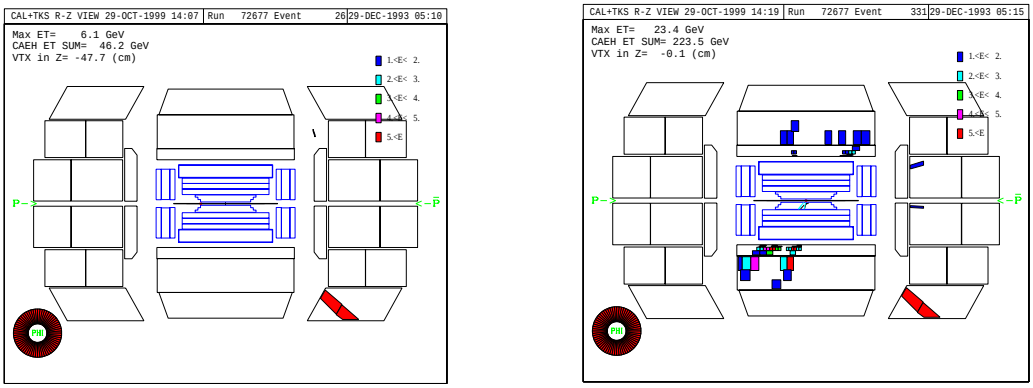

Figure 5.10: *Left: A minimum bias event with malfunctioning calorimeter cells. Right: A* JET_2_MISS *event taken from the same run.*

Model and new physics processes with the 2 jets + $\not\!\!E_T$ final state. Specifically, each jet has a given probability (dependent on the jet's E_T and $|\eta_d|$) that AIDA removes a cell from the jet. This probability has been measured [89] and the results are shown in Fig. 5.11.

5.2.3 Main Ring Beam Instability

Despite the application of the Main Ring vetoes at Level 1, the JET_2_MISS data set contains events with significant Main Ring activity. In fact, the event shown in Fig. 4.1 comes from the JET_2_MISS data set. In addition to such events containing large positive E_T, our data contains events with large 'negative' E_T in this region (Fig. 5.12). Such 'negative' energies occur in events following a large deposition of energy in the Main Ring region. The large energy produces

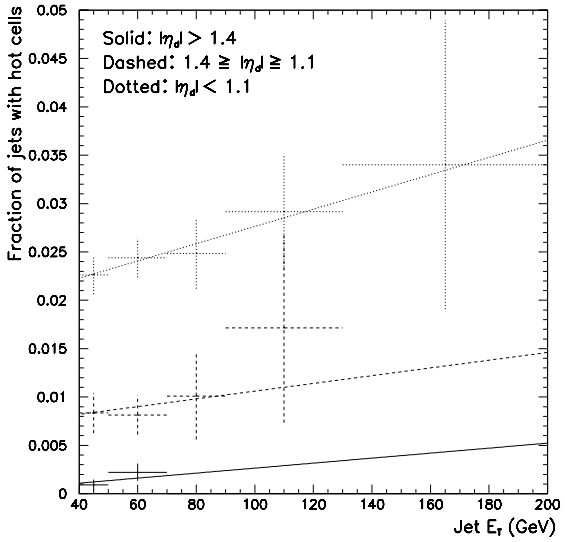

Figure 5.11: *The fraction of jets with hot cells as a function of jet E_T and $|\eta_d|$.*

substantial charge in the calorimeter and it can take the multiple beam crossings for the calorimeter electronics system to release the charge. During this time, the system reads less charge at the end of a given event than at the beginning of the event, resulting in a 'negative' energy measurement.

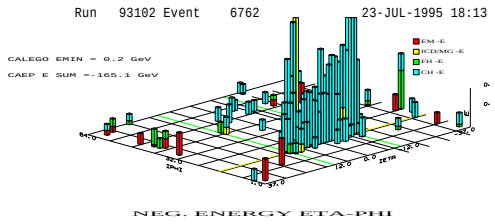

Figure 5.12: *Negative energy plot of an event following a large deposition of energy in the Main Ring region. There are -67 GeV of E_T in the Main Ring region.*

To remove events with such Main Ring effects, we measure the E_T in the Main

Ring region, where this region is defined as cells in the CH layer with $|\eta_d| \leq 1.4$ and $1.6 \leq \phi \leq 2.0$. Figure 5.13 shows the positive and negative energy in this region compared to the energy in a similar ('control') region rotated 180^o in ϕ. We remove events with enough energy along the Main Ring to significantly degrade the $\not\!\!E_T$ resolution; since 50 GeV jets have an energy resolution of just under 6 GeV, the presence of 10 GeV E_T of Main Ring induced energy can provide degradation on the same order as the resolution of the jets. We mark our requirement of |Main Ring E_T| < 10 GeV with an arrow in Fig. 5.13.

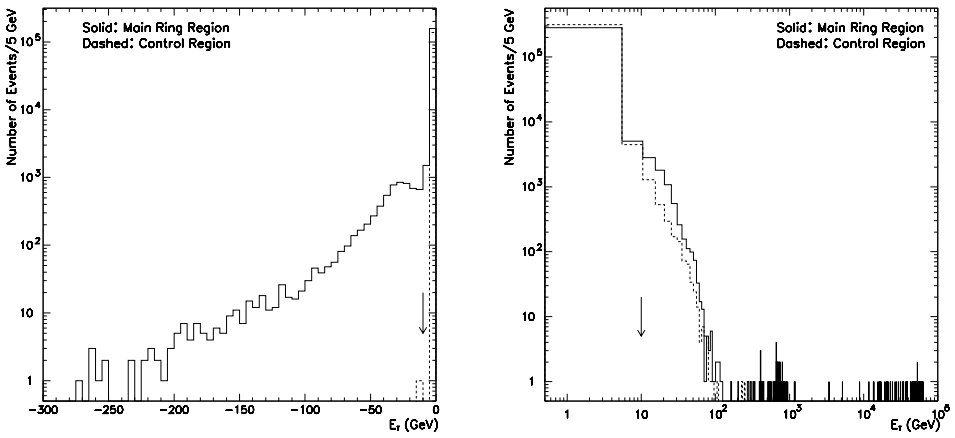

Figure 5.13: *Comparison of Main Ring E_T (solid) to normal Coarse Hadronic E_T (dashed) in the* JET_2_MISS *data sample. The left plot shows negative E_T, the right plot positive E_T. The control region has no events with E_T > 200 GeV or E_T < -15 GeV.*

The Main Ring E_T cut results in an acceptance loss for jets in this region and an overall loss of luminosity. We calculate the former using 50 GeV jets in the control region, and the latter using unbiased data taken every hundredth beam

crossing. The acceptance is (94.0 ± 1.0)% for jets in the Main Ring region; the luminosity loss is (0.24 ± 0.17)%, leaving (85.2 ± 3.7) pb^{-1} of data.

5.2.4 Vertex Measurement Error

In events with 2 or more inelastic collisions, we mistakenly associate the vertex from a low energy collision with that of a high energy collision when more tracks emanate from the vertex of the low energy collision. When we construct a jet with the incorrect vertex, we use the incorrect cone for the jet and fail to measure the energy that falls outside our cone and inside the true cone. The transverse energy measurement depends on the location of the vertex, and the jet energy corrections compound E_T measurement errors. Thus, vertex measurement error can result in significant jet E_T and $\not\!\!E_T$ measurement errors.

To reduce the effects of vertex measurement error, we use central ($|\eta_d| \leq 1.0$) jets to confirm the location of the vertex. We require at least 1 of the 2 highest E_T jets to be central and calculate its 'jet vertex' by averaging the z positions of the CDC tracks within a 0.5 cone of the jet. Since particles from a secondary vertex can pass through the jet's cone, the cone may include tracks that are not part of the jet. To correct for this, we remove the track with the largest deviation from the jet vertex, if that deviation is at least 10 cm ($\sim 5\sigma$). We recalculate the jet vertex and again remove the track with the largest deviation, until no tracks

deviate by more than 10 cm from the jet vertex.

We require the distance between each jet vertex and the reconstructed vertex to be less than 15 cm, choosing this value to maximize the statistical significance of any new physics in our data set (Section 7.3.2). We measure the efficiency of this requirement using multijet events, and the result of $(90.9 \pm 0.5)\%$ is consistent with the value obtained using W plus 2 jets events. Figure 5.14 shows the distance between the jet vertex and the reconstructed vertex for jets data and for the JET_2_MISS data set.

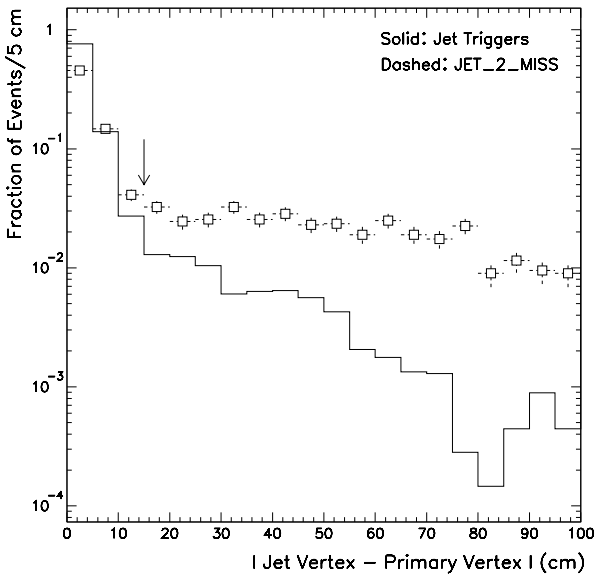

Figure 5.14: *The distance between the jet vertex and the reconstructed vertex for jet (solid) and* JET_2_MISS *(dashed) data.*

Since vertex measurement errors preferentially occur in events with multiple collisions, our data set contains an unusually large fraction of these events. Figure

5.15 compares the value of the multiple interaction variable (Section 4.2.2) for the JET_2_MISS data set and an unbiased single electron data set, both before and after our vertex confirmation requirement. The Figure demonstrates the prevalence of multiple interaction events in our data set and the effectiveness of the vertex requirement. The requirement does not completely remove the bias toward events with multiple collisions, and events with vertex measurement errors comprise a fraction of our QCD background. We will later optimize for the rejection of this background (Chapter 7), further reducing the effects of vertex measurement errors.

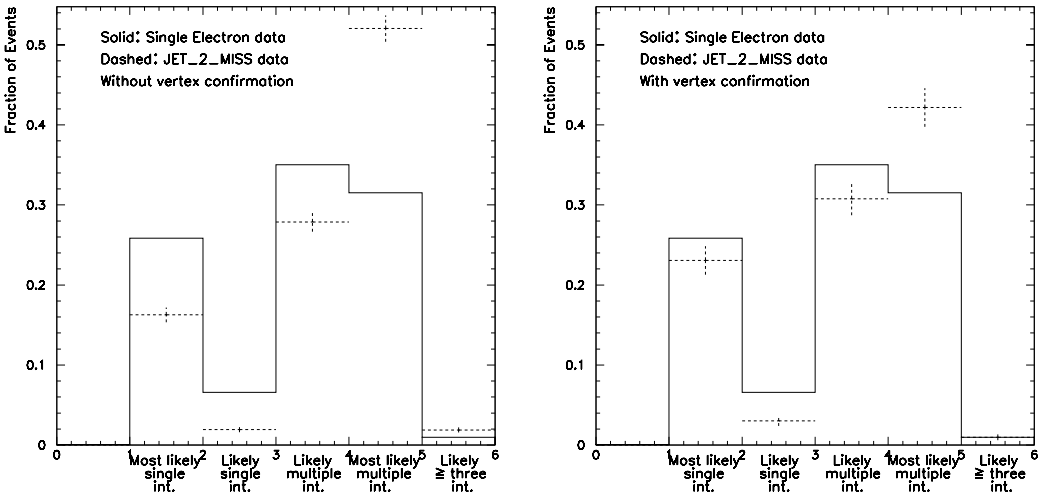

Figure 5.15: *Comparison of the multiple interaction variable for single electron (solid) and* JET_2_MISS *(dashed) data, without (left) and with (right) the vertex confirmation requirement.*

5.2.5 Cosmic Ray and Electron Contamination

A supernova explosion produces high energy particles, consisting predominantly of protons and 'alphas' (helium nuclei composed of two protons and two neutrons). These particles travel through the universe and a small fraction bombards the Earth, interacting with the atmosphere and producing a cascade of secondary particles. Most of the cascading particles radiate their energy before they reach the Earth's surface, but the muon is an important exception. The muon's large mass (compared to an electron) and weak interactions (compared to a hadron) allows it to reach the surface with most of its initial energy. High energy muons ('cosmic rays') passing through our detector can radiate photons, which we reconstruct as jets. When an event contains 2 such photons, it results in a 2 jets + $\not\!\!E_T$ final state.

We identify the presence of photons in our detector by studying the distance the measured particles travel. Photons radiate their energy over a distance of just a few cells (Section 3.2.2), and are typically confined to either the Electromagnetic or Hadronic region of the detector. We study the fraction of energy in the Electromagnetic region ('EM fraction') for jets in our JET_2_MISS data sample and for hadronic jets; since the ICD has no EM layers, we do not include jets in this region. Figure 5.16 shows the maximum and minimum EM fraction of all of the jets in each event. We remove all events containing a jet with EM fraction > 0.95 or $\leq$

0.1. In addition to cosmic rays, this requirement removes events with electrons and other energy depositions inconsistent with the production of a hadronic jet.

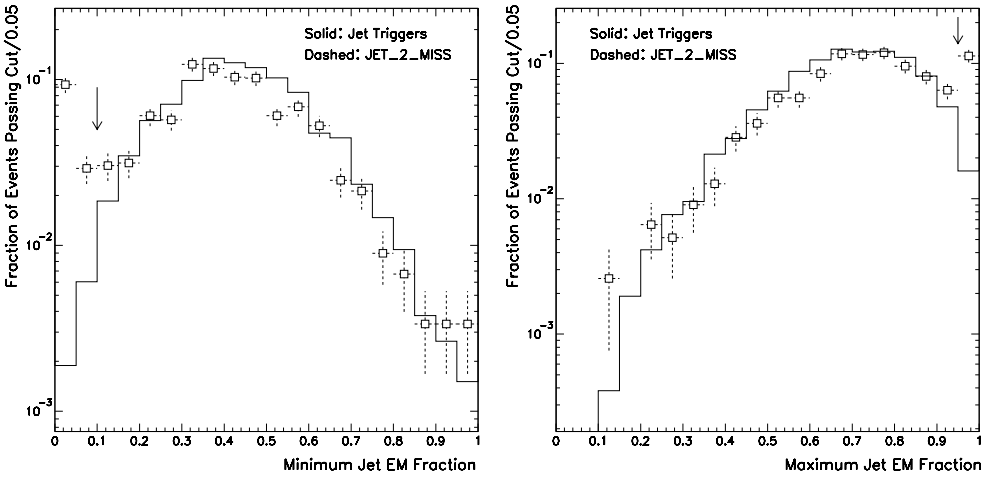

Figure 5.16: *The minimum (left) and maximum (right)* EM *fraction of jets in events with final states of jets only (solid) and 2 jets + $\not\!\!E_T$ (dashed). The excesses in the 2 jets + $\not\!\!E_T$ data indicate the presence of cosmic rays or electrons.*

5.2.6 Muon Contamination

In $p\bar{p}$ collisions, muons occur in the 2 jets + $\not\!\!E_T$ final state through the decay of heavy quarks (c, b) or vector bosons (W, Z). In a heavy quark decay to a muon, the muon's direction is approximately the same as that of the quark. We identify such a decay by the presence of a muon aligned with a jet. We identify muons from a W or Z decay by the presence of a muon isolated from any jet. To reduce the numbers of W and Z background events (Section 6.1), we remove these isolated muons from the data sample.

We identify muons using the muon system and the calorimeter. We require the muon to fail no more than one of the 'flag word 4' criteria (Section 4.2.5) in the CF, and none in the EF. In the calorimeter, we require more than 65% of the hadronic layers along a central muon's path to be above the zero suppression threshold (HFRAC > 0.65). For forward muons, we require HFRAC > 0.75 and the energy in the last hadronic layer to be greater than zero (EFRAC > 0). If all of the hadronic layers along the muon's path are above threshold (HFRAC =1), we remove the EFRAC requirement. These requirements find muons with efficiencies of $(91.9 \pm 1.8)\%$ ($|\eta_d| \leq 0.7$), $(86.7 \pm 3.2)\%$ ($0.7 < |\eta_d| \leq 1.0$), and $(83.4 \pm 2.9)\%$ ($1.0 < |\eta_d| \leq 1.7$) [90].

In addition to the muon quality requirements, we impose the E_T and topological requirements $E_T > 15$ GeV and $|\eta_d| \leq 1.7$, respectively. The EF was not fully functional until run 89,000, so before this run we require muons to have $|\eta_d| \leq 1.0$. To ensure that a muon does not arise from a heavy quark decay, we impose a muon isolation requirement of ΔR(μ, nearest jet) > 0.5. We list the full set of muon requirements in Table 5.2.

5.2.7 Jet Energy Measurement Error

QCD jets production can result in a 2 jets + $\not\!\!E_T$ final state when we err in the E_T measurement of at least 1 jet. The trigger acolinearity requirement removes the

Cut
$E_T \geq 15$ GeV
$\lvert\eta_d\rvert \leq 1.0$ (Run $< 89{,}000$), $\lvert\eta_d\rvert \leq 1.7$ (Run $\geq 89{,}000$)
flag word $4 \leq 1$ (CF), flag word $4 = 0$ (EF)
Hfrac ≥ 0.65 (CF), Hfrac $= 1$ or (Hfrac ≥ 0.75 and Efrac > 0) (EF)
ΔR(μ, jet) > 0.5

Table 5.2: *Muon identification requirements used for rejection.*

dominant contribution of 2 jets production with at least 1 erroneously measured jet. However, QCD processes resulting in 3 jets can contribute to the 2 jets + $\not\!\!E_T$ final state. In a 3 jets event with at least 2 erroneously measured jets, the $\not\!\!E_T$ does not align with any of the jets in the event (Fig. 5.17).

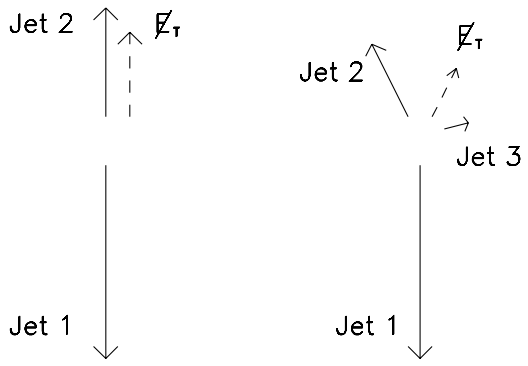

Figure 5.17: Left: *The dominant* QCD *background to the 2 jets + $\not\!\!E_T$ final state. An error in the E_T measurement of at least 1 jet causes the $\not\!\!E_T$.* Right: *The dominant* QCD *background after the imposition of the acolinearity requirement. An erroneously measured third jet shifts the $\not\!\!E_T$ away from any of the jets.*

The cross section for producing 3 jets events falls rapidly as the energy of the third jet increases. Thus, we expect the majority of these events to have 2 high E_T jets and a third low E_T jet. Measurement error of the third jet shifts the $\not\!\!E_T$ away from the other jets, but the angle between the $\not\!\!E_T$ and a jet is still small. In particular, since the 2 high E_T jets have approximately the same true E_T, a measurement error of one of these jets creates missing energy in roughly the same direction as the jet with the second largest measured E_T. Figure 5.18 shows the distribution of the $\Delta\phi$(jet 2, $\not\!\!E_T$) angle for the data sample and for a QCD sample (Section 6.3). We remove events with small values of $\Delta\phi$(jet 2,$\not\!\!E_T$) ($< 60^o$), as they arise predominantly from measurement errors.

5.3 Initial Selection

Using the selection requirements, we define a 2 jets + $\not\!\!E_T$ data sample in which we can search for new physical particles and processes. Table 5.3 shows the number of JET_2_MISS events that pass each successive requirement.

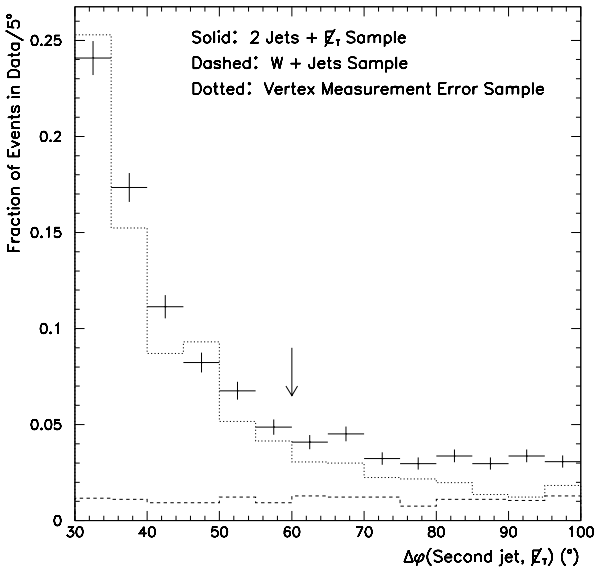

Figure 5.18: *The $\Delta\phi$(second jet, $\not\!\!E_T$) distribution for 2 jets + $\not\!\!E_T$ data (solid), W + jets data (dashed), and data with vertex measurement errors (dotted); the latter two samples have been normalized so that their sum fits the data. We remove events with an angle less than 60° between the second jet and $\not\!\!E_T$.*

Cut	# of Events
JET_2_MISS trigger	503,557
Leading jet $E_T \geq 50$ GeV	296,758
Second jet $E_T \geq 50$ GeV	113,718
$\not\!\!E_T \geq 40$ GeV	13,986
$\Delta\phi$(jet,$\not\!\!E_T$) $\geq 30^o$	3,127
No bad runs	2,242
No AIDA removed cells	1,888
|Main Ring E_T| ≤ 10 GeV	1,567
Leading or second jet $\|\eta_d\| \leq 1.0$; all jets $\|\eta_d\| \leq 4.0$	1,269
|Jet vertex - Primary vertex| < 15 cm	526
Jet EM Fraction cuts	448
No isolated muons	423
$\Delta\phi$(jet 2,$\not\!\!E_T$) $\geq 60^o$	253

Table 5.3: *The initial set of requirements imposed on the* JET_2_MISS *data sample and the number of events that pass each requirement.*

Chapter 6

Background

Standard Model processes resulting in the 2 jets + $\not\!\!E_T$ final state present a background to the potential new physical processes we aim to discover. We separately study the production of W or Z bosons plus jets, top quarks, and QCD jets.

6.1 W and Z Production

The initial state $p\bar{p}$ collisions produce W and Z bosons with cross sections on the order of 10^3 pb. Such production results in a 2 jets + $\not\!\!E_T$ final state when the incoming quarks radiate one or more high energy quarks or gluons, and when one or more of the W or Z decay products goes undetected.

The following 6 processes comprise the primary source of 2 jets + $\not\!\!E_T$ events

from W and Z production:

1. $(W^{\pm} \rightarrow \tau^{\pm}\nu \rightarrow$jet $\not\!\!E_T) + 1$ jet
2. $(Z^0 \rightarrow \nu\nu \rightarrow \not\!\!E_T) + 2$ jets
3. $(W^{\pm} \rightarrow \mathrm{e}^{\pm}\nu \rightarrow$jet $\not\!\!E_T) + 1$ jet
4. $(W^{\pm} \rightarrow l^{\pm}\nu \rightarrow \not\!\!E_T) + 2$ jets
5. $(Z^0 \rightarrow \tau^{\pm}\tau^{\mp} \rightarrow$jet $\not\!\!E_T) + 1$ jet
6. $(Z^0 \rightarrow \mu^{\pm}\mu^{\mp} \rightarrow \not\!\!E_T) + 2$ jets

The first 2 processes are irreducible Standard Model processes, with $\not\!\!E_T$ arising from our inability to measure neutrinos. The third process contributes when the electron 'fakes' a jet by depositing less than 95% of its energy in the EM region of the calorimeter (this type of contribution can occur in the first process as well, when the τ decays to an electron). The last three processes contribute when we fail to reconstruct electrons or muons because of detector inefficiencies.

To determine the contribution of each W or Z process, we use the data to measure its cross section and apply the initial topological and E_T requirements (Section 5.3) to a computer generated sample of events (Monte Carlo) to calculate the fraction of events passing these requirements.

6.1.1 Monte Carlo Samples

We generate samples of W and Z boson events using computer generators based on Feynman diagram calculations. For W and Z + 1 jet production, we use the PYTHIA generator (version 6.127) [91]; for W and Z + 2 jets production, we use the VECBOS generator (version 3.0) [92], modified to give equal weight to each generated event [93]. We require the generators' final state quarks and gluons to have at least 10 GeV of E_T, and we require the final state quarks or gluons in VECBOS to be separated by an $\eta - \phi$ radius of at least 0.5 (a smaller radius would cause the quarks or gluons to occupy the same cone and be reconstructed as 1 jet).

The final state quarks and gluons 'hadronize,' forming bound states of hadrons and producing the jets in the event. PYTHIA includes a model for hadronization, as well as for the production of additional quarks or gluons in the event (initial and final state radiation); VECBOS does not have such a model, so we use the hadronization program ISAJET (version 7.37) [94] to simulate these processes. We impose specific W or Z decays in both PYTHIA and VECBOS; to decay any taus in the event, we use TAUOLA [95] and ISAJET, respectively.

After running the generators to produce W and Z + jet(s) events, with full decays and hadronization, we use the PJET [96] program to build hadronic jets and impose initial E_T thresholds. These thresholds reduce the number of events

we need to run through the detector simulation program (GEANT 3.15 [97]), the slowest program in the chain. To improve the speed of the detector simulation, we use a library of jets (SHOWERLIB 2.0 [98]) to determine the response of the detector for each jet. For each event, we select jets from this library based on the following information: The particle content of the jets; the event vertex position; and the momenta, η, and ϕ of the jets.

After the event generation and detector simulation, we reconstruct the events using DØRECO. DØRECO runs AIDA on the events, but since the Monte Carlo does not simulate electronics failures or Uranium decay, all of the removed cells come from jets. We restore all hot cells to the closest jet if the hot cell is within a 0.5 cone of the jet. After cell restoration, we run the Monte Carlo version of CAFIX 5.1 to correct the jet energies. Table 6.1 shows the number of generated events for each W or Z Monte Carlo sample, the generator cross section, the PJET thresholds, and the number of events before and after the imposition of the thresholds.

The initial and final state radiation produced by PYTHIA can result in additional jets in the final state. For the $(W \to e\nu)$ + 1 jet and $(W \to \tau\nu)$ + 1 jet samples, an additional jet creates an overlap with the VECBOS $(W \to e\nu)$ + 2 jets and $(W \to \tau\nu)$ + 2 jets samples. To remove this overlap, we use the leptons in the events to separate the samples. The $(W \to e\nu)$ + 1 jet sample contributes to the

Monte Carlo Sample	σ (pb)	Events	PJET Thresholds (GeV)	Events
$(W^{\pm} \to e^{\pm}\nu) + 1$ jet	597	50,000	E_T^{ν} >10, E_T^e >20, E_T^{jet} >10	23,865
$(W^{\pm} \to \tau^{\pm}\nu) + 1$ jet	597	100,000	$2(E_T^{jet} > 30)$	11,531
$(W^{\pm} \to e^{\pm}\nu) + 2$ jets	325	31,133	E_T^e >20, $2(E_T^{jet}$ >10)	23,191
$(W^{\pm} \to \mu^{\pm}\nu) + 2$ jets	325	31,133	$2(E_T^{jet} > 30)$	2,274
$(W^{\pm} \to \tau^{\pm}\nu) + 2$ jets	325	31,133	$2(E_T^{jet} > 30)$	8,396
$(Z^{\pm} \to e^{\pm}e^{\mp}) + 1$ jet	127	50,000	$3(E_T^{jet}$ >15)	12,734
$(Z^{\pm} \to \tau^{\pm}\tau^{\mp}) + 1$ jet	127	100,000	$2(E_T^{jet} > 30)$	32,998
$(Z^{\pm} \to e^{\pm}e^{\mp}) + 2$ jets	31.6	36,715	$2(E_T^e$ >20), $2(E_T^{jet}$ >12.5)	18,674
$(Z^{\pm} \to \mu^{\pm}\mu^{\mp}) + 2$ jets	31.6	36,715	$2(E_T^{jet}$ >30)	2,779
$(Z^{\pm} \to \nu\nu) + 2$ jets	31.6	36,715	$2(E_T^{jet}$ >30)	2,779

Table 6.1: *The W and Z Monte Carlo samples, the generator cross sections, and the effects of the* PJET *thresholds.*

background when the electron has less than 95% of its energy in the EM region, thus appearing as one of the jets in the event. We require the $\eta - \phi$ distance (ΔR) between the electron and one of the 2 high E_T jets to be less than or equal to 0.3. For the $(W \to e\nu) + 2$ jets sample, we require this distance to be greater than 0.3, removing the overlap between these samples. We impose the same requirements on the τ decays to electrons in the $(W \to \tau\nu) + 1$ and 2 jets samples. In addition, we remove the τ decays to muons from the $(W \to \tau\nu) + 1$ jet sample and require the τ to decay to either an electron or a muon in the $(W \to \tau\nu) + 2$ jets sample.

6.1.2 W/Z Plus Jet(s) Cross Section Measurements

We measure the W and Z cross sections using the electron + $\not\!\!E_T$ and 2 electrons final states, respectively. We measure the cross sections for at least 1 or 2 hadronic jets in the final state and check the accuracy of the Monte Carlo by comparing its E_T and angular distributions to the data.

We use the triggers shown in Table 6.2 [80] to select the W and Z data samples. These triggers require a high E_T EM cluster at Level 1; a high EM fraction cluster (f_{EM} >0.85) at Level 1.5; and shape and isolation (EIS) requirements at Level 2. The EM2_EIS2_HI trigger requires a second EIS electron and the EM2_EIS_ESC trigger requires a second 'escape' (ESC) electron, which has no shape or isolation requirements. The EM1_EISTRKCC_MS trigger requires a track associated with central electrons (TRKCC) and $\not\!\!E_T >$ 15 GeV (MS). Since the trigger has a $\not\!\!E_T$ requirement, it includes a Level 1 Main Ring activity veto known as 'Good Cal,' which requires MR_VETO_LOW and MR_VETO_HIGH to be false. MR_VETO_LOW is set to true if there are 2 or more hits in the Main Ring veto counters while protons pass through DØ; MR_VETO_HIGH is set to true if there are 6 or more hits in the Main Ring veto counters during injection and transition of the acceleration cycle.

We identify electrons using the 5 variable likelihood ratio and the electron isolation fraction. We define a set of thresholds for these variables by studying

Trigger	Level 1	Level 2
EM2_EIS2_HI	2 (E_T >7 GeV)	2 (E_T >20 GeV, EIS)
EM2_EIS_ESC	2 (E_T >7 GeV)	E_T >20 GeV, EIS; E_T >16 GeV, ESC
EM1_EISTRKCC_MS	E_T >10 GeV	E_T >20 GeV,EIS,TRKCC; $\not\!\!E_T$ >15 GeV

Table 6.2: *The electron triggers used for* W *and* Z *cross section measurements. The triggers have an intermediate Level (1.5), which requires* EM *fraction > 0.85 and* E_T *> 12 GeV (15 GeV for* EM1_EISTRKCC_MS*).*

their effects on an electron dominated data sample (we choose this sample using the Z selection criteria described in the next section). Figures 6.1 and 6.2 show the efficiencies of various thresholds, along with our chosen requirements (marked by arrows).

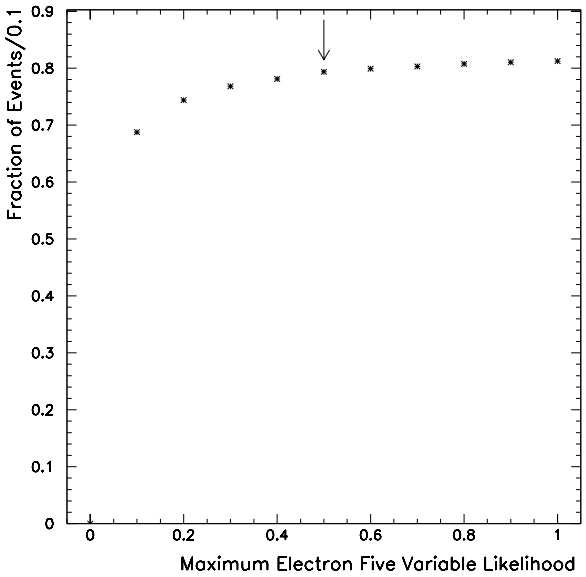

Figure 6.1: *The efficiency for an electron to have a 5 variable electron likelihood below a given value.*

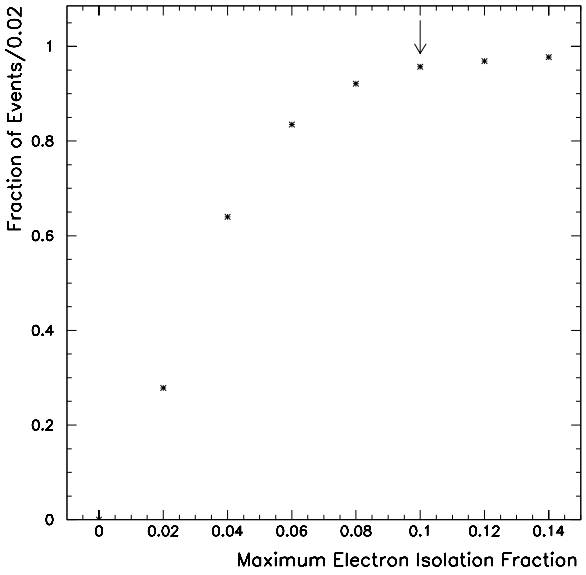

Figure 6.2: *The efficiency for an electron to have an isolation fraction below a given value.*

Z Cross Section

3.37% of Z boson decays result in 2 electrons [30], which have a combined invariant mass equal to the Z mass. We select events resulting from Z boson decay by imposing an invariant mass requirement on the 2 electrons data sample. We select this sample by requiring one central ($|\eta_d| \leq 1.1$) EM cluster away from a detector crack ($\Delta\phi_{e,crack}/\Delta\phi_{module} \geq 10\%$; see Fig. 6.3) with E_T above 25 GeV. We require the cluster to pass the trigger (EIS, TRKCC) and identification requirements (ϵ_5 and f_{iso}). We require a second high E_T (> 25 GeV) EM cluster in the central or forward region of the calorimeter ($|\eta_d| \leq 1.1$, or $1.5 \leq |\eta_d| < 2.5$), such that the invariant mass of the 2 clusters is within 10% of the Z mass (82

GeV/c^2 $\leq$ M$_{ee}$ $<$ 100 GeV/c^2; see Fig. 6.4).

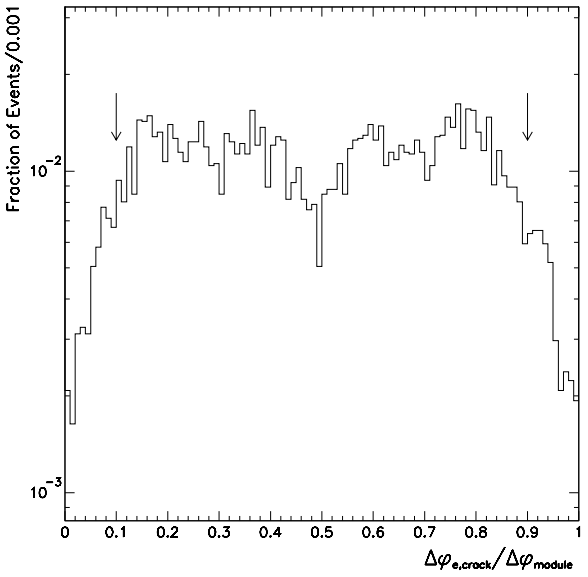

Figure 6.3: *The position of each* EM *cluster relative to the nearest detector crack. The dip in the center corresponds to the ϕ segmentation within the* EM *module.*

The background to this sample consists primarily of multi-jet events, in which 1 jet passes the electron identification requirements, and 2 high EM fraction jets have an invariant mass in the Z mass window. The background falls exponentially with increasing invariant mass (M_{ee}), and in the region of the Z mass it can be approximated as a linear function of M_{ee} [99]. Using this approximation, the integrated background in the M_{ee} windows of 73 to 82 GeV and 100 to 109 GeV is equal to the total background in the Z mass window of 82 to 100 GeV. Thus, to find the background in our Z sample, we add the number of events in the high and low windows. We do not include a systematic error for this procedure since

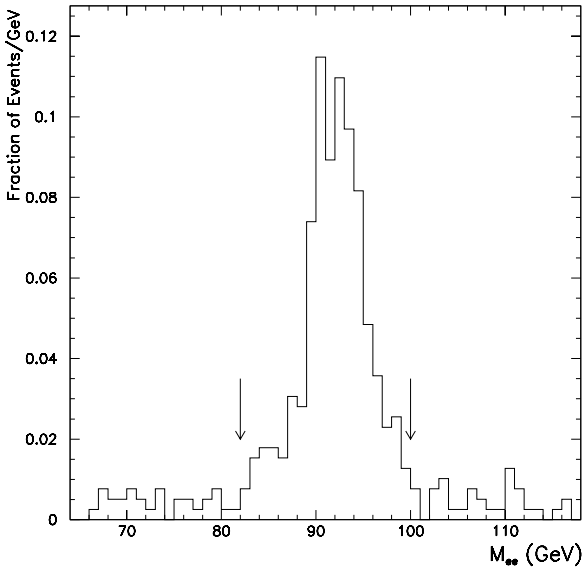

Figure 6.4: *The invariant mass of the 2* EM *clusters in the 2 electrons + jet(s) data sample.*

a more complete study of the background [99], which takes Drell-Yan electrons into account,[1] results in only a 1% change in the electron efficiency; this is small compared to our statistical error (see Table 6.3).

To measure the Z + jet(s) production cross section, we determine the fraction of events passing our selection requirements. We use Monte Carlo for all requirements except for electron identification. We measure the electron identification efficiency by separating the EM2_EIS_ESC Z sample into 2 subsamples: A '2 central' electrons sample (CC-CC); and a '1 central, 1 forward' electron sample (CC-EC). Using the CC-CC sample, we calculate the electron efficiency from the

[1]Drell-Yan electrons are produced by the 'decay' of a photon rather than a Z boson.

following equation:

$$\epsilon_{id} = \frac{2 \times (2\ good\ ele.\ events)}{2 \times (2\ good\ ele.\ events)\ +\ (1\ good\ ele.\ events)} \tag{6.1}$$

In this equation, 'good' electrons are electrons that pass our identification requirements, and '1 good electron events' have only 1 electron passing these requirements. We measure the electron efficiency separately for events with 1 or 2 (or more) jets (Table 6.3).

N_{jets}	1 Good Ele.	2 Good Ele.	Electron Eff.
$\geq$1	141	131	(65.0 $\pm$ 2.4) %
$\geq$2	21	14	(57.1 $\pm$ 7.1) %

Table 6.3: *The* CC *electron efficiencies for samples with at least 1 or 2 jets.*

We require the jets in this and the W sample to have $E_T \geq 25$ GeV, $0.1 \leq$ EM fraction < 0.95 (if the jet is not in the ICD region), and Coarse Hadronic (CH) fraction < 0.4. Since we do not reject events passing MICRO_BLANK and MRBS_LOSS, we use the CH fraction cut to remove Main Ring 'jets.'

After applying all the cuts to the Monte Carlo, we calculate the Z + jet(s) cross sections using the following equation:

$$\sigma \times BR = \frac{\frac{N_{CC-CC}}{(\epsilon_{id}^{CC})^2 + 2\epsilon_{id}^{CC}(\epsilon_{L2}^{CC} - \epsilon_{id}^{CC})} + \frac{N_{CC-EC}}{\epsilon_{id}^{CC}\,\epsilon_{L2}^{EC}}}{A_{MC} \times L}, \tag{6.2}$$

where A_{MC} is the Monte Carlo acceptance; L is the luminosity; ϵ_{L2}^{CC} and ϵ_{L2}^{EC}

are the measured Level 2 electron efficiencies in the CC, (98.3±0.2)%, and EC, (99.3±0.2)%, respectively; ϵ_{id}^{CC} is the electron identification efficiency in the CC; and N_{CC-EC} and N_{CC-CC} are the numbers of data events with 1 or 2 CC electrons, respectively. Using the measured luminosity of (111.9 ± 4.8) pb^{-1} we show the cross sections in Table 6.4. The first uncertainty listed is statistical and the second is systematic. The latter arises from jet energy scale and luminosity uncertainties.

N$_{jets}$	N_{CC-CC}	N_{CC-EC}	MC Acc.	σ×BR (pb)
≥ 1	259	114	(3.06 ± 0.08 ± 0.11)%	140 ± 10 ± 8
≥ 2	33	14	(1.85 ± 0.07 ± 0.13)%	32.0 ± 6.1 ± 2.5

Table 6.4: *The* Z + *jet(s) cross sections.*

To demonstrate the accuracy of the Monte Carlo distributions, we compare the data to the Monte Carlo in the Z + 2 jets sample (since the Z + 1 jet background to the 2 jets + $\not\!\!E_T$ sample is small, we do not make the same comparisons for this sample; see Table 6.6). We choose distributions that correspond to the following variables of interest in the 2 jets + $\not\!\!E_T$ sample: The E_T of the jets; $\not\!\!E_T$; and the angles between the jets and between each jet and $\not\!\!E_T$. In the 2 jets + $\not\!\!E_T$ data set, we do not measure the Z decay products (Section 6.1). Thus, the P_T of the Z corresponds directly to the $\not\!\!E_T$ in the data set. The distributions we use to compare Monte Carlo to data in the Z + 2 jets sample are: The E_T of the 2 jets; the P_T of the Z; $\Delta\phi(jet\ 1,\ jet\ 2)$; $\Delta\phi(jet\ 1,\ Z)$; and $\Delta\phi(jet\ 2,\ Z)$. Figure 6.5

shows these comparisons.

W Cross Section

To obtain a sample of W events, we use (84.5 ± 3.6) pb^{-1} [87] of data taken with the EM1_EISTRKCC_MS trigger. We reduce Main Ring effects by rejecting events passing the MRBS_LOSS and MICRO_BLANK conditions, and by requiring the E_T in the Coarse Hadronic region to be greater than -10 GeV. We select the W sample by requiring a central EM cluster that passes the electron fiducial, E_T, and identification cuts, and we require the $\not\!\!E_T$ to be greater than 25 GeV.

The dominant background to the W sample comes from multi-jet events (QCD), where one jet passes the electron requirements and at least one jet is mismeasured, resulting in $\not\!\!E_T$. To measure this background, we obtain a QCD sample by changing our electron cuts into 'anti-electron' cuts. For the anti-electron cuts we change the 5 variable likelihood and isolation cuts to $\epsilon_5 > 5$ and $f_{iso} > 0.1$, respectively. We normalize the QCD (anti-electron) sample to the W (electron) sample using low $\not\!\!E_T$ (< 15 GeV) events from a single electron trigger (EM1_ELE_MON). This sample gives the ratio of QCD events passing electron cuts to those passing anti-electron cuts. Of the 3284 and 469 events in the W + 1 jet and 2 jets samples, respectively, we predict 298 and 66 QCD events.

In addition to the QCD background, there is a small background from $t \rightarrow$

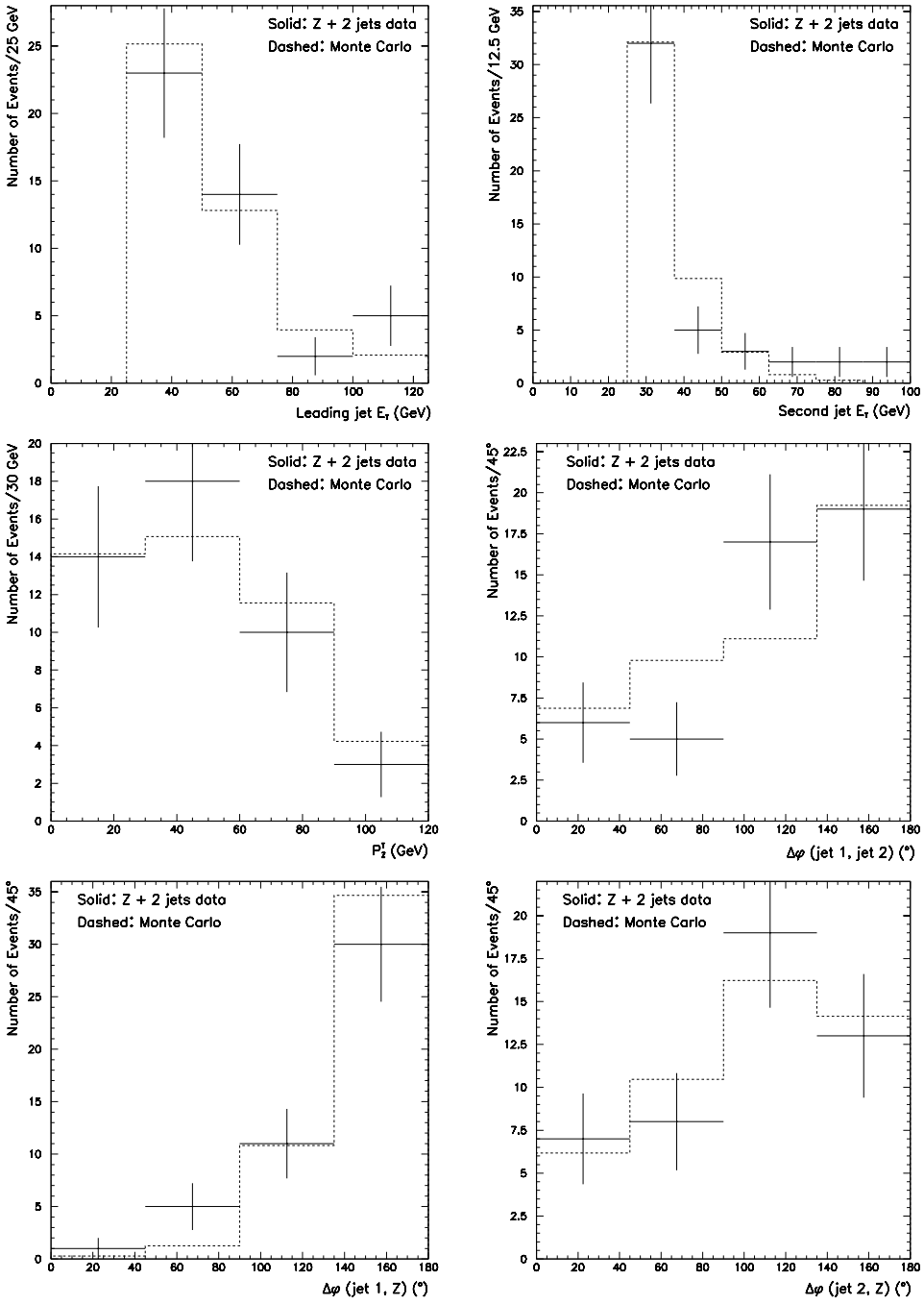

Figure 6.5: *Comparison of* Z + *2 jets data to Monte Carlo.* Top: *Leading jet* E_T *(left) and second jet* E_T *(right).* Middle: *Z* P_T *(left) and* $\Delta\phi(jet\ 1,\ jet\ 2)$ *(right).* Bottom: $\Delta\phi(jet\ 1,\ Z)$ *(left) and* $\Delta\phi(jet\ 2,\ Z)$ *(right).*

$W^+b\bar{t} \rightarrow W^-\bar{b}$ events, where one of the W bosons decays to jets and the other decays to an electron and a neutrino. We predict this background using the DØ measured cross section and Monte Carlo events generated with HERWIG (Section 6.2.2). We expect 22 $t\bar{t}$ events in the W + 2 jets data sample.

We show the W plus jet(s) cross sections in Table 6.5. As with the Z sample, we compare the data to the Monte Carlo plus background for the distributions of interest in our 2 jets + $\not\!\!E_T$ data sample. For the W + 1 jet data set, these distributions are: Electron E_T; $\not\!\!E_T$; jet E_T; $\Delta\phi(jet,\ electron)$; $\Delta\phi(jet,\ \not\!\!E_T)$; and $\Delta\phi(electron,\ \not\!\!E_T)$ (Fig. 6.6). For the W + 2 jets data set, the distributions are: W P_T; leading jet E_T; second jet E_T; $\Delta\phi(jet\ 1,\ jet\ 2)$; $\Delta\phi(jet\ 1,\ W)$; and $\Delta\phi(jet\ 2,\ W)$ (Fig. 6.7).

Sample	Events	MC Acc.	$\sigma\times$BR (pb)
W + 1 jet	2986	$(7.20 \pm 0.12 \pm 0.29)\%$	$755 \pm 34 \pm 44$
W + 2 jets	381	$(2.44 \pm 0.09 \pm 0.14)\%$	$324 \pm 45 \pm 23$

Table 6.5: *The* W + *jet(s) cross sections.*

6.1.3 W and Z Background Predictions

We calculate the total number of expected events from W and Z + jet(s) production using the following equation:

$$N = L \times \sigma \times A, \tag{6.3}$$

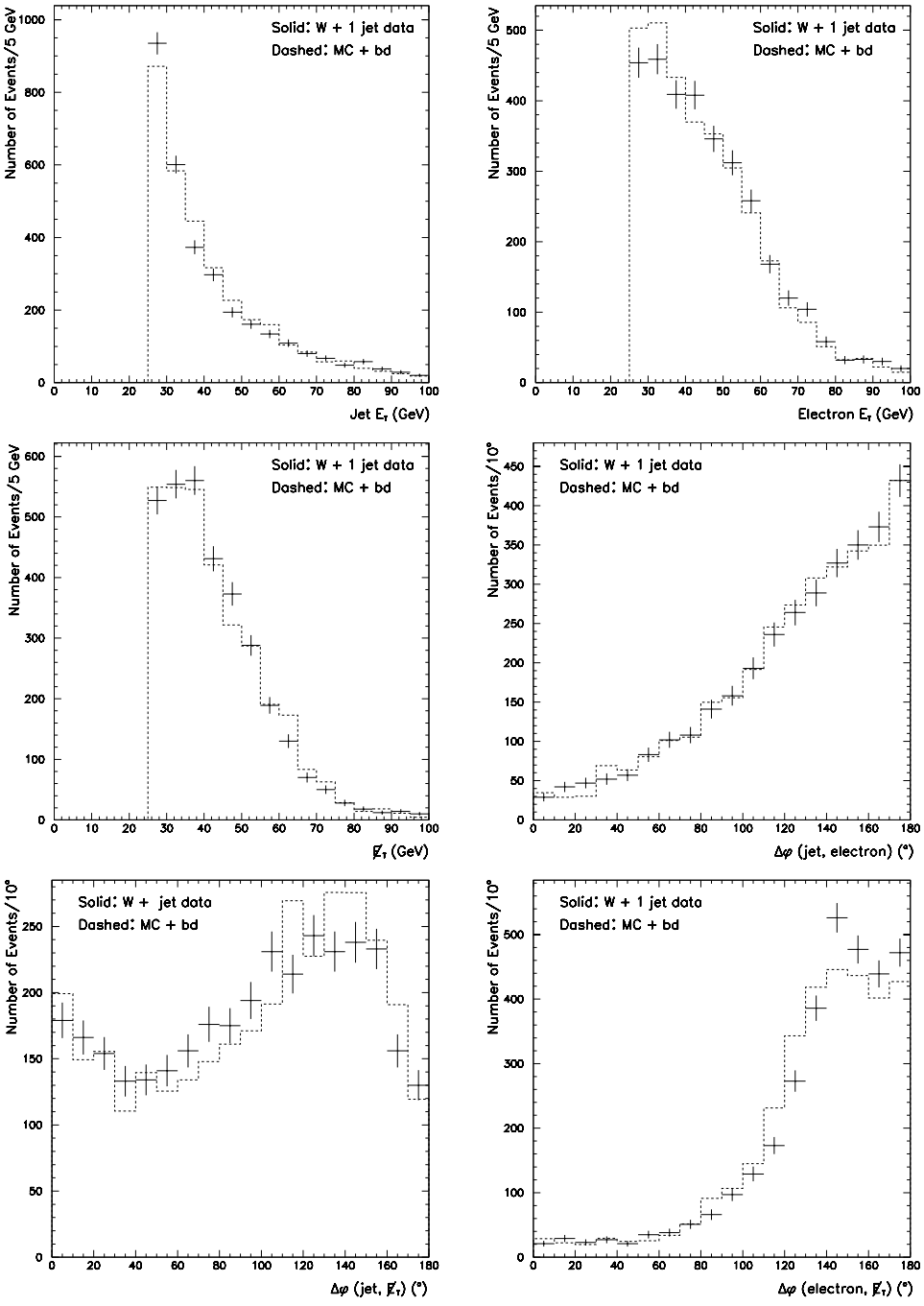

Figure 6.6: *Comparison of* W + *1 jet data to Monte Carlo plus QCD background.* Top: *Jet* E_T *(left) and electron* E_T *(right).* Middle: $\not\!\!E_T$ *(left) and* $\Delta\phi$*(jet, electron) (right).* Bottom: $\Delta\phi$*(jet,* $\not\!\!E_T$*) (left) and* $\Delta\phi$*(electron,* $\not\!\!E_T$*) (right).*

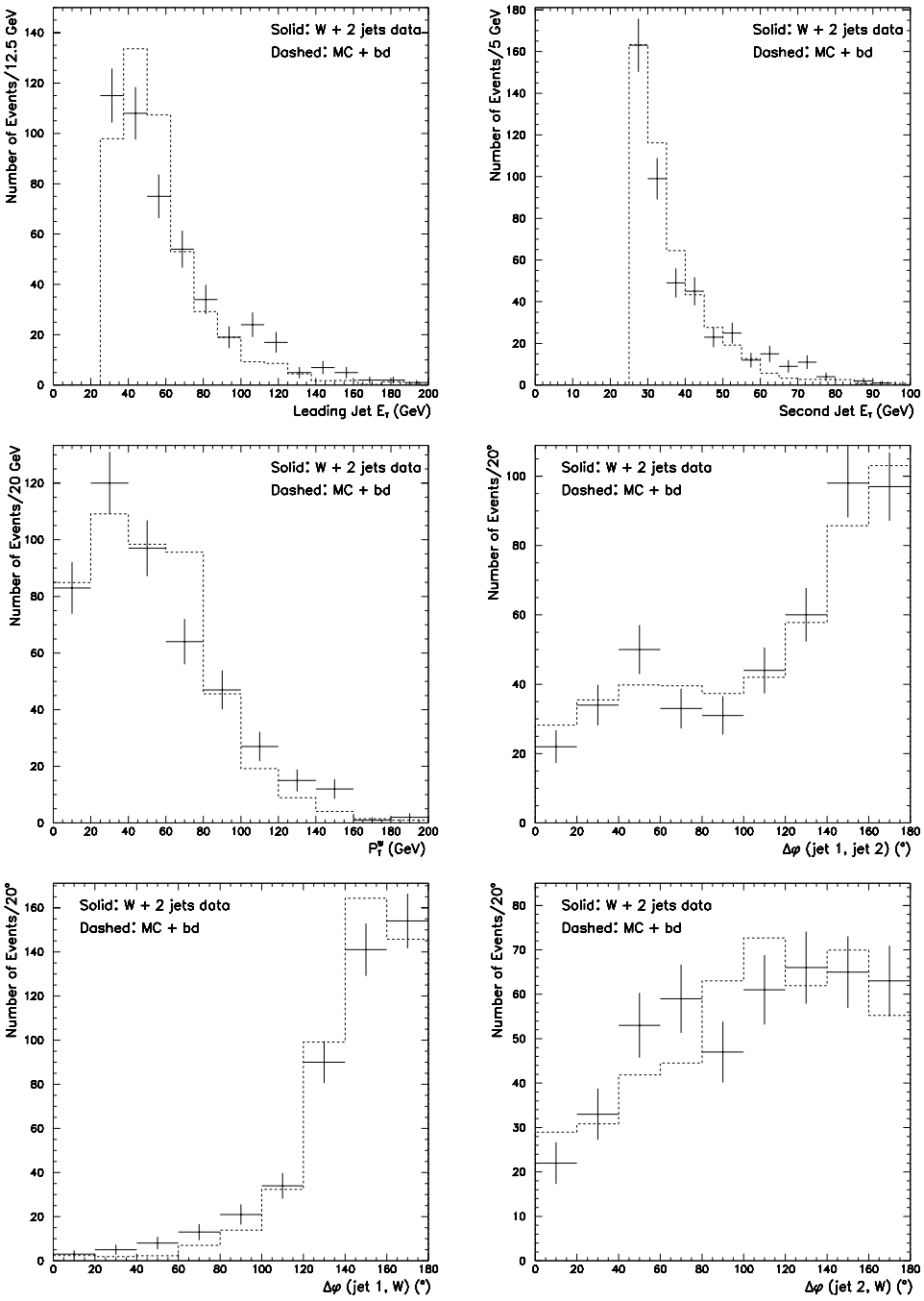

Figure 6.7: *Comparison of* W + *2 jets data to Monte Carlo plus QCD background.* Top: *Leading jet* E_T *(left) and second jet* E_T *(right).* Middle: W P_T *(left) and* $\Delta\phi(jet\ 1,\ jet\ 2)$ *(right).* Bottom: $\Delta\phi(jet\ 1,\ W)$ *(left) and* $\Delta\phi(jet\ 2,\ W)$ *(right).*

where L is the luminosity ((85.2 ± 3.7) pb^{-1}; Section 5.2.2), σ is the cross section of the particular process (Section 6.1.2), and A is the acceptance of our initial cuts (Section 5.3).

Background	$\sigma \times BR$ (pb)	Acceptance $\times 10^{-4}$	# of Events
$(W \to \tau\nu)$ + 1 jet	$755 \pm 34 \pm 44$	$7.49 \pm 0.87\ ^{+1.40}_{-1.20}$	$48.2 \pm 5.0\ ^{+9.7}_{-8.4}$
$(Z \to \nu\nu)$ + 2 jets	$192 \pm 37 \pm 15$	$25.6 \pm 2.6\ ^{+6.1}_{-3.8}$	$41.9 \pm 8.7\ ^{+10.7}_{-7.3}$
$(W \to e\nu)$ + 1 jet	$755 \pm 34 \pm 44$	$8.22 \pm 1.28\ ^{+2.09}_{-1.31}$	$52.9 \pm 7.0\ ^{+14.0}_{-9.3}$
$(W \to e\nu)$ + 2 jets	$324 \pm 45 \pm 23$	$3.14 \pm 1.00\ ^{+0.91}_{-0.90}$	$8.7 \pm 2.4 \pm 2.6$
$(W \to \mu\nu)$ + 2 jets	$324 \pm 45 \pm 23$	$7.53 \pm 1.55\ ^{+1.92}_{-1.53}$	$20.8 \pm 3.6\ ^{+5.6}_{-4.5}$
$(W \to \tau\nu)$ + 2 jets	$324 \pm 45 \pm 23$	$2.39 \pm 0.88\ ^{+0.58}_{-0.31}$	$6.6 \pm 1.8\ ^{+1.7}_{-1.0}$
$(Z \to \tau\tau)$ + 1 jet	$140 \pm 10 \pm 8$	$1.78 \pm 0.42\ ^{+0.53}_{-0.23}$	$2.1 \pm 0.4\ ^{+0.7}_{-0.3}$
$(Z \to \mu\mu)$ + 2 jets	$32.0 \pm 6.1 \pm 2.5$	$7.06 \pm 1.39\ ^{+1.65}_{-1.23}$	$1.9 \pm 0.4\ ^{+0.5}_{-0.4}$

Table 6.6: *Expected number of events from each W or Z background. The acceptance is the fraction of events passing the selection requirements described in Chapter 5.*

6.2 Top Quark Production

The initial state $p\bar{p}$ collisions produce top quarks with a cross section of about 10 pb. The top decays almost exclusively to a b quark and a W boson, and a 2 jets + $\not\!\!E_T$ final state results when the W decays to one or more undetected particles.

The production of the top quark occurs in association with either a b antiquark ('single top production') or an antitop quark ('top pair production'):

- $t\bar{b} \to W^+ b\bar{b} \to l^+ \nu b\bar{b} \to \not\!\!E_T +\ 2\ jets$

- $t\bar{t} \rightarrow W^+bW^-\bar{b} \rightarrow q\bar{q}'bl^-\nu\bar{b} \rightarrow 3\ jets + \not\!\!E_T + jet$,

In addition to these processes, there are processes that differ by only particle-antiparticle distinctions: Single antitop production ($b\bar{t}$); and $t\bar{t}$ production with the W decays reversed. In all processes, the 2 jets + $\not\!\!E_T$ final state results from a failure to measure the charged lepton in the event.

6.2.1 Single Top Production

We use equation 6.3 to determine the number of events in the 2 jets + $\not\!\!E_T$ data sample arising from single top production. We take the theoretical cross section of 2.57 ± 0.19 pb [100], which includes the next-to-leading-order process of quark radiation, and multiply by the fraction of W bosons decaying to muons and taus (2/9). To calculate the acceptance of our cuts, we use 198,095 Monte Carlo events generated by CompHEP 3.0 and run through PYTHIA 5.7, GEANT 3.15, and CAFIX 5.1 for hadronization, detector simulation, and energy corrections, respectively. The Monte Carlo sample does not include the electronic decay of the W, so we apply a correction to the background based on the ratio of electron to muon and tau events from the W + 2 jets samples (Table 6.6). This approximation is valid since both the single top and W + 2 jets backgrounds arise from a failure to measure a muon or electron. Table 6.7 shows the expected number of single top events in our 2 jets + $\not\!\!E_T$ data sample.

Background	$\sigma \times BR$ (pb)	Acceptance	# of Events
$tb \to l^{\pm}\nu$ + 2 jets	0.571 ± 0.043	(3.54 ± 0.04 $^{+0.24}_{-0.26}$) %	2.3 ± 0.3 ± 0.2

Table 6.7: *Expected number of events from single top production. The number of events includes a correction factor of 1.31 ± 0.16 to account for electron decays not included in the Monte Carlo.*

6.2.2 Top Pair Production

As with single top production, we use equation 6.3 to determine the number of events in the 2 jets + $\not\!\!E_T$ data set arising from top pair production. We take the DØ measured cross section of 5.9 ± 1.7 [30] and apply the ratio of W bosons decaying to muons and electrons (0.35; this includes the muonic and electronic decays of τ particles). We determine the acceptance of our cuts using 29,557 Monte Carlo events generated by HERWIG 5.7 and run through GEANT 3.15 and CAFIX 5.1 for detector simulation and energy corrections, respectively. Table 6.8 shows the expected number of top-antitop events in our 2 jets + $\not\!\!E_T$ data sample.

Background	$\sigma \times$BR (pb)	Acceptance	# of Events
$t\bar{t} \to l^{\pm}\nu$ + 4 jets	2.1 ± 0.4 ± 0.4	(6.69 ± 0.15 ± 0.85)%	12.0 ± 2.3 ± 2.8

Table 6.8: *Expected number of events from top pair production.*

6.3 Quark and Gluon Production

Light quark and gluon production are the most common processes at the Tevatron. The collider produces high E_T central hadronic jets with a cross section on the order of 10 μb. These processes have no intrinsic $\not\!\!E_T$, but if measurement errors in just one out of 10 million such events cause the event to pass our $\not\!\!E_T$ requirement, then quark and gluon production will be the largest single contribution to the background.

The vertex confirmation requirement and the $\Delta\phi$(jet 2,$\not\!\!E_T$) cut reduce quark and gluon events with vertex and jet energy measurement errors, respectively. We do not use Monte Carlo events to determine how many of these events remain; Monte Carlo events assume measurements with normal detector resolutions, while our sample contains pathological events outside of these resolutions. We thus use the data to predict the quark and gluon multijet background.

For our multijet sample with measurement errors, we use events where the deviation between a jet vertex and the reconstructed vertex (Δz) is between 15 cm and 50 cm (if the 2 highest E_T jets are central, we require both jet vertices to be in this range). We set the maximum Δz to 50 cm to get the most accurate prediction for the multijet dominated region of $\not\!\!E_T$ between 30 GeV and 40 GeV (Table 6.9). We use the events with $\Delta\phi$(jet 2, $\not\!\!E_T$) $< 60^o$ (another multijet dominated region) to normalize this sample to the data. Table 6.10 shows the number of events in our

multijet sample, the normalization factor, and the expected number of multijet events in the 2 jets + $\not\!\!E_T$ data set. In obtaining the first 2 quantities, we subtract the expected W, Z, and top backgrounds.

Event Sample	Number of Events
Multijet	162.1 ± 23.7
W, Z, and top	52.8 ± 7.0
Total background	214.9 ± 24.7
Data	225

Table 6.9: *The expected and observed numbers of events in the multijet dominated sample of $\not\!\!E_T$ between 30 GeV and 40 GeV.*

15 cm $< \Delta z \leq$ 50 cm	$(\frac{\Delta z<15\ cm}{15\ cm<\Delta z<50\ cm})_{\Delta\phi<60^o}$	Expected # of multijet events
41.4 ± 7.1	1.64 ± 0.25	68.0 ± 15.5 ± 14.9

Table 6.10: *The expected number of multijet events in the data sample with $\not\!\!E_T$ $\geq$ 40 GeV. Δz represents the distance between a jet vertex and the reconstructed vertex. $\Delta\phi$ represents the angle between the second highest E_T jet and $\not\!\!E_T$.*

Figure 6.8 compares the background distributions to the data distributions for the region of $\not\!\!E_T$ between 30 GeV and 40 GeV. We show the following distributions: Leading jet E_T; second jet E_T; $\Delta\phi(jet\ 1,\ jet\ 2)$; $\Delta\phi(jet\ 1,\ \not\!\!E_T)$; $\Delta\phi(jet\ 2,\ \not\!\!E_T)$; and the invariant mass of the 2 highest E_T jets (M_{inv}).

The events with vertex measurement errors provide an accurate model of the multijet background. Although we choose the Δz threshold to give the best agreement between the background and the data for the region 30 GeV $\leq$ $\not\!\!E_T$

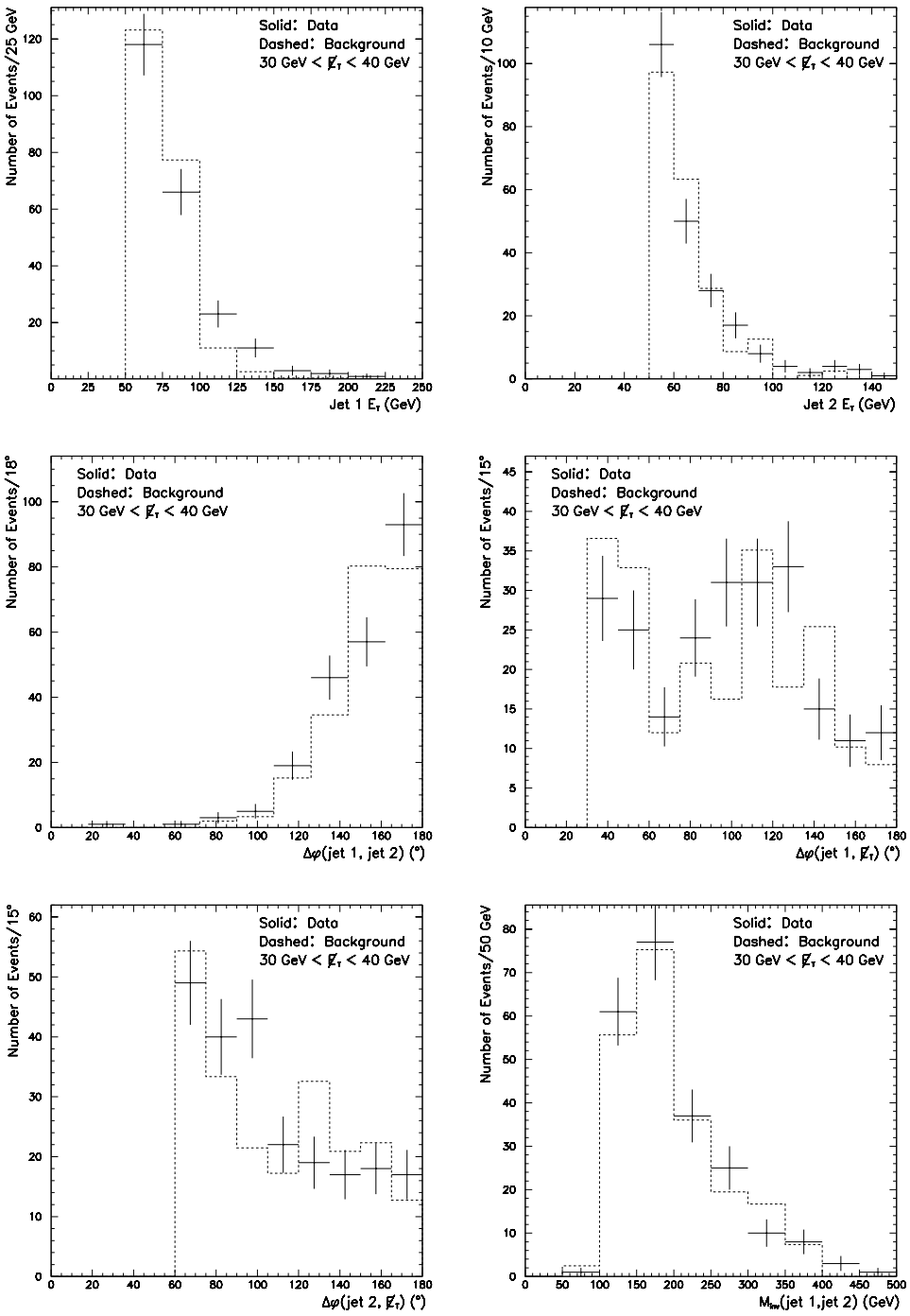

Figure 6.8: *Comparison of 2 jets + $\not\!\!E_T$ data to expected background for the 'test' region of 30 GeV $\leq \not\!\!E_T <$ 40 GeV.* Top: *Leading jet E_T (left) and second jet E_T (right).* Middle: *$\Delta\phi(j_1,j_2)$ (left) and $\Delta\phi(j_1,\not\!\!E_T)$ (right).* Bottom: *$\Delta\phi(j_2,\not\!\!E_T)$ (left) and the invariant mass of the 2 highest E_T jets (right).*

$<$ 40 GeV, different choices of Δz thresholds have only a small effect on the multijet prediction. Changing the maximum Δz from 50 cm to 100 cm increases the multijet prediction in the 30 GeV $\leq \not\!\!E_T <$ 40 GeV region by 22%, which we take to be the systematic error of the procedure (Table 6.10).

Chapter 7

Optimization

To search for leptoquark and WZ production, we focus on the regions where such production occurs. We make selection cuts to maximize the statistical significance of the excesses we would observe in the presence of these new physical processes.

7.1 Signal Monte Carlo

We use the PYTHIA 6.127 generator for all of our Monte Carlo samples except for the vector leptoquark samples; for these samples, we use CompHEP 3.0 and PYTHIA 5.7 for hadronization. We generate 10,000 events for each scalar leptoquark mass ranging from 70 GeV to 140 GeV (in 10 GeV intervals); 5,000 events for each vector leptoquark mass ranging from 120 GeV to 300 GeV (in 20 GeV

intervals); and 25,000 events for WZ production.

We run the PYTHIA output through PJET, requiring 2 jets with E_T above 30 GeV. Finally, we apply the detector simulation (SHOWERLIB 2.0) and energy corrections (CAFIX 5.1) to the events.

7.2 Signal and Background Distributions

To separate the signal events from background events, we choose from among the following 7 distributions: Leading jet E_T; second jet E_T; $\not\!\!E_T$; $\Delta\phi(jet\ 1,\ jet\ 2)$; $\Delta\phi(jet\ 1, \not\!\!E_T)$; $\Delta\phi(jet\ 2, \not\!\!E_T)$; and the invariant mass of the 2 jets ($M_{inv}(jet\ 1,\ jet\ 2)$). Figures 7.1 to 7.6 show these distributions and the ΔR distribution for the background and for 100 GeV scalar leptoquark, 200 GeV vector leptoquark, and WZ production.

7.3 Neural Network

We use a 'neural network' to determine the regions where leptoquark and WZ production result in the most statistically significant excesses. A neural network is a mathematical algorithm that provides the most effective separation between different classes of data. The network maps the input variables from each event into a single output variable, which ranges from 0 to 1. In the limit of infinitely

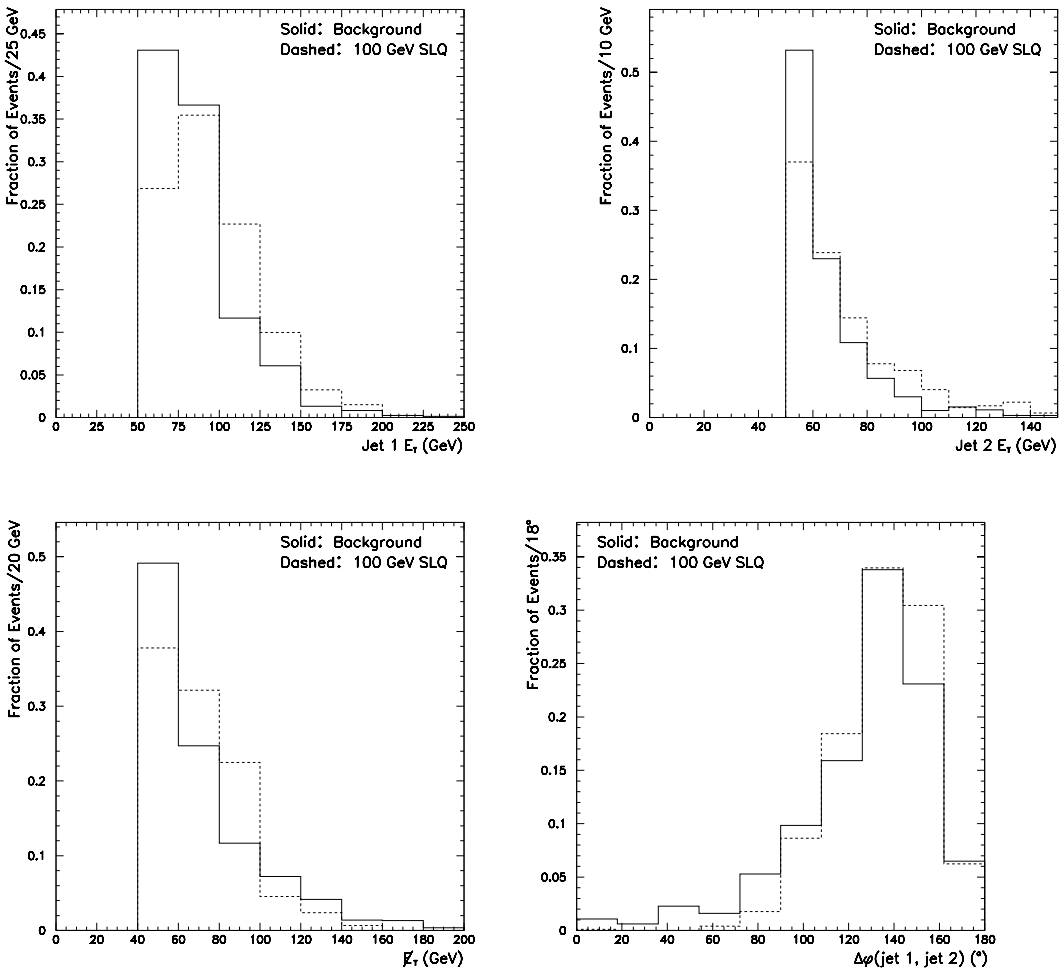

Figure 7.1: *Comparison of the expected background to 100 GeV scalar leptoquark production.* Top: *Leading jet E_T (left) and second jet E_T (right).* Bottom: $\not\!\!E_T$ *(left) and* $\Delta\phi(jet\ 1,\ jet\ 2)$ *(right).*

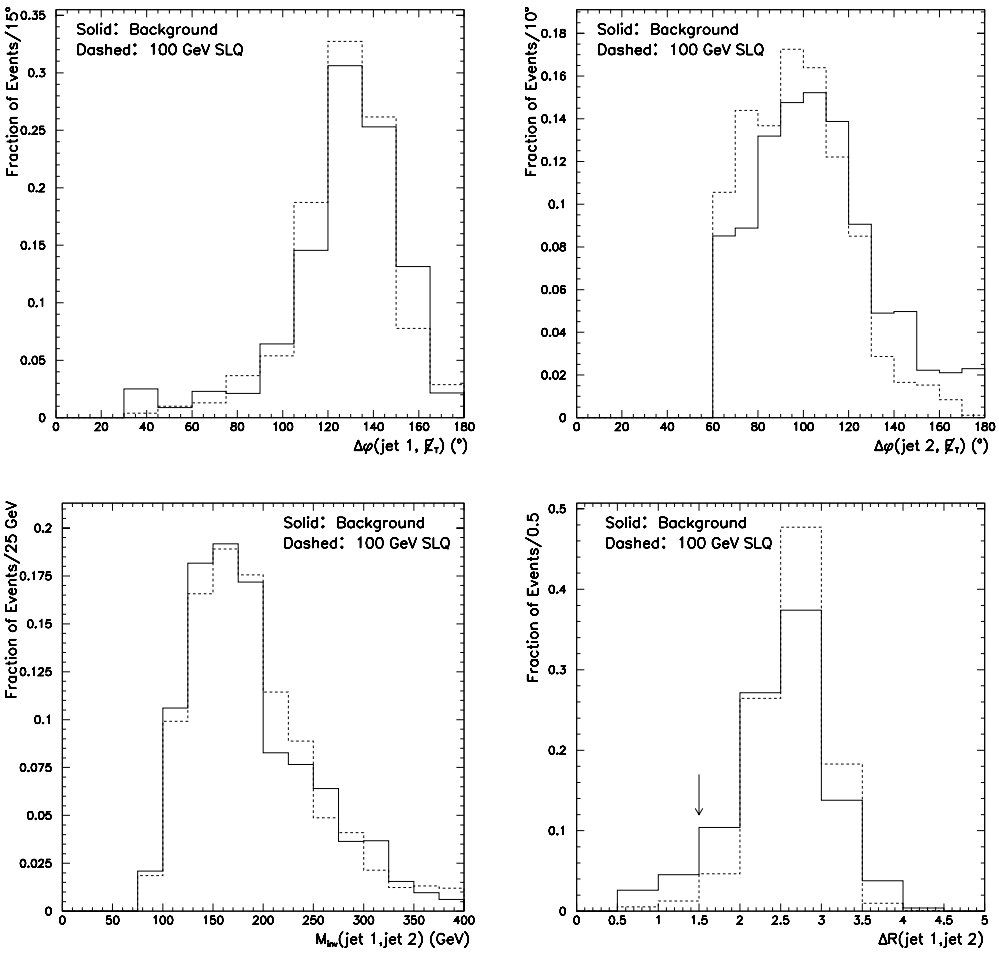

Figure 7.2: *Comparison of the expected background to 100 GeV scalar leptoquark production.* Top: $\Delta\phi(jet\ 1,\ \not\!\!E_T)$ *(left) and* $\Delta\phi(jet\ 2,\ \not\!\!E_T)$ *(right).* Bottom: $M_{inv}(jet\ 1,\ jet\ 2)$ *(left) and* $\Delta R(jet\ 1,\ jet\ 2)$. *The arrow marks the* ΔR *requirement we apply to reduce the systematic error due to the trigger (Section 5.1.2).*

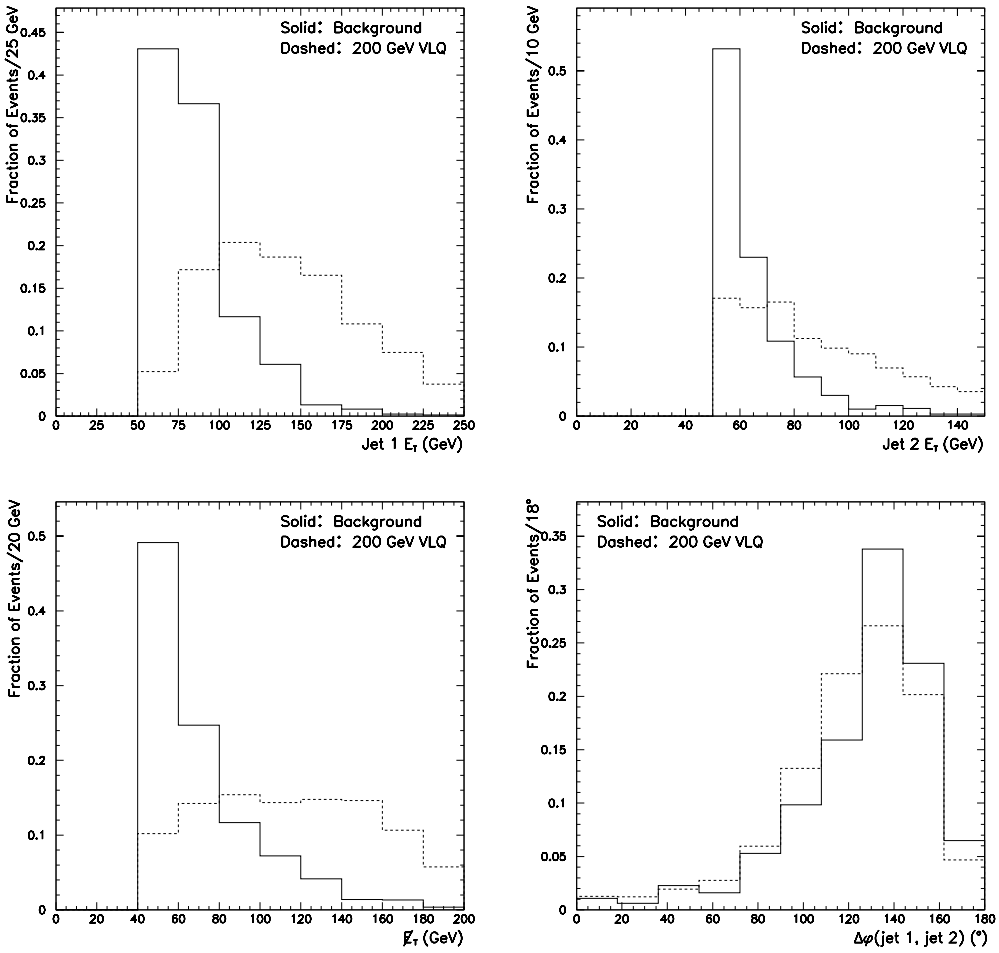

Figure 7.3: *Comparison of the expected background to 200 GeV vector leptoquark production.* Top: *Leading jet E_T (left) and second jet E_T (right).* Bottom: $\not\!\!E_T$ *(left) and* $\Delta\phi(jet\ 1,\ jet\ 2)$ *(right).*

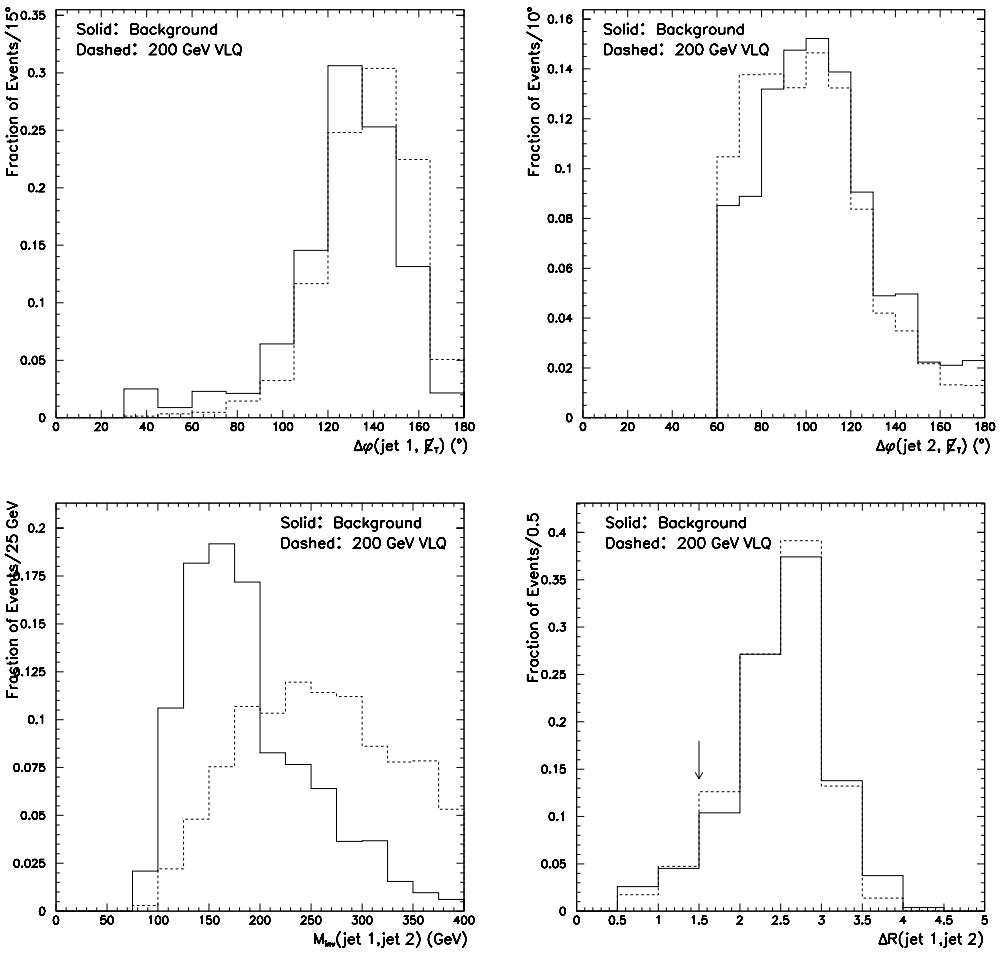

Figure 7.4: *Comparison of the expected background to 200 GeV vector leptoquark production.* Top: $\Delta\phi(jet\ 1,\ \not\!\!E_T)$ *(left) and* $\Delta\phi(jet\ 2,\ \not\!\!E_T)$ *(right).* Bottom: $M_{inv}(jet\ 1,\ jet\ 2)$ *(left) and* $\Delta R(jet\ 1,\ jet\ 2)$. *The arrow marks the* ΔR *requirement we apply to reduce the systematic error due to the trigger (Section 5.1.2).*

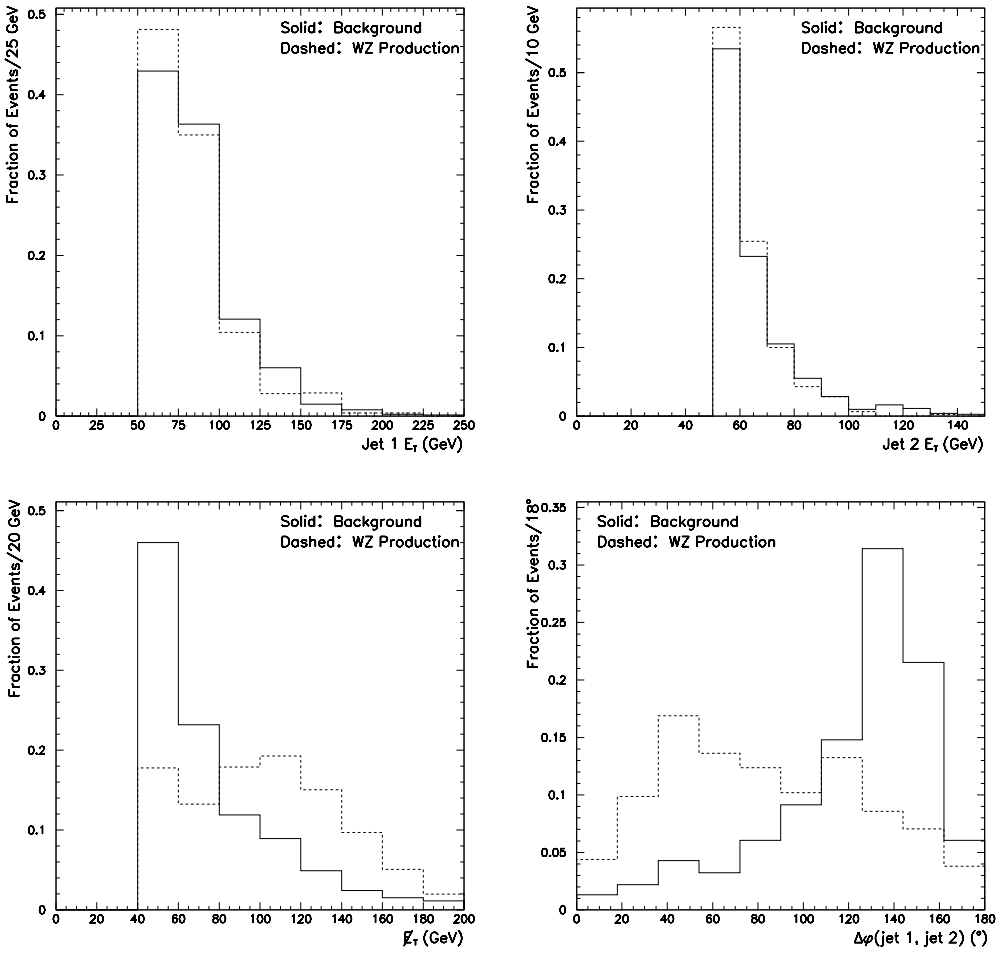

Figure 7.5: *Comparison of the expected background to WZ production.* Top: *Leading jet E_T (left) and second jet E_T (right).* Bottom: *$\not\!\!E_T$ (left) and $\Delta\phi$(jet 1, jet 2) (right).*

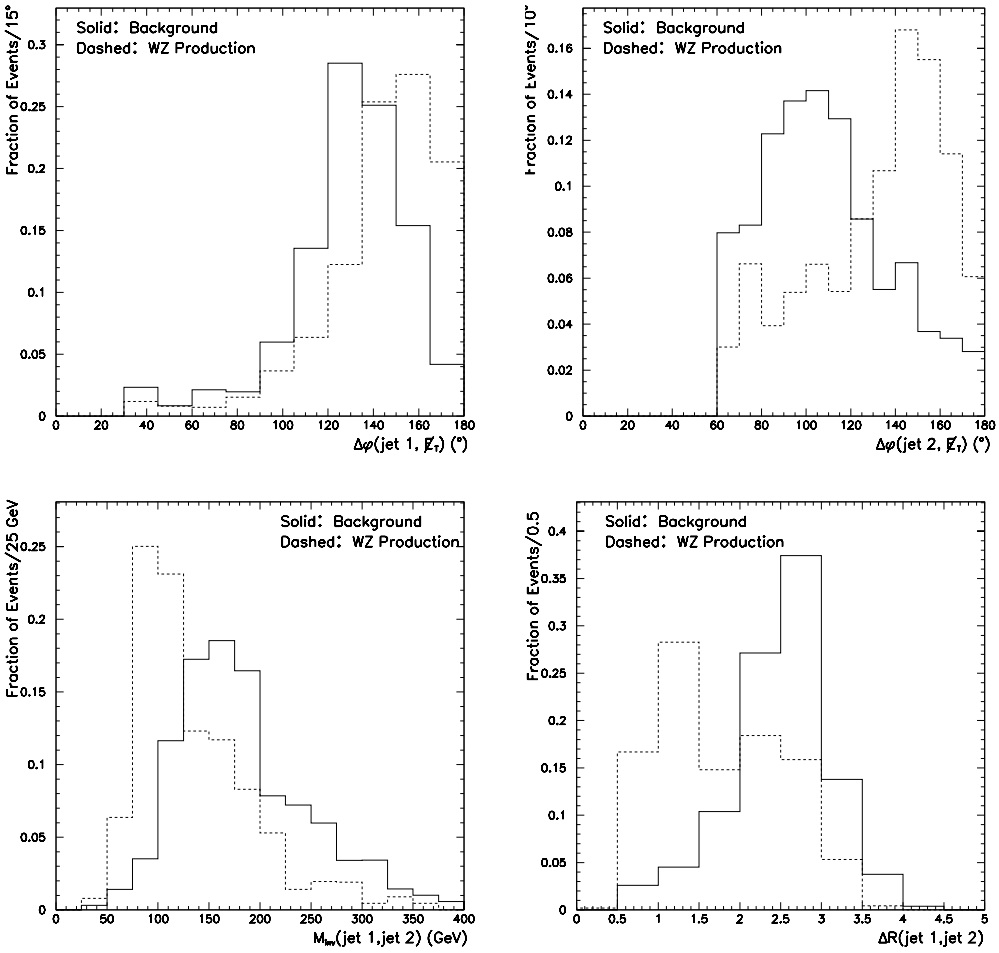

Figure 7.6: *Comparison of the expected background to WZ production.* Top: $\Delta\phi(jet\ 1,\ \not\!\!E_T)$ *(left) and* $\Delta\phi(jet\ 2,\ \not\!\!E_T)$ *(right).* Bottom: $M_{inv}(jet\ 1,\ jet\ 2)$ *(left) and* $\Delta R(jet\ 1,\ jet\ 2)$.

large event samples, the neural network output is:

$$D = \frac{s}{s+b}, \tag{7.1}$$

where s stands for the number of leptoquark and WZ events ('signal'), and b stands for the number of background events.

7.3.1 Algorithm

We use the neural network JETNET 3.4 [102] with 3 'layers' to map input distributions to a single output variable. We use 2 input distributions for the first layer, 5 intermediate variables in the second ('hidden') layer, and 1 output variable (equation 7.1).

The network mappings are linear mappings defined by a set of 'weights' (w_{ij}) and 'thresholds' (θ_i). Denoting the input variables by x_j, the first mapping can be expressed by the following equation:

$$y_i(x) = \sum_{j=1}^{2} w_{ij} x_j + \theta_i \tag{7.2}$$

In the second (and final) mapping, the network takes these 5 y_i values to the output variable. To ensure that the output is in the range [0,1], the network uses

the following 'transfer' function:

$$g(y_i(x)) = 1/(1 + e^{-2y_i(x)}) \tag{7.3}$$

The final result is then:

$$D(x) = g(\sum_{i=1}^{5} w_i g(y_i(x)) + \theta) \tag{7.4}$$

To separate between different classes of events, the network adjusts the weights ($w_{ij},\ w_i$) and thresholds ($\theta_i,\ \theta$) to minimize the mean square error (ϵ^2) between the discriminant (D_i) and the desired result:

$$\epsilon^2 = \frac{1}{N}\sum_{i=1}^{N}(D_i - t_i)^2 \tag{7.5}$$

In this equation, N corresponds to the total number of input background and signal events, and t_i corresponds to the desired output for a given event (1 for signal, 0 for background).

7.3.2 Procedure

Since we do not have an infinite number of events for background and signal samples, the neural network can find regions where statistical fluctuations create

an artificial excess of signal over background. To prevent such regions from biasing our signal and background predictions, we separate the samples into 'training' and 'prediction' samples. We build the training samples so that all background samples are weighted equally in the neural network. The training samples consist of 148 events each for background and signal. Table 7.1 shows the fractions of the original samples in the training and prediction samples.

Process	Training Sample	Prediction Sample
$(W \to \tau\nu) + 1$ jet	22.5%	77.5%
$(Z \to \nu\nu) + 2$ jets	15.8%	84.2%
$(W \to e\nu) + 1$ jet	46.3%	53.7%
$(W \to e\nu) + 2$ jets	30.8%	69.2%
$(W \to \mu\nu) + 2$ jets	31.3%	68.7%
$(W \to \tau\nu) + 2$ jets	33.3%	66.7%
$(Z \to \tau\tau) + 1$ jet	2.8%	97.2%
$(Z \to \mu\mu) + 2$ jets	2.7%	97.3%
$t\bar{t} \to l +$ jets	0.23%	99.77%
$tb \to l +$ jets	0.02%	99.98%
QCD	49.0%	51.0%
$(SLQ\overline{SLQ})_{100GeV}$	19.4%	80.6%
$(VLQ\overline{VLQ})_{200GeV}$	7.9%	92.1%
$(W \to 2$ jets$)(Z \to \nu\nu)$	37.8%	62.2%

Table 7.1: *The division of the event samples into 'training' and 'prediction' samples. All of the background training samples have equal weight.*

We select the 2 input distributions that minimize the neural network ϵ^2 (equation 7.5) for each signal sample. We optimize for 3 signal samples: 100 GeV scalar leptoquark; 200 GeV vector leptoquark; and WZ production. These leptoquark masses would provide an excess of $\sim 2\sigma$ if they exist.

To select the optimal region for signal production, we impose a threshold on each neural network's output variable. We choose the thresholds to maximize the significance of the excess that would arise from the new physical process under study. We measure this excess in terms of the number of standard deviations from the mean (σ). If there are no new physical proceses, the probability of an excess greater than 1σ is about 16%, and the probability of an excess greater than 2σ is less than 3%. The number of standard deviations of a given signal is:

$$n_\sigma = \frac{N_{signal}}{\sqrt{N_{signal} + N_{background} + \Delta N^2_{signal} + \Delta N^2_{background}}} \tag{7.6}$$

Chapter 8

Results

We have selected the data, predicted the background, and optimized for new physics. The last remaining step is to compare the data to the background to determine if we have evidence for new physical processes. We first examine the data and background distributions with only the initial cuts applied (Section 5.3); we then compare the number of data events to the number of background events for each new physical process under study.

8.1 Data and Background Distributions

The expected number of background events ($265.4 \pm 20.5\ ^{+26.5}_{-21.7}$) is consistent with the number of events in the data (253). We examine the extent of this consistency by comparing the data and background for the 8 distributions of

Section 7.2 (Figs. 8.1 and 8.2). The data are consistent with the background for all of the distributions.

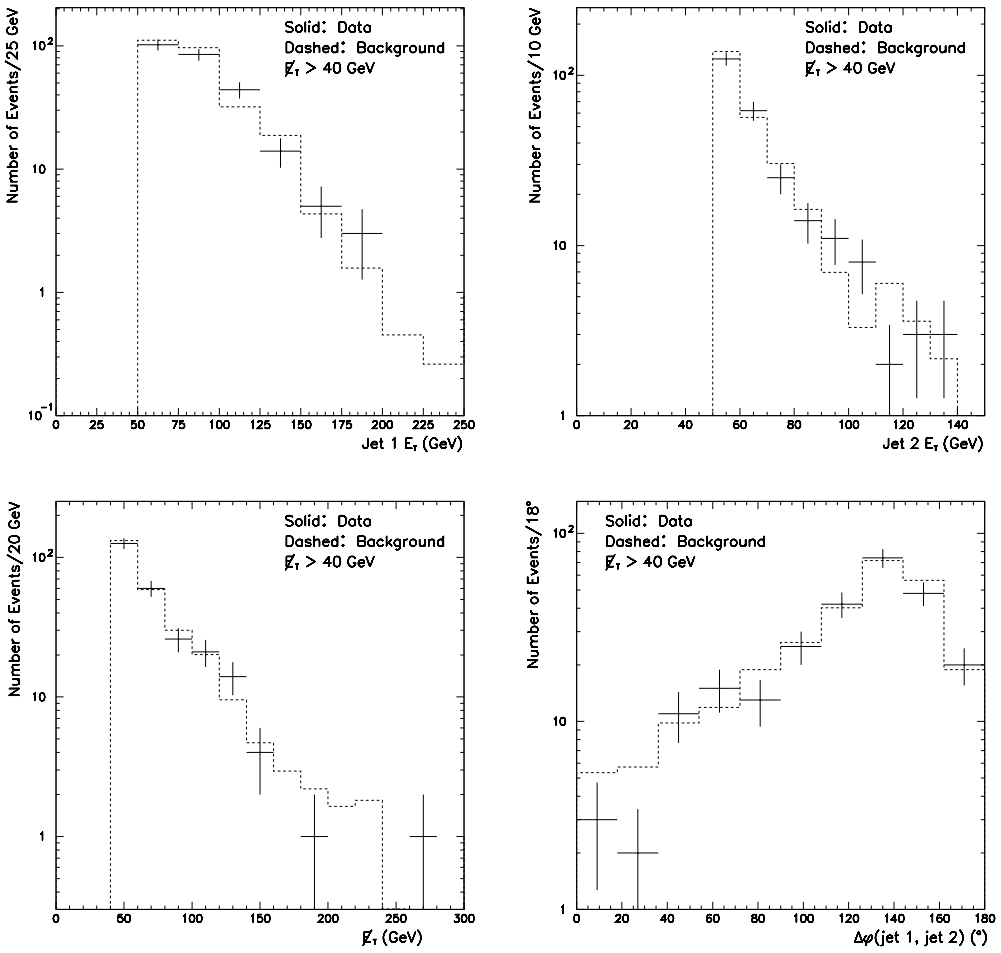

Figure 8.1: *Comparison of 2 jets + $\not\!\!E_T$ data to expected background.* Top: *Leading jet E_T (left) and second jet E_T (right).* Bottom: *$\not\!\!E_T$ (left) and $\Delta\phi$(jet 1, jet 2) (right).*

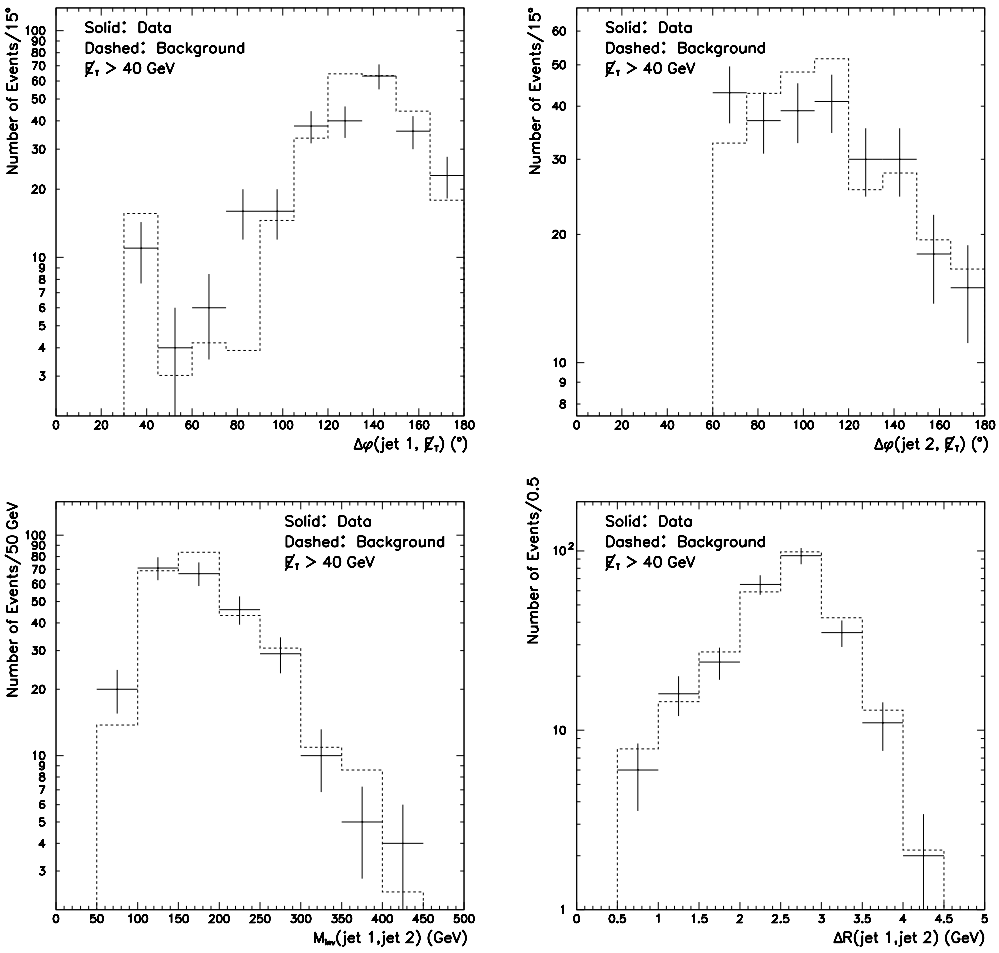

Figure 8.2: *Comparison of 2 jets + $\not\!\!E_T$ data to expected background.* Top: $\Delta\phi(jet\ 1,\ \not\!\!E_T)$ *(left) and* $\Delta\phi(jet\ 2,\ \not\!\!E_T)$ *(right).* Bottom: *The invariant mass (left) and the jet separation (right) of the 2 highest E_T jets.*

8.2 Scalar Leptoquarks

We optimize for the production of 100 GeV scalar leptoquarks using the $\not\!\!E_T$ and the $\Delta\phi(jet\ 1,\ jet\ 2)$ distributions (Fig. 8.3). Figure 8.4 shows the neural network output for the background, 100 GeV scalar leptoquarks, and the data; the arrow marks the cut chosen to maximize the expected excess. We show the numbers of expected and observed events after this cut in Table 8.1.

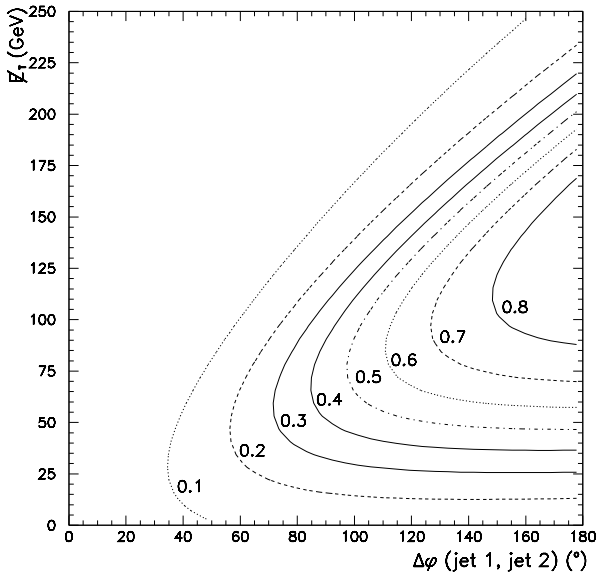

Figure 8.3: *The neural network contours in the $\Delta\phi(jet\ 1, jet\ 2)$-$\not\!\!E_T$ plane. Our optimization requires the neural network output variable to be greater than 0.6.*

The data are consistent with the background and we do not observe the excess expected from scalar leptoquark production. We determine the maximum cross section leptoquarks can have and still be consistent with the data, defining consistency as at least a 5% probability that the leptoquark hypothesis fits the data. We

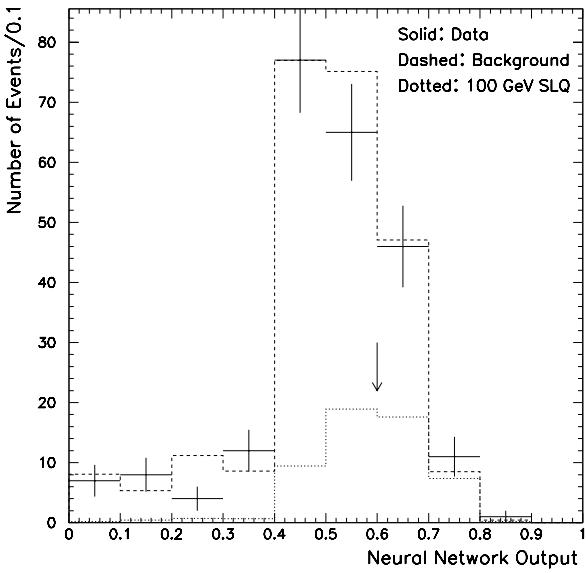

Figure 8.4: *The neural network output for the data (solid), background (dashed), and 100 GeV scalar leptoquarks (dotted). We mark the chosen cut with an arrow.*

N_{data}	$N_{background}$	N_{SLQ}	$\Delta n_\sigma^{expected}$	$\Delta n_\sigma^{obs.}$	Cross Section Limit (pb)
58	$56.0\ ^{+8.0}_{-8.2}$	$25.1\ ^{+2.1}_{-2.7}$	+2.1	+0.2	10.8

Table 8.1: *The data, background, and expected 100 GeV scalar leptoquark events. We show the expected number of σ excess, the observed number of σ excess, and the 95% confidence level cross section limit.*

show this '95% Confidence Level' cross section limit as a function of leptoquark mass in Fig. 8.5. This limit rules out the production of scalar leptoquarks below 99 GeV. It is the highest mass limit to date for first generation scalar leptoquarks decaying exclusively to quarks and neutrinos. The previous limit of 79 GeV was set with 7.4 pb^{-1} of Run 1A data at DØ [103]. Table 8.2 shows the current mass limit for each generation of scalar leptoquark.

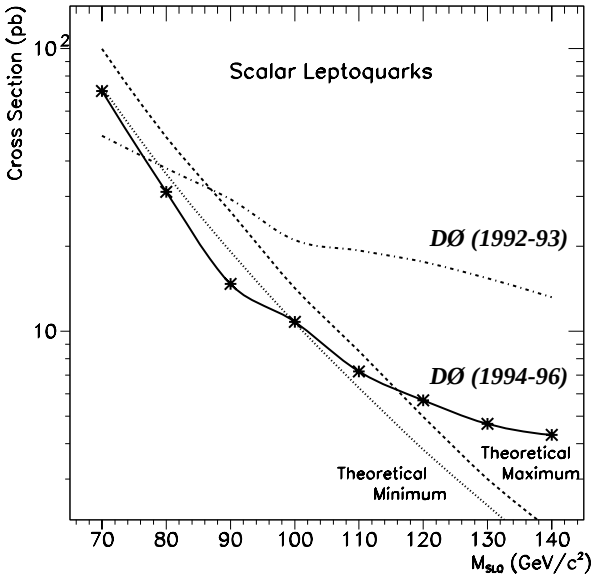

Figure 8.5: *The 95% Confidence Level cross section limit from the current data set (1994-96) and the Run 1A data set (1992-93). We show the minimum and maximum theoretical cross sections for scalar leptoquarks, assuming the leptoquarks decay exclusively to a quark and a neutrino.*

SLQ Generation	95% CL Mass Limit
First	99 GeV
Second	123 GeV
Third	148 GeV

Table 8.2: *The mass limit for each generation of scalar leptoquark decaying exclusively to a quark and a neutrino. The first generation limit is from this analysis; the second and third generation limits are from a search for leptoquarks at* CDF *[104]. The* CDF *analysis identifies one of the jets as arising from either a c or a b quark.*

The most general scalar leptoquark couplings allow for a leptoquark to decay into either a charged lepton or a neutrino. We denote the branching ratio of leptoquarks to charged leptons as β, and show the leptoquark mass limit as a function of β in Table 8.3. DØ has also searched for leptoquarks with the 2 jets + 2 electrons [105] and 2 jets + electron + $\not\!\!E_T$ [106] final states. We combine the current analysis with these results to set limits in the mass versus branching ratio plane in Fig. 8.6.

β	95% CL Mass Limit
0.0	99 GeV
0.05	95 GeV
0.1	92 GeV

Table 8.3: *Scalar leptoquark mass limits as a function of the leptoquark's branching ratio to quarks and charged leptons (β).*

The DØ limits are complementary to those from the electron-proton collider in Germany (HERA) and the electron-positron collider in Switzerland (LEP). Table 8.4 shows the limits for each type of first generation scalar leptoquark that could exist [108]. The leptoquarks in the table are categorized according to their weak and electromagnetic (Q_{EM}) charges. There are three categories of weak charge that scalar leptoquarks can have: None (S_0); up or down ($S_{1/2}$); and up-up, down-down, or up-down (S_1).

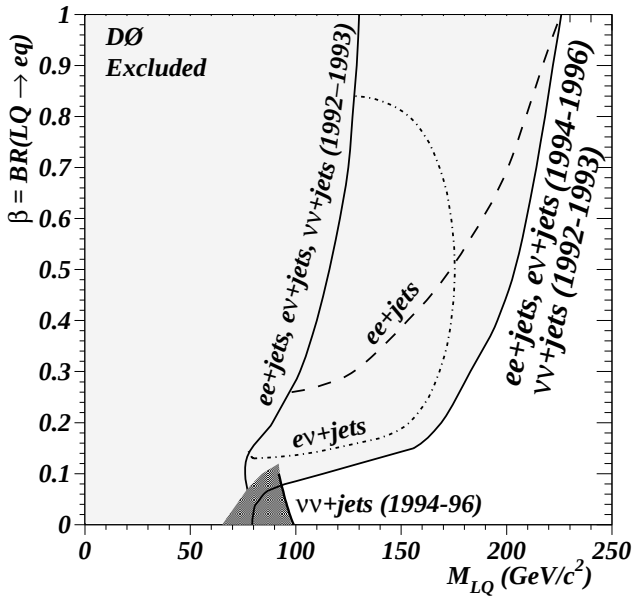

Figure 8.6: *The DØ 95% Confidence Level cross section limit versus branching ratio to eq for first generation scalar leptoquarks [103]. The current analysis excludes the darkened region.*

8.3 Vector Leptoquarks

We optimize for the production of 200 GeV/c^2 vector leptoquarks using the second jet E_T and the $\not\!\!E_T$ distributions (Fig. 8.7). Figure 8.8 shows the neural network output for the background, leptoquarks, and data; the arrow marks the cut chosen to maximize the expected excess. We show the numbers of expected and observed events after this cut in Table 8.5.

The data do not have the excess expected from vector leptoquark production. We show the corresponding 95% Confidence Level cross section limit as a function of leptoquark mass in Fig. 8.9. This limit rules out the production of vector lepto-

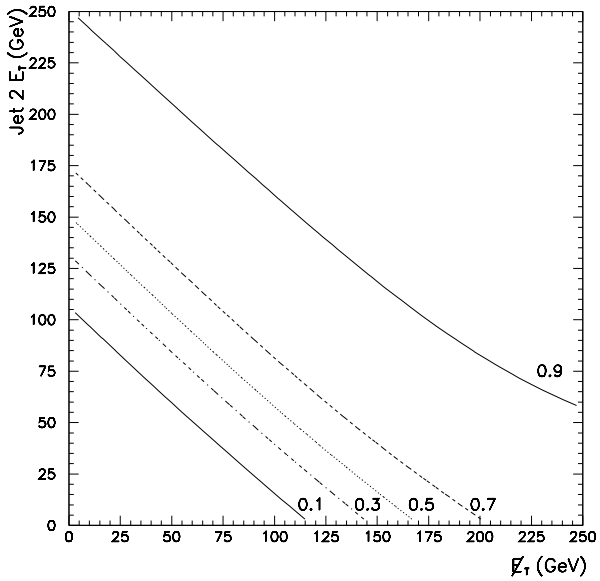

Figure 8.7: *The neural network contours in the $\not\!\!E_T$-second jet plane. Our optimization requires the neural network output variable to be greater than 0.7.*

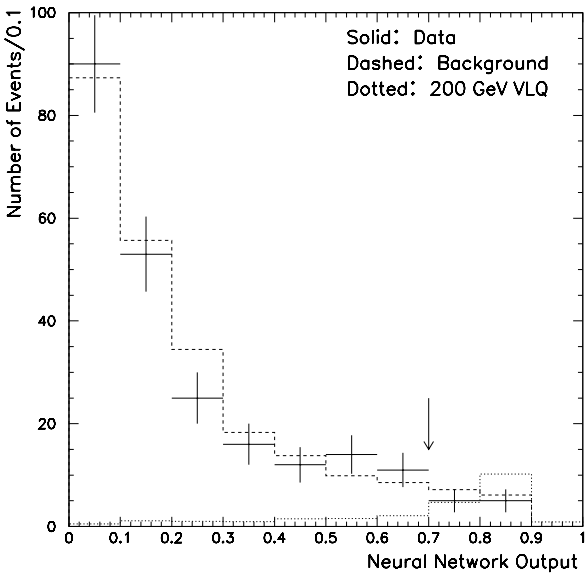

Figure 8.8: *The neural network output for the data (solid), background (dashed), and 200 GeV/c^2 vector leptoquarks (dotted). We mark the chosen cut with an arrow.*

LQ	Q_{EM}	Decay	BR($LQ \to eq$)	Mass Limit (GeV)
S_0	-1/3	$e_L u$, $\nu_L d$	0.5	204^b, $390^d_{(\lambda=0.31)}$, $620\lambda^e$
		$e_R u$	1	242^b, $300^d_{(\lambda=0.31)}$, $570\lambda^e$
$\tilde{S}_0$	-4/3	$e_R d$	1	242^b
$S_{1/2}$	-2/3	$\nu_L \bar{u}$	0	99^a
		$e_R \bar{d}$	1	242^b, $282^c_{(\lambda=0.31)}$, $320\lambda^e$
	-5/3	$e_L \bar{u}$	1	242^b, $282^c_{(\lambda=0.31)}$, $340\lambda^e$
		$e_R \bar{u}$	1	242^b, $282^c_{(\lambda=0.31)}$, $320\lambda^e$
$\tilde{S}_{1/2}$	+1/3	$\nu_L \bar{d}$	0	99^a
	-2/3	$e_L \bar{d}$	1	242^b, $271^c_{(\lambda=0.31)}$, $450\lambda^e$
S_1	+2/3	$\nu_L u$	0	99^a
	-1/3	$\nu_L d$, $e_L u$	0.5	204^b
	-4/3	$e_L d$	1	242^b, $420\lambda^d$

Table 8.4: *The mass limit for each type of first generation scalar leptoquark. We show:* [a]*Limits from this analysis;* [b]*Tevatron limits [103], which are independent of the the leptoquark coupling to quarks and leptons (λ);* [c]*limits from the ZEUS collaboration at HERA, with* $\lambda = \sqrt{4\pi\alpha_{em}} = 0.31$ *[109];* [d]*limits from the L3 collaboration at LEP [111], with* $\lambda = 0.31$*; and* [e]*limits from the ZEUS collaboration, with the coupling dependence shown [110].*

quarks below 178 GeV/c^2, 222 GeV/c^2, and 282 GeV/c^2, assuming the minimum cross section, Minimal Coupling, and Yang-Mills coupling, respectively. These mass limits are the highest limits to date for all generations of vector leptoquarks decaying exclusively to quarks and neutrinos. Table 8.6 shows the current and previous limits for different leptoquark generations and couplings. For first generation leptoquarks and leptoquarks with the minimum cross section, the previous limits are from a search for leptoquarks at DØ in Run 1A [103]. For second and third generation MC and YM leptoquarks, the previous limits are from a search

for leptoquarks at CDF in Run 1 [104].

N_{data}	$N_{background}$	N_{VLQ}	$\Delta n_{\sigma}^{expected}$	$\Delta n_{\sigma}^{obs.}$	Cross Section Limit (pb)
10	$13.3\ ^{+2.8}_{-2.6}$	15.8 ± 1.3	+2.6	-0.8	0.60

Table 8.5: *The data, background, and expected 200/c^2 GeV vector leptoquark events (assuming Minimal Coupling). We show the expected number of σ excess, the observed number of σ deficit, and the 95% Confidence Level cross section limit.*

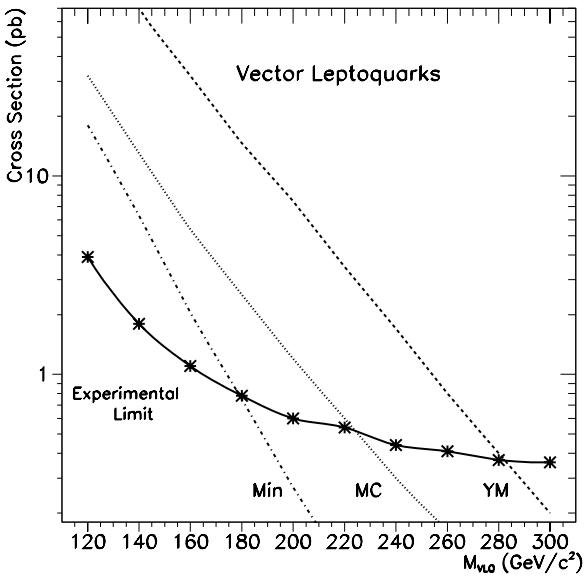

Figure 8.9: *The 95% Confidence Level cross section limit and the minimum theoretical cross sections for vector leptoquarks. We assume the leptoquarks decay exclusively to a quark and a neutrino.*

We show the vector leptoquark mass limits as a function of the leptoquark's branching ratio to a charged lepton and a quark in Table 8.7. We show the limits for the different types of vector leptoquarks in Table 8.8, using the Minimal Coupling cross section for DØ limits. We incorporate our results into the results

VLQ Generation	Minimum Cross Section	Minimal Coupling	Yang-Mills
First	178 (145)	222 (160)	282 (205)
Second	178 (145)	222 (171)	282 (222)
Third	178 (145)	222 (199)	282 (250)

Table 8.6: *The mass limits for each generation of vector leptoquark decaying exclusively to a quark and a neutrino. The limits are in units of GeV/c^2, and the previous limits are in parentheses.*

from DØ searches for second generation leptoquarks in the 2 jets + 2 muons and 2 jets + muon + $\not\!\!E_T$ [107] final states. We set limits in the mass versus branching ratio plane for MC and YM second generation vector leptoquarks (Figs. 8.10 and 8.11, respectively).

β	Mass Limit (Min)	Mass Limit (MC)	Mass Limit (YM)
0.0	178	222	282
0.05	175	220	280
0.1	172	217	276
0.15	169	214	272
0.20	165	209	267
0.25	161	204	263

Table 8.7: *Vector leptoquark mass limits as a function of the leptoquark's branching ratio to quarks and charged leptons (β). The limits are in units of GeV/c^2.*

8.4 WZ Production

We optimize for WZ production using the leading jet E_T and the $M_{inv}(jet\,1,\ jet\,2)$ distributions (Fig. 8.12). Figure 8.13 shows the neural network output for the

LQ	Q_{EM}	Decay	BR($LQ \to eq$)	Mass Limit (GeV)
V_0	-2/3	$e_L d$, $\nu_L \bar{u}$	0.5	275^b_{MC}, $560^d_{(\lambda=0.31)}$, $670\lambda^c$
		$e_R \bar{d}$	1	290^b_{MC}, $550\lambda^c$
$\tilde{V}_0$	-5/3	$e_R \bar{u}$	1	290^b_{MC}, $410\lambda^c$
$V_{1/2}$	-1/3	$\nu_L d$	0	222^a_{MC}
		$e_R u$	1	290^b_{MC}, $960\lambda^c$
	-4/3	$e_L d$	1	290^b_{MC}, $380\lambda^c$
		$e_R d$	1	290^b_{MC}, $960\lambda^c$
$\tilde{V}_{1/2}$	+2/3	$\nu_L u$	0	222^a_{MC}
	-1/3	$e_L u$	1	290^b_{MC}, $1060\lambda^c$
V_1	+1/3	$\nu_L d$	0	222^a_{MC}
	-1/3	$\nu_L \bar{u}$, $e_L d$	0.5	275^b_{MC}, $470^e_{(\lambda=0.31)}$
	-4/3	$e_L \bar{u}$	1	290^b_{MC}, $470^e_{(\lambda=0.31)}$

Table 8.8: *The mass limit for each type of first generation vector leptoquark. We show:* [a] *Limits from this analysis, assuming Minimal Coupling (MC);* [b] *Tevatron limits [103], assuming MC;* [c] *limits from the ZEUS collaboration at HERA, with the coupling dependence shown [110];* [d] *limits from the L3 collaboration at LEP [111], with* $\lambda = 0.31$*; and* [e] *limits from the ALEPH collaboration at LEP [112], with* λ*=0.31.*

background, WZ production, and the data; the arrow marks the cut chosen to maximize the expected excess. We show the number of expected and observed events after this cut in Table 8.9. There is a 1.2σ excess of events; in the absence of a signal, we expect an excess of this magnitude or greater to occur 11% of the time. The cross section limit is 72.3 pb, including the branching ratio to the 2 jets + $\not\!\!E_T$ final state. The total WZ production cross section limit is 548 pb; in the absence of an excess, this limit would be 363 pb. Our limit is not as strong as the previous limit of 47 pb set by DØ using the 3 electrons + $\not\!\!E_T$ and 2 electrons + muon + $\not\!\!E_T$ final states [113]. These final states have lower backgrounds than

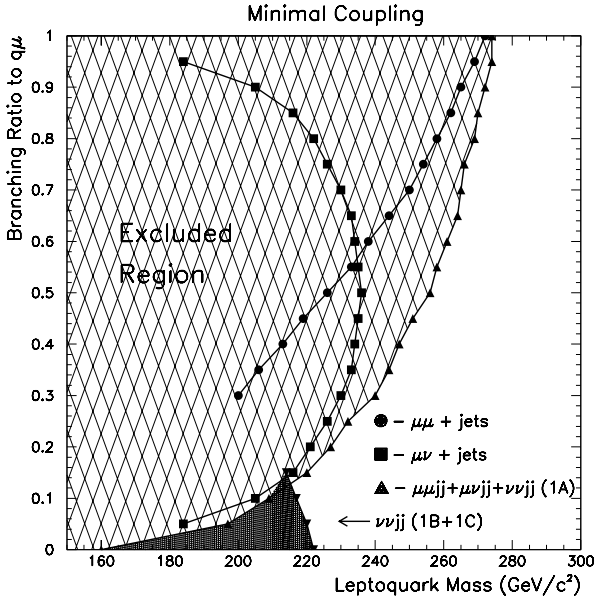

Figure 8.10: *The DØ 95% Confidence Level cross section limit versus branching ratio to μq for second generation vector leptoquarks with Minimal Coupling [107]. The current analysis (Runs 1B+1C) excludes the darkened region.*

the 2 jets + $\not\!\!E_T$ final state, contributing to the stronger limit. In addition, our trigger is not fully efficient for the region of jet E_T and jet separation where the majority of WZ events would be found.

N_{data}	$N_{background}$	N_{WZ}	$\Delta n_\sigma^{expected}$	$\Delta n_\sigma^{obs.}$	Cross Section Limit (pb)
20	$13.5\ ^{+3.3}_{-3.0}$	0.2	0.0	+1.2	72.3

Table 8.9: *The data, background, and expected WZ events. We show the expected number of σ excess, the observed number of σ deficit, and the 95% Confidence Level cross section limit for WZ production.*

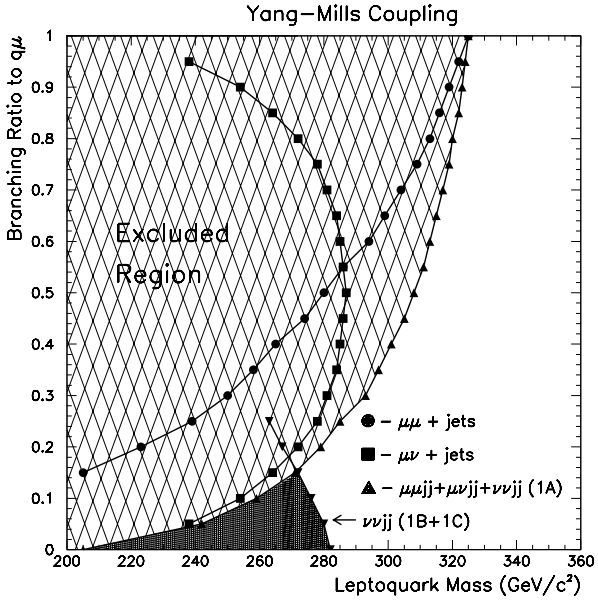

Figure 8.11: *The DØ 95% Confidence Level cross section limit versus branching ratio to μq for second generation vector leptoquarks with Yang-Mills coupling [107]. The current analysis (Runs 1B+1C) excludes the darkened region.*

8.5 Conclusion

We have searched for evidence of leptoquark and WZ production in the 2 jets + $\not\!\!E_T$ data set. The data are consistent with the Standard Model predictions and we find no evidence of new processes with the characteristics of leptoquark or WZ production (Chapter 2). Based on the consistency of the data with the Standard Model, we set the world's highest mass limits for vector leptoquarks and first generation scalar leptoquarks, in the case where the leptoquarks decay exclusively to quarks and neutrinos.

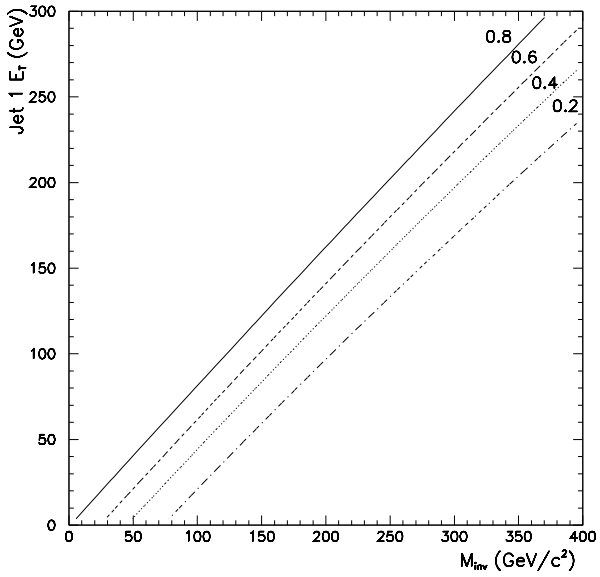

Figure 8.12: *The neural network contours in the $M_{inv}(jet\ 1, jet\ 2)$ and leading jet E_T plane. Our optimization requires the neural network output variable to be greater than 0.7.*

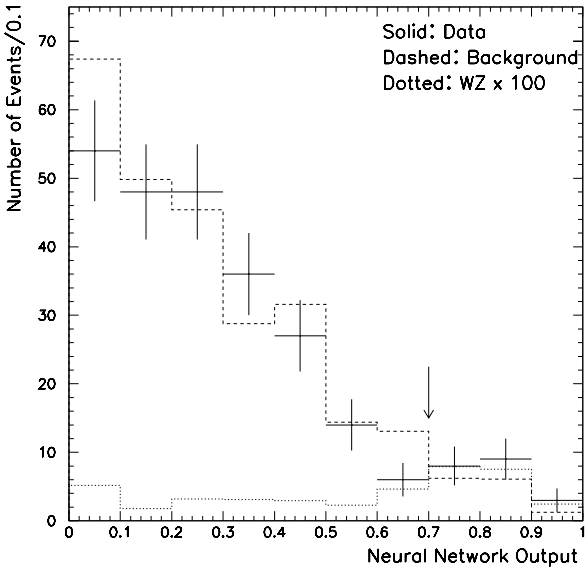

Figure 8.13: *The neural network output for the data (solid), background (dashed), and WZ production (dotted). We mark the chosen cut with an arrow.*

Bibliography

[1] I. Newton, *Philosophiae Naturalis Principia Mathematica,* London, 1686.

[2] I. Newton, *Opticks,* London, 1704.

[3] A. Einstein, *Ann. der Phys.* **17**, 891 (1905).

[4] C. Guye and C. Lavanchy, *Archives des Sciences Physiques et Naturelles* **42**, 286, 353, 441 (1916); K. Glitscher, *Ann. der Phys.* **52**, 608 (1917).

[5] A. Einstein, *Ann. der Phys.* **35**, 898 (1911).

[6] J. C. Maxwell, *A Treatise on Electricity and Magnetism,* Oxford: Clarendon Press, 1891.

[7] A. Einstein, *Ann. der Phys.* **17**, 132 (1905).

[8] W. Heisenberg, *Z. Phys.* **35**, 618 (1927).

[9] P. A. M. Dirac, *Proc. Roy. Soc. London* **A117**, 610 (1928).

[10] P. A. M. Dirac, *Proc. Roy. Soc. London* **A133**, 60 (1931).

[11] C. Anderson, *Science* **77**, 432 (1933).

[12] H. A. Bethe and E. Fermi, *Z. Phys.* **77**, 296 (1932).

[13] E. Fermi, *Ric. Scientifica* **4(2)**, 491 (1933); *Nuova Cimento* **2**, 1 (1934); *Z. Phys.* **88**, 161 (1934).

[14] H. Yukawa, *Proc. Phys.-Math. Soc. Japan* **17**, 48 (1935).

[15] L. Brown, ed., *Renormalization: From Lorentz to Landau (and Beyond),* New York: Springer-Verlag, 1993.

[16] W. E. Lamb Jr. and R. C. Retherford, *Phys. Rev.* **72**, 241 (1947); H. A. Bethe, *Phys. Rev.* **72**, 339 (1947); H. M. Foley and P. Kusch, *Phys. Rev.* **72**, 1256 (1947); J. Schwinger, *Phys. Rev.* **73**, 417 (1948); J. A. Wheeler, *Ann. NY Acad. Sci.* **48**, 219 (1946); M. Deutsch, *Phys. Rev.* **82**, 455 (1951).

[17] J. D. Jackson, in K. W. Ford, ed., *Elementary Particle Physics and Field Theory,* New York, NY: W. A. Benjamin, Inc, 1963.

[18] C.N. Yang and R.L. Mills, *Phys. Rev.* **96**, 191 (1954).

[19] M. Gell-Mann, *Phys. Lett.* **8**, 214 (1964); J. Joyce, *Finnegans Wake,* New York: Viking, 1939.

[20] H. R. Rubinstein and H. Stern, *Phys. Lett.* **21**, 447 (1966); Ya. B. Zel'dovich and A. D. Sakharov, *Sov. J. Nucl. Phys.* **4**, 283 (1967); C. G . Callan and D. J. Gross, *Phys. Rev. Lett.* **22**, 156 (1969); D. H. Perkins, in J. D. Jackson, A. Roberts, and R. Donaldson, eds., *Proceedings of the XVI International Conference on High Energy Physics,* Batavia, IL: National Accelerator Laboratory, 1972.

[21] D. J. Gross and F. Wilczek, *Phys. Rev. Lett.* **30**, 1343 (1973).

[22] R. P. Feynman, *Phys. Rev.* **76**, 749, 769 (1949).

[23] S. Glashow, *Nucl. Phys.* **22**, 579 (1967). S. Weinberg, *Phys. Lett.* **12**, 132 (1967). A. Salam, *Elementary Particle Physics,* N. Svartholm ed., 367 (1968).

[24] G. Arnison *et al.*, *Phys. Lett.* **122B**, 103 (1983); **126B**, 398 (1983); P. Bagnaia *et al.*, *Phys. Lett.* **129B**, 130 (1983); M. Banner *et al.*, *Phys. Lett.* **118B**, 476 (1983).

[25] S. Abachi *et al.*, *Phys. Rev. Lett.* **74**, 2632 (1995); The CDF Collaboration, *Phys. Rev. Lett.* **75**, 3997 (1995).

[26] DONUT Collaboration, *hep-ex/0012035* (2000).

[27] The DELPHI Collaboration, *Phys. Lett.* **B499**, (2001) 23; The OPAL Collaboration, *Phys. Lett.* **B499**, (2001) 38; ALEPH Collaboration, *Phys. Lett.* **B495**, (2000) 1; L3 Collaboration, *Phys. Lett.* **B495**, (2000) 18.

[28] P.W. Higgs, *Phys. Rev. Lett.* **12**, 132 (1964).

[29] S. Weinberg, *Phys. Rev.* **D13**, 974 (1976); L. Susskind, *Phys. Rev.* **D20**, 2619 (1979).

[30] Particle Data Group, *Eur. Phys. J.* **C15**, 1 (2000).

[31] H. Georgi and S.L. Glashow, *Phys. Rev. Lett.* **32**, 438 (1974).

[32] P. Langacker, *Phys. Rep.* **C72**, 185 (1981); Y. Hayato *et al.*, *Phys. Rev. Lett.* **83**, 1529 (1999).

[33] R. N. Mohapatra, *Phys. Rev.* **D9**, 3461 (1974); F. Wilczek and A. Zee, *Phys. Rev. Lett.* **42**, 421 (1979).

[34] C.-K. Chang, *Phys. Rev.* **D5**, 950 (1972); J. C. Pati and A. Salam, *Phys. Rev.* **D10**, 275 (1974); O. W. Greenberg and C. A. Nelson, *Phys. Rev.* **D10**, 2567 (1974).

[35] J. C. Pati and A. Salam, *Phys. Rev. Lett.* **31**, 661 (1973); R. N. Mohapatra, *Phys. Rev.* **D11**, 2558 (1975); G. Senjanovic and R. N. Mohapatra, *Phys. Rev.* **D12**, 1502 (1975).

[36] Y. A. Gol'fand and E. P. Likhtam, *JETP Lett.* **13**, 323 (1971); D. V. Volkov and V. P. Akulov, *Phys. Lett.* **B46**, 109 (1973); J. Wess and B. Zumino, *Nucl. Phys.* **B70**, 39 (1974).

[37] G. Veneziano, *Nuovo Cim.* **A57**, 190 (1968); J. Scherk and J. H. Schwarz, *Nucl. Phys.* **B81**, 118 (1974); *Phys. Lett.* **B57**, 463 (1975); F. Gliozzi, J. Scherk and D. Olive, *Phys. Lett.* **B65**, 282 (1976).

[38] E. Rutherford, *Phil. Mag.* **21**, 669 (1911); *Nature* **92**, 423 (1913).

[39] J.D. Cockcroft and E.T.S. Walton, *Proc. Roy. Soc. London* **A136**, 619 (1932); **A137**, 229 (1932).

[40] V. L. Fitch and J. L. Rosner, in L. M. Brown, A. Pais, and B. Pippard, eds., *Twentieth Century Physics, Vol. II,* Bristol: Institute of Physics and New York: American Institute of Physics, 1995.

[41] E.O. Lawrence and N.E. Edlefsen, *Science,* **72**, 376 (1930); E.O. Lawrence and M.S. Livingston, *Phys. Rev.* **37**, 1707 (1931); **38**, 136 (1931); **40**, 19 (1932).

[42] E.M. McMillan, *Phys. Rev.* **68**, 143 (1945); V. Veksler, *Compt. rend. acad. sci. U.S.S.R.* **43**, 444 (1944); **44**, 393 (1944); *J. Phys. (U.S.S.R.)* **9**, 153 (1945).

[43] P. B. Moon, L. Riddiford, and J. L. Symonds, *Proc. Roy. Soc.* **A230**, 204 (1955); O. Chamberlain *et al.*, *Phys. Rev.* **100**, 947 (1955); J. P. Blewett, *Rep. Prog. Phys.* **XIX**, 37 (1956);

[44] E.D. Courant, M.S. Livingston, H.S. Snyder, *Phys. Rev.* **88**, 1190 (1952).

[45] E. Regenstreif, *CERN* **59-29**, (1959); CERN **60-26**, (1960);

[46] M. S. Livingston and J. P. Blewett, *Particle Accelerators,* New York: McGraw-Hill Book Company, Inc., 1962.

[47] D. W. Kerst *et al.*, *Phys. Rev.* **102**, 590 (1956); G. K. O'Neill, *Phys. Rev.* **102**, 1418 (1956); *Sci. Am.* **215**, 107 (1966).

[48] M. S. Livingston, *FERMILAB-TM* **95**, (1968).

[49] A. Tollestrup, *FERMILAB-CONF-94-378-E*, (1994).

[50] J. Cranshaw, *FERMILAB-CONF-00-320-E*, (2000); P. Petroff, *hep-ex/9910028*, (1999).

[51] E. Baver and M. Leurer, *Phys. Rev.* **D51**, 260 (1995); W. Buchmüller, R. Ruckl, and D. Wyler, *Phys. Lett.* **B191**, 442 (1987).

[52] P.H. Frampton, *Mod. Phys. Lett.* **A7**, 559 (1992).

[53] J. L. Hewett and T. G. Rizzo, *Phys. Rep.* **183**, 193 (1989); E. Accomando *et al.*, *Phys. Rep.* **299**, 1 (1998).

[54] M. Krämer *et al.*, *Phys. Rev. Lett.* **79**, 341 (1997).

[55] J. Blümlein, E. Boos, and A. Kryukov, *Z. Phys.* **C76**, 137 (1997).

[56] J. Blümlein, E. Boos, and A. Kryukov, *hep-ph/9811271* (1998).

[57] H.-U. Bengtsson *et al.*, *Phys. Rev. Lett.* **55**, 2762 (1985).

[58] E. Eichten and K. Lane, *hep-ph/9609297* (1996); *hep-ph/9609298* (1996).

[59] J. Ellis and S. Rudaz, *Phys. Lett.* **B128**, 243 (1983); H. Baer *et al.*, *Phys. Rev.* **D44**, 725 (1991).

[60] W. Beenakker *et al.*, *Nucl. Phys.* **B515**, 3 (1998).

[61] J. Ohnemus, *Phys. Rev.* **D44**, 3477 (1991); S. Frixione, P. Nason, and G. Ridolfi, *Nucl. Phys.* **B383**, 3 (1992).

[62] U. Bauer, T. Han, and J. Ohnemus, *Phys. Rev.* **D51**, 3381 (1995); L. Dixon, Z. Kunst, and A. Signer, *Phys. Rev.* **D60**, 114037 (1999).

[63] A. Stange, W. Marciano, S. Willenbrock, *Phys. Rev.* **D49**, 1354 (1994).

[64] G. Altarelli, B. Mele, and M. Ruiz-Altaba, *Z. Phys.* **C45**, 109 (1989).

[65] C. D. Hoyle, *et al.*, *Phys. Rev. Lett.* **86**, 1418 (2001).

[66] N. Arkani-Hamed, S. Dimopoulos, G. Dvali, *Phys. Lett.* **B429**, 263 (1998); J. Hewett, *Phys. Rev. Lett.* **82**, 82 (1999); T. Han, D. Rainwater, and D. Zeppenfeld, *Phys. Lett.* **B463**, 93 (1999).

[67] J. Thompson, *FERMILAB-TM-1909* (1994).

[68] *http://www-d0.fnal.gov/online/RunI/Analysis/LogLum/run1_online_summary.html*

[69] F. Abe *et al.*, *Nucl. Inst. Meth.* **A271**, 387 (1988).

[70] S. Abachi *et al.*, *Nucl. Inst. Meth.* **A338**, 185 (1994); S. Snyder, *DØ Note* **2500**, (1995).

[71] A. R. Clark *et al.*, *Nucl. Inst. Meth.* **A279**, 243 (1989); J. F. Detoeuf *et al.*, *Nucl. Inst. Meth.* **A279**, 310 (1989).

[72] R. Wigmans, *Nucl. Inst. Meth.* **A259**, 389 (1987); **A265**, 273 (1988).

[73] M. Abolins *et al.*, *Nucl. Inst. Meth.* **A280**, 36 (1989); P. Franzini, *Nucl. Inst. Meth.* **A289**, 438 (1990).

[74] S. Abachi *et al.*, *Nucl. Inst. Meth.* **A324**, 53 (1993).

[75] I. Adam, *Columbia University Ph.D. Thesis*, (1997).

[76] L. Babukhadia, *University of Arizona Ph. D. Thesis* (1999).

[77] J. Bantly *et al.*, *DØ CONF-94-1*(1996).

[78] C. Brown *et al.*, *Nucl. Inst. Meth.* **A279**, 331 (1989).

[79] N. Amos, *DØ Note* **2072**, (1994).

[80] *http://www-d0.fnal.gov/online/RunI/GM/trigger_lists.html*

[81] G. Manning, Ed., *DØ Software Documentation*, unpublished.

[82] *http://www-d0.fnal.gov/physics_analysis/d0fix/d0fix.html*

[83] B. Abbott *et al.*, *DØ Note* **3287**, (1997).

[84] M. Abolins *et al.*, *Nucl. Inst. Meth.* **A289**, 543 (1990).

[85] L. Babukhadia *et al.*, *DØ Note* **3408**, (1998).

[86] B. Abbott *et al.*, *DØ Note* **2885**, (1996).

[87] G. Gomez, *University of Maryland Ph. D. Thesis* (1999).

[88] K. Frame, *et al.*, *DØ Note* **3165**, (1997).

[89] E. Popkov, *DØ Note* **3622**, (2000).

[90] D. Hedin, *DØ Note* **2712**, (1995).

[91] T. Sjostrand, *Comp. Phys. Comm.* **82**, 74 (1994); T. Sjostrand *et al.*, *hep-ph/0010017*, (2000); T. Sjostrand, *hep-ph/0012188*, (2000).

[92] F. A. Berends *et al.*, *Nucl. Phys.* **B357**, 32 (1991).

[93] D. Chakraborty, *DØ Note* **2337**, (1994).

[94] F. Paige and S. Protopopescu, *BNL Report* **BNL38034**, (1986); H. Baer *et al.*, *hep-ph/0001086*, (2000).

[95] S. Jadach, J. H. Kuhn, and Z. Was, *Comp. Phys. Comm.* **64**, 275 (1990); M. Jezabek *et al.*, *Comp. Phys. Comm.* **70**, 69 (1992); S. Jadach *et al.*, *Comp. Phys. Comm.* **76**, 361 (1993); P. Golonka, E. Richter-Was, and Z. Was, *hep-ph/0009302*, (2000); Z. Was, *Nucl. Phys. Proc. Suppl.* **98**, 96 (2001).

[96] B. Klima and C. Stewart, *DØ Note* **905**, (1989); D. Norman, *DØ Note* **1065**, (1990).

[97] CERN *Program Library Long Writeup* **W5013**, (1993); J. Womersley, W. Merritt, and S. Peryshkin, *DØ Note* **1425**, (1992).

[98] W. J. Womersley, R. Raja, and A. M. Jonckheere, *DØ Note* **650**, (1987); W. G. D. Dharmaratna, R. Raja, and C. Stewart, *DØ Note* **1730**, (1993).

[99] P. Tamburello, *University of Maryland Ph.D. Thesis* (1998).

[100] A. S. Belyaev *et al.*, *DØ Note* **3772**, (2000).

[101] E. Boos *et al.*, *DØ Note* **3147**, (1997).

[102] C. Peterson, T. Rognvaldsson, and L. Lonnblad, *Comput. Phys. Commun.* **81**, 185 (1994).

[103] D. Acosta and S. Blessing, *Ann. Rev. Nucl. Part. Sci.* **49**, 389 (1999).

[104] T. Affolder *et al.*, *Phys. Rev. Lett.* **85**, 2056 (2000).

[105] B. Abbott *et al.*, *Phys. Rev. Lett.* **79**, 4321 (1997).

[106] B. Abbott *et al.*, *Phys. Rev. Lett.* **80**, 2051 (1998).

[107] B. Abbott *et al.*, *Phys. Rev. Lett.* **84**, 2088 (2000).

[108] J. Kalinowski *et al.*, *Z. Phys.* **C74**, 595 (1997).

[109] ZEUS Collaboration, J. Breitweg *et al.*, *Eur. Phys. J.* **C16**, 253 (2000).

[110] ZEUS Collaboration, C. Adloff *et al.*, *Phys. Lett.* **B479**, 358 (2000).

[111] L3 Collaboration, M. Acciarri *et al.*, *Phys. Lett.* **B489**, 81 (2000).

[112] ALEPH Collaboration, R. Barate *et al.*, *Eur. Phys. J.* **C12**, 183 (2000).

[113] B. Abbott *et al.*, *Phys. Rev.* **D60**, 072002 (1999).

[114] S. Abachi *et al.*, *Nucl. Inst. Meth.* **A408**, 103 (1998).

Appendix A

Run 2

On March 1, 2001, the Fermilab Tevatron began producing initial state 2 TeV $\sqrt{s}$ $p\bar{p}$ collisions for 'Run 2.' In the next few years the Tevatron will produce a total luminosity of 2×10^3 pb^{-1} (2 fb^{-1}), more than a factor of 20 greater than the luminosity used in this analysis. With the increase in data will come an increase in the statistical significance of the production of new physical processes. If the optimization stays the same as in this analysis, DØ will be able to extend the mass limit for scalar leptoquarks to ~140 GeV/c^2 and the cross section limit for $W(\rightarrow 2jets)Z(\rightarrow \not\!\!E_T)$ production to ~50 pb. The final Run 2 limits will be even better than this, since the optimization will focus on the higher masses observable in Run 2, more efficient triggers will be used, and improvements to the detector [114] will reduce the vertex measurement errors. The collisions the

Fermilab Tevatron produces over the next few years will provide an unprecedented opportunity to search for new physical particles and processes. The knowledge gained through this search will fill in more pieces to the puzzle that we call the universe.